# Intralaminar Fracture Toughness Characterization of a Torn High Strength Cloth with Dyneema® Fibers

Ing. B.J.E. van Rodijnen

Master of Science Thesis

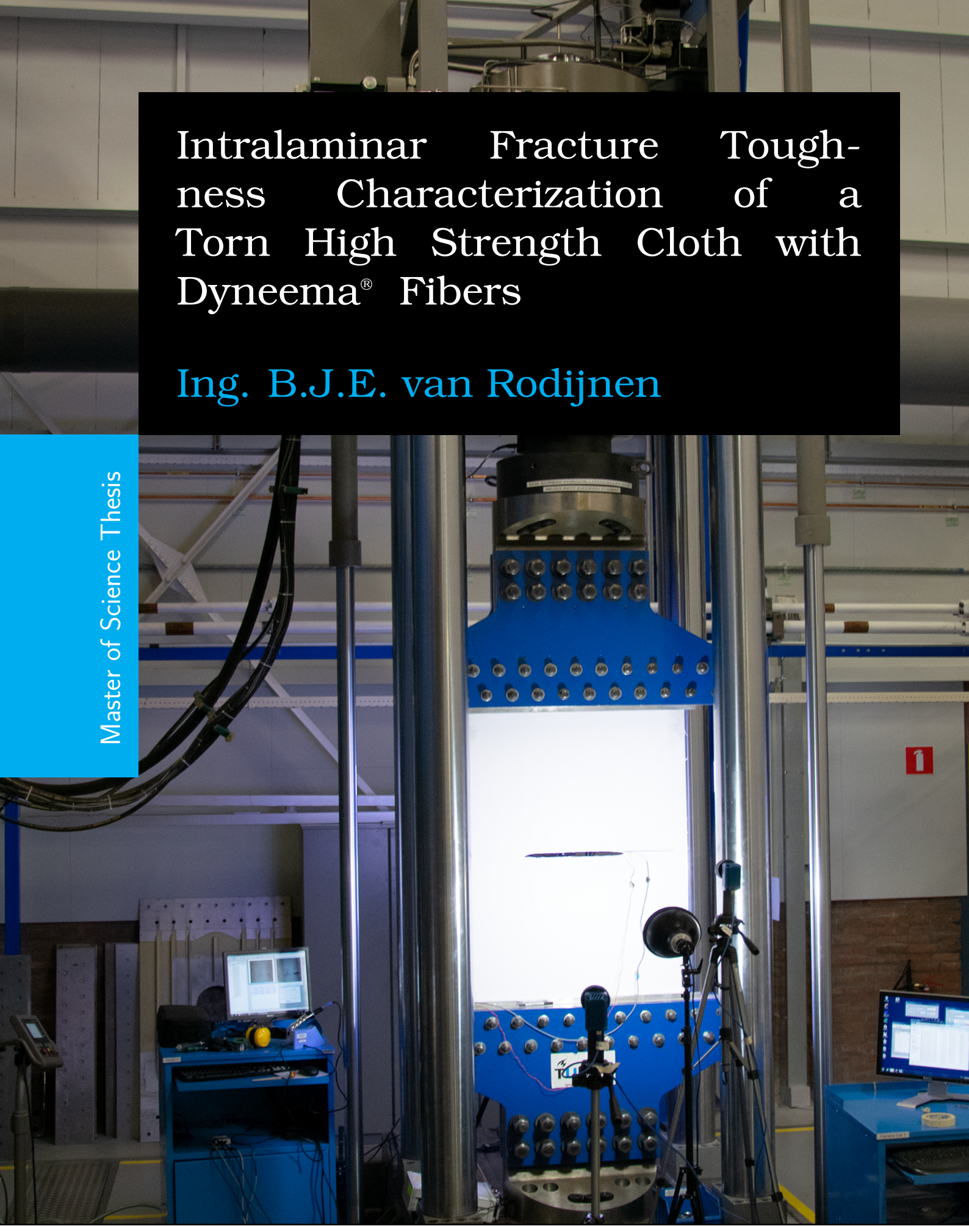

TU Delft Delft University of Technology

Aerospace Structures and Materials

# Intralaminar Fracture Toughness Characterization of a Torn High Strength Cloth with Dyneema® Fibers

Master of Science Thesis

Ing. B.J.E. van Rodijnen

August 30, 2018

Faculty of Aerospace Engineering · Delft University of Technology

The work in this thesis was supported by DSM Dyneema® . Their cooperation is hereby gratefully acknowledged.


Delft University of Technology
Department of Structural Integrity and Composites

The undersigned hereby certify that they have read and recommend to the Faculty of Aerospace Engineering for acceptance a thesis entitled

# Intralaminar Fracture Toughness Characterization of a Torn High Strength Cloth with Dyneema® Fibers

by

Ing. B.J.E. van Rodijnen

in partial fulfillment of the requirements for the degree of

Master of Science in Aerospace Engineering

Dated: August 30, 2018

Chair Holder:

Dr.ir. R.C. Alderliesten

Supervisors:

Prof.dr.ir. R. Marissen

Dr.ir. O.K. Bergsma

Committee member:

Dr. B. Chen

# Abstract

Due to the massive amount af damage inflicted by tsunamis and flood events, DSM Dyneema® and Mehler proposed a new solution for coastline protection, a self-deploying flexible tsunami barrier, made of a high strength cloth with Dyneema® fibers. One of the design considerations is the response of the material with a considerable crack due to debris penetration, loaded by the water pressure. This research characterizes the fracture toughness of the cloth using fracture mechanics tests on center cracked tensile specimens (CC(T)s). Two methods have been investigated which could be used to determine the damage progression of the cloth when a notch is present.

The material consists of a singly ply, plain weave fabric of Dyneema® CF10 fibers, impregnated with Queo 8210 plastomer resin. It is flexible, anisotropic and and the stress strain behavior is non-linear in the weft direction. The non-linearity is a result of the weaving process in combination with the behavior of the resin, leading to highly curved fibers in the weft direction.

Fracture toughness tests are performed on CC(T)s under plane stress conditions with widths of 120, 288 and 900 mm and different initial crack sizes, such that size effects could be investigated. Failure modes encountered during testing are fiber-shifting, fiber pull out, matrix release and eventually fiber breakage. Macroscopically the crack tip blunted into an elliptical form due to crack opening displacement which is as large as the elongation of the material. Although all tests show a reduction in the expected failure load due to the presence of the crack. Failure is not preceded by stable crack extension, but sudden and "explosive" and occurs when the net cross section reaches the ultimate stress level. Therefore the material failure is strength and not fracture mechanics dominant.

Linear elastic fracture mechanics proved not applicable to determine fracture toughness constants. Due to the different behavior and fiber-shifting around the crack tip, the anisotropic stress-field equations proved to be inaccurate in describing the stress field at the crack tip. which does not follow a $1/\sqrt{\pi r}$ relation. Therefore, no critical stress intensity factor (CSIF) $\mathcal{K}_{I_c}$ nor its equivalence, a strain energy release rate (SERR) $\mathcal{G}_{I_c}$ could be determined as a single constant.

A numerical solution is proposed based on the peridynamics (PD) framework. PD is a reformulation of the classical continuum mechanics equation of motion, into a non-local form based on and spatial integral equations. Peridynamic simulation proved well capable of modeling fracture of orthotropic lamina's without the use of special techniques. However, in this research the non-linear behavior of the material, especially fiber-shifting is not sufficiently included in the model. The resulting failure strains of the notched lamina's where therefore conservative compared to the test results.

For the tsunami barrier, the Dyneema® cloth proved to be a good material to use. Since the failure remains strength-dominant, the wide sheets retains high failure strengths when large notches are present. The outer regions are limited effected by the redistribution of the stress throughout the material and it is expected that when the sides are stitched the toughness is increased by the transverse fibers.

# Acknowledgments

Dear Reader,

With submitting this thesis report I am about to finish my Master Degree in Aerospace Structures and Materials. Unfortunately, that also means my time as a student here in Delft will finally come to and end. All those years studying here could not better be described as a great roller-coaster ride. A lot took place, I've made a lot of new friends and have seen a lot of places. During the master and this thesis project I've learned a lot, both on engineering as personally. I really pushed my boundaries and so its a time to never forget, a time that made me who I am today.

This thesis would not haven been written without the help of many people. First of all, I would like to thank my two supervisors, Prof.dr.ir. Roel Marissen and Dr.ir. Otto Bergsma for providing this assignment in cooperation with DSM and for al the assistance, guidance and patience during the entire process of writing this thesis. I would also like to thank Dr.ir. René Alderliesten and Dr. Boyang Chen for taking time to read this report and for taking place in my graduation committee.

Furthermore, I would like to thank the Lab Technicians from the DASML lab. Gertjan, Johan, Victor, Micha and Frans thanks for all the assistance on setting up the test benches and the microscopic equipment. No testing would have been taking place without your help.

This journey the last years would have been impossible without the support and caring of my parents. Im very grateful that they never stopped believing in me and always helped me to pursue my goal to finish my Master Degree.

I would also like to thank my friends here at the faculty and our student room, Peter, Viktor, Gerardo, Bob, Rutger for all the fun and distraction during the process and for all the discussions at the coffee machine.

Last but not least I would like to a give a special thanks to Evert Kranendonk, who really supported me these last years to finish my thesis and always found time to help me, for which i am sincerely grateful.

I hope you will enjoy reading this report,

Ing. B.J.E. van Rodijnen — Delft University of Technology
August 30, 2018

"Look up at the stars and not down at your feet. Try to make sense of what you see, and wonder about what makes the universe exist. Be curious"

— *Stephen Hawkings*

# Contents

## Table of Contents

# List of Figures

# List of Tables

# Nomenclature

## List of Acronyms

| | |
|---|---|
| ASTM | American Society for Testing and Materials |
| CC(T) | Center cracked tensile specimen |
| CFRP | Carbon fiber reinforced polymers |
| CLT | Classical laminate theorem |
| CSIF | Critical stress intensity factor |
| C(T) | Compact tension specimen |
| DCB | Double cantilever beam |
| DIC | Digital image correlation |
| ENF | End-notch flexure |
| FEM | Finite elements method |
| GFRP | Glass fiber reinforced plastic |
| LEFM | Linear-elastic fracture mechanics |
| PD | Peridynamics |
| SE(B) | Single-edge notched bend specimen |
| SEM | Scanning electron microscopy |
| SERR | Strain energy release rate |
| SIF | Stress intensity factor |
| UD | Uni-directional |
| UHMW-PE | Ultra-high-molecular-weight polyethylene |
| VCCT | Virtual crack closure technique |
| XFEM | EXtended finite element method |
| ZNSD | Zero-normalized squared differences correlation criterion |

# List of Symbols

### Latin Symbols

| Symbol | Description | Unit |
|---|---|---|
| $a$ | Half the crack length | $[m]$ |
| $\mathbf{b}(\mathbf{x}, t)$ | Body force density | $[N]$ |
| $c$ | Peridynamic material parameter | $[-]$ |
| $c_f$ | Peridynamic material constant in fiber direction | $[-]$ |
| $c_m$ | Peridynamic material consant in matrix direction | $[-]$ |
| $CV$ | Sample coefficient of variaton | $[\%]$ |
| $E$ | Young's Modulus | $[GPa]$ |
| $f$ | Membrane stress factor | $[-]$ |
| $\mathrm{F}(\diagup)$ | Geometry correction factor | $[-]$ |
| $F_h$ | Resulting force | $[kN]$ |
| $G$ | Shear Modulus | $[GPa]$ |
| $\mathcal{G}_c$ | Critical energy release rate | $[^J/_m]$ |
| $\mathcal{G}$ | Energy release rate | $[^J/_m]$ |
| $\mathcal{H}_\mathbf{x}$ | Particle domain | $[-]$ |
| $\mathcal{K}$ | Stress intensity factor | $[MPa\sqrt{m}]$ |
| $\mathcal{K}_c$ | Critical stress intensity factor | $[MPa\sqrt{m}]$ |
| $M\,(^a/_W)$ | Von Mises plane stress limit load function | $[MPa]$ |
| $m_{dry}$ | Sample dry weight | $[g]$ |
| $m_{wet}$ | Sample wet weight | $[g]$ |
| $\mathcal{M}_x, \mathcal{M}_y, \mathcal{M}_{xy}$ | Moment resultants about the x,y and xy axis | $[Nm]$ |
| $n$ | Time step | $[s]$ |
| $n$ | Number of specimens | $[-]$ |
| $nX, nY$ | Material points in x- and y-direction | $[-]$ |
| $\mathcal{N}_x, \mathcal{N}_y, \mathcal{N}_{xy}$ | Normal and shear force per unit length | $[N]$ |
| $P$ | Applied Load | $[N]$ |
| $\boldsymbol{\mathcal{Q}}$ | Reduced stiffness matrix | $[MPa]$ |
| $\mathbf{S}$ | Pure shear failure stress | $[MPa]$ |
| $s$ | Perdidynamic stretch function | $[-]$ |
| $s_0^{ft}$ | Limits stretch of fibers in tensile | $[\%]$ |
| $s_0^{mt}$ | Limits stretch of matrix in tensile | $[\%]$ |
| $s_{n-1}$ | Standard deviation | $[-]$ |
| $T$ | Membrane tension | $[kN]$ |
| $t$ | Ply thickness | $[mm]$ |
| $t$ | Time | $[s]$ |
| $\mathbf{u}$ | Displacement vector | $[-]$ |
| $U$ | Equiavlent thoughness | $[jm^{-3}]$ |
| $\ddot{\mathbf{u}}(\mathbf{x}, t)$ | Acceleration vector | $[^m/_{s^2}]$ |

| | | |
|---|---|---|
| $\dot{\mathbf{u}}_i$ | Velocity vector | $[^m/_s]$ |
| $v_c$ | Volume correction factor | $[-]$ |
| $V_{in}$ | Initial boundary velocity | $[^m/_s]$ |
| $W$ | Half the witdh of a CCT specimen | $[m]$ |
| $w_f$ | Fracture energy | $[J]$ |
| $W_k$ | Strain energy density | $[-]$ |
| $w_{kj}$ | Micropotential | $[-]$ |
| $\mathbf{x}$ | Position vector | $[-]$ |
| $\bar{x}$ | Samples mean value | $[-]$ |
| $\mathbf{X}^c$ | Compressive stress limit in warp direction | $[MPa]$ |
| $x_i$ | Measured value | $[-]$ |
| $\mathbf{X}^t$ | Tensile failure stress in warp direction | $[MPa]$ |
| $\mathbf{Y}^c$ | Compressive failure stress in weft direction | $[MPa]$ |
| $\mathbf{Y}^t$ | Tensile stress limit in weft direction | $[MPa]$ |

### Greek Symbols

| Symbol | Description | Unit |
|---|---|---|
| $\alpha$ | Inital base angle | $[rad]$ |
| $\Delta$ | Spacing between material points | $[m]$ |
| $\delta$ | Horizon distance | $[m]$ |
| $\boldsymbol{\epsilon}$ | Strain vector | $[-]$ |
| $\epsilon^t_{x_u}, \epsilon^c_{x_u}$ | Strain limits in warp direction | $[\%]$ |
| $\epsilon^c_{y_u}, \epsilon^c_{y_u}$ | Strain limits in weft direction | $[\%]$ |
| $\boldsymbol{\eta}$ | Relative displacement vector | $[m]$ |
| $\gamma_{xy_u}$ | Shear strain limit | $[\%]$ |
| $\kappa$ | Material bulk modulus | $[GPa]$ |
| $\mu$ | Failure parameter | $[-]$ |
| $\nu$ | Poisson's Ratio | $[-]$ |
| $\Omega$ | Ohm | $[\frac{kgm^2}{s^3A^2}]$ |
| $\Phi$ | Biharmonic stress function | $[MPa]$ |
| $\phi(\mathbf{x}, t)$ | Local damage at material point $\mathbf{x}$ | $[-]$ |
| $\Pi$ | Potential energy | $[J]$ |
| $\rho$ | Material density | $[^g/_{cm^3}]$ |
| $\rho_0$ | Density auxillary liquid | $[^g/_{cm^3}]$ |
| $\rho(\mathbf{x})$ | Density function | $[^{Kg}/_{m^3}]$ |
| $\rho_l$ | Density air | $[^g/_{cm^3}]$ |
| $\boldsymbol{\sigma}$ | Stress vector | $[MPa]$ |
| $\sigma_0$ | Nominal stress | $[MPa]$ |
| $\sigma_y$ | Yield stress | $[MPa]$ |
| $\theta$ | Fiber orentiation angle | [deg] |

| | | |
|---|---|---|
| $\boldsymbol{\xi}$ | Initial bond length | $[m]$ |

### Operators

| Symbol | Description |
|---|---|
| $\nabla$ | Divergence operator |

# Chapter 1

# Introduction

In the last few decades, heavy floodings, created by tropical storms, heavy rainfall or tsunami's, inflicted severe damage to life, property and goods along coastlines and riverbanks around the world. A few examples of tropical storms and the devastation they inflicted are Katrina (2005) along the Golf Coast and Irene (2011) along the US east coast[1]. Due to Katrina, a catagory 5 hurricane with wind shears over 280 km/h, 80% of the area around New Orleans was flooded due to failure of the floodwalls. Inflicting an estimated amount of $125 billion damage and over more than 1800 casualties. Irene, which peaked as a category 3 hurricane with wind speeds up tot 190 km/h at the bahamas, hit mostly the east coast of the United Stated around from North-Carolina up to New Jersey and New York. Although weakened to a Cat 1 hurricane, it inflicted heavy floodings and caused for over $14.5 billion damage with more than 50 deadly casualties, especially in the state of New Jersey.
Examples that are even more deadlier and destructive are tsunami's, such as the 2004 Second Christmas Day Indian Ocean tsunami and the 2011 Tōhoku tsunami in Japan. The 2004 tsunami, inflicted by a massive oceanic earthquake with a moment magnitude of 9.1-9.3 and its epicenter 160km west of Sumatra. The tsunami inflicted damage around the entire Indian Ocean from Indonesia till Africa. With 30 meters, the highest tsunami was measured at the west coast of the Indonesian region Aceh. In total more than 230.000 people lost their lives in 12 countries and the total damage was worth $20 billion.
The second example, the Tōhoku tsunami in Japan, was triggered by an 9.0-9.1 moment magnitude earthquake, with its epicenter 70 km east of the Oshika Peninsula. It was the most severe earthquake ever recorded in Japan. The tsunami waves triggered by the earthquake, reached heights up to 20 meters. As a result, 18000 people died or went missing and the total damage inflicted is estimated to be over $360 billion. It led to such damage at the Fukushima Nuclear Power Plant, that the reactor cooling systems broke down, leading to a nuclear meltdown which infected the pacific ocean with radioactive waste.

From the immense destruction of life and property these examples inflicted, it is clear that coastlines are currently not able to withstand floods of these magnitude and governments have to take new measures to protect coastal areas. Coastline protection using dikes or walls is possible, but in order to stop a 20 meter or higher wave, they will have a large impact on the optical impression of the landscape. Also, when using solid or rotating walls, the high bending moments at the base, may lead to inefficient and heavy structures. Therefore, new concepts for flood protection have been proposed. One proposal, first introduced at the Dutch symposium 'Afsluitbaar Open Rijnmond' by van der Ziel[2] in 2010, consists of a collapsible self-deploying parachute barrier which can automatically be deployed during a flood event. This concept is further developed and patented[3] by Marissen et al.[4] using a high strength cloth consisting of the ultra-strong polymer fiber Dyneema® as load carrier. The barrier works by the principal of a self-deploying membrane. A schematic overview of the principle is given in Figure 1-1. The membrane consists of four main parts, the membrane, the floating member, mourning cables and the foundation. The whole structure will be concealed in a gutter on-shore, as shown at the left side of Figure 1-1. The membrane and mourning cables are constraint inside the foundation.

When a flood event starts, the buoyancy forces acting on the floater, will push the floater upwards, pulling the membrane out of the gutter. The mourning cables are fixed to the floating member at

the front, holding the floater in place, preventing any displacement in flow direction. As can bee seen in Figure 1-1b, this situation will form an active wall, preventing the water to move further inland.

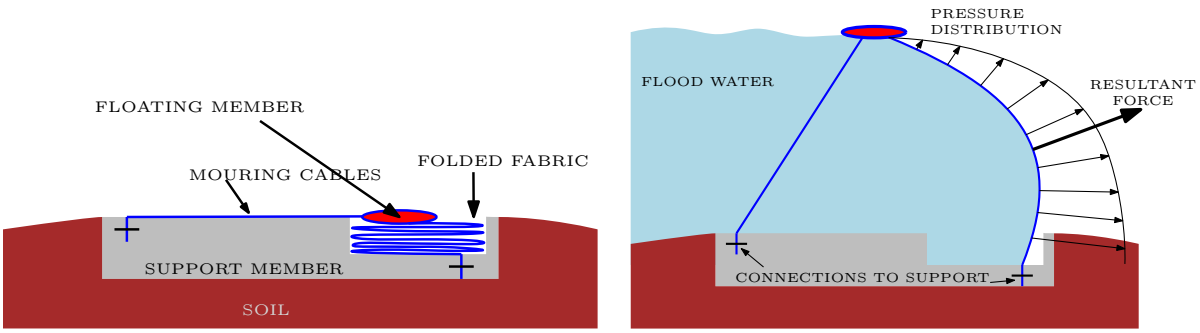


**(a)** The situation when the barrier is stored in a gutter on shore.

**(b)** The situation when the barrier is deployed due to a flood or tsunami. The cloth forms an active wall protecting the coastal area.

**Figure 1-1:** Principle of the flexible membrane flood barrier. At the left when stored, at the right when deployed[4].

One of the main advantage of this structure is the load transfer within the membrane and mooring cables. As shown by Marissen et al.[4], the flood water will form an linear pressure distribution, with a total resulting force $F_h$. This load is transfered to the barrier as a pure tensile force. This leads to a quite efficient structure since no bending loading is present at the foundation. The dynamic behavior of the barrier is investigated further investigated by Hofland et al.[5] showing that a 50 m height and 9 mm thick Dyneema® membrane can withstand a 20m high water level, considering a safety factor of 3. A feasibility study is performed by Horsten[6] by investigating the membrane and site specific design considerations, proofing the feasibility of the concept.

An aspect concerning the design of the flood barrier, is the damage tolerance of the membrane when it's perforated locally by debris. Especially within a tsunami event, where large amounts of debris will be floating in the water, like trees and boats. The impact of large debris on the barrier may lead to perforations or other types of damage. It is unknown what the reaction of the membrane with its Dyneema® backbone will be. For example, will the crack grow steadily, or will the membrane zip open instantly? Such effects might seriously limit the feasibility of the flood barrier concept.

The main goal of this research is to characterize the fracture toughness properties of the fabric and to investigate damage mechanics involved in the process. And to develop a model that can predict the damage growth and critical damage in the flood barrier. The main research question of this thesis is therefore formulated as followed:

> *"What are the intra-laminar fracture toughness characteristics of a notched cloth with Dyneema® Fibers under quasi-static loading and can a tool be developed to determine the critical damage of the flood barrier?"*

Therefore, in this research, the damage tolerance of the membrane is investigated with the main goal to investigate and characterize the fracture mechanical behavior of the Dyneema® cloth, by applying fracture mechanics concepts. And, to investigate if a tool, analytically or numerically can be used or developed to determine the allowable damage in the tsunami barrier.

## 1.1 Thesis outline

The outline of the thesis is as followed. In the first four chapters, the framework of the research is defined. Starting with Chapter 2, containing literature review in which the theory and methods used in this research are reviewed. With the outcome of the literature survey, additional research questions and a hypothesis are formulated as stated in Chapter 3. With theoretical background and additional research questions, the experimental set-up of the research can be developed. The research contains four main experimental parts, determining material properties, fracture mechanics tests, an analytical analysis based on linear-elastic fracture mechanics (LEFM) and a numerical simulation using peridynamics (PD). The design of the experiments and the set-up of the test benches is Chapter 4.

The results of the experiments are given in Chapter 5 till Chapter 8. First, the physical properties and engineering constants of the cloth have to be determined. These values are required for the implementation of the LEFM analysis and PD simulation. The results of the tests are given in Chapter 5. Chapter 6 contains the results of all fracture tests, including the force-displacement graphs, digital image correlation (DIC) analysis and toughness calculations. With the results from the fracture toughness tests, in Chapter 7 an analytical approach based on LEFM is used to determine if is applicable to apply on the tsunami barrier. The last experimental chapter is Chapter 8 in which the results of the numerical fracture simulations of the cloth are elaborated.

In the final two chapters of the report, fracture toughness of the cloth in relation with the tsunami barrier discussed in Chapter 9. Followed by the conclusion of this research and recommendations in Chapter 10.

# Chapter 2

# Literature Review

This research focuses on the application of fracture mechanics towards the damage prediction of the high strength cloth with Dyneema® fibers. This chapter contains a literature review, in which the theory of fracture mechanics methods is reviewed. In the first section of this chapter, Section 2.1, an introduction to the physical appearance and properties of Dyneema® in general is given. In section Section 2.2, the design case of the flood barrier as proposed by Marissen et al.[3] is reviewed, including design parameters and loading factors. The load case is required to determine the allowable crack length.

Since the material is anisotropic, the classical laminate theorem (CLT) is required to describe the stress-strain relations and failure properties. The review of the CLT is given in Section 2.3 The fracture mechanics model reviewed is the linear-elastic fracture mechanics (LEFM), which contains the basics of stress intensity factor (SIF) and strain energy release rate (SERR) and stresses around notches. The method is adjusted to be applied to orthotropic materials, which is reviewed in Section 2.4. The last section, Section 2.5, reviews the fundamentals of the peridynamics (PD) theory, which is proposed as numerical method to model the damage propagation of the Dyneema® fabric.

## 2.1 Dyneema®

Dyneema® is the trademark name for fibers consisting of ultra-high-molecular-weight polyethylene (UHMW-PE) fibers ($(C_2H_4)_n$), invented by DSM and is made of polyethylene molecules with high molecular weight. Dyneema® is created using a gel spinning precess starting from a high temperature solution of UHMW-PE. By cooling down and using a drawing process to untangle the polymer chains, roughly 90% of crystallization can be reached[7]. A UHMW-PE molecule typically contains 100,000 up to 250,000 monomer units[7].

The high tensile strength is reached by the extreme alignment of fibers in the longitudinal direction, so that external loads are transferred through the covalent bonding between the carbon atoms within the chains. The interaction between molecular chains is depended on van der Waals bonds and is therefore low, requiring long chains for shear load transfer between the chains. For comparison, Table 2-1 shows the tensile strength of Dyneema® fibers compared to some specific grades of carbon-, glass- and aramide-fibers according to Edupack[8].

**Table 2-1:** The Ultimate tensile strength, density and specific strength of Dyneema® compared to other types of fibers according to CES-EduPack[8]

| Fiber | Tensile strength (GPa) | Specific density ($^{g}/_{cm^3}$) | Specific strength ($\frac{kN \cdot cm}{g}$) |
|---|---|---|---|
| Dyneema® SK75 | 3.3 - 3.9 | 0.97 - 0.98 | 340 - 400 |
| Carbon T800S | 5.8 | 1.8 | 322 |
| S-Glass | 4.7 - 4.8 | 2.49 - 2.5 | 188 - 192 |
| Kevlar 149 | 3.2 - 3.6 | 1.46 - 1.48 | 219 - 243 |

The ultimate tensile strength of the Dyneema® fibers are comparable with the kevlar 149 grade aramide fibers, but lower than the strengths of carbon T800s and S-glass under pure tensile mode. But, if the specific density is taken into account, it can be noticed that the specific density of the Dyneema® fibers has a value of 0.98 $^{g}/_{cm^3}$. This is very low compared to the carbon T800S and S-Glass fibers, it is even lighter then water. If the specific strength is taken into account, which is defined by dividing the tensile strength over the specific density, the specific strength is the highest for Dyneema® . This indicating that a structure with equal load carrying capability, is the lightest structure when made out of Dyneema® fibers.

Although Dyneema® is very strong in under axial tensile loading, the strength under shear or compression is limited. The polymer backbone of Dyneema® , tends to respond with plastic deformation when loaded under axial compression. Since no hydrogen-bonds are present between the chains and the VanderWaals-bonds or crystalline interactions are much weaker, UHMW-PE fibers tend to fail due to molecular buckling. This leads, according to Marissen et al.[4], to a compressive strength which is is typically just about 1% of the tensile strength.

Since its development, Dyneema® is well established in applications where high tensile stresses occur or high fracture toughness is required. Since UHMW-PE experiences low properties in compression and transverse loading, applications are different than for glass or carbon fiber. An overview of the applications for Dyneema® is given by Marissen[9] and some examples are body and vehicle armor, ropes, sails and cut resistance clothing.

More information about the fabrication process, structure and dynamics of Dyneema® can be found in Marissen et al.[4], Sobieraj et al.[10] and Demco et al.[7].

Recently, DSM-Dyneema® and Mehler developed a very high strength cloth, created by impregnating a plain-weave fabric consisting of Dyneema® fibers with a polyolefin plastomer called Queo 8210. Queo 8210 is an ethylene based octene-1 plastomer, produced by Borealis. According to the data sheet, it has a tensile strength of 24 MPa at a strain of 1000%[11]. Unlike resins like epoxies, which form a solid composite when cured, the impregnated fabric remains flexible. This flexibility allows the flood barrier to be stored folded in a trench, reducing the space required.

## 2.2 Loadcase of the tsunami barrier

The principle of the tsunami barrier is developed by Marissen et al.[4] and patented under Marissen et al.[3]. The loadcase analysis is based on a 20 meter high tsunami.

Marissen et al.[4] modeled the curvature, contour length and the membrane tension $T$ as function of the initial base angle $\alpha$ and a membrane stress factor $f$ with $f < 1$. Load is introduced due to the water level, which decreases linearly towards the water surface. A conceptual membrane shape is given in Figure 2-1. The properties of each ply, as used in the design is a maximum tensile force of 240 $^{kN}/_{m}$ and a ply thickness of 0.75 mm.

The main advantage of using such a flexible structure is that the membrane is loaded under uni-axial tensile stress only. Therefore, no complex and expensive foundation is required to carry the high bending moments that occur at the foundation of walls made out of concrete or steel. Depending on $\alpha$ and $f$, the membrane tension varies between the 994 and 2124 $^{kN}/_{m}$. The optimum contour, according to Marissen et al.[4] and based on a load and cost analysis, has an initial angle of $\alpha = 0.2$ rad ($\approx$ 11,5 deg) and a stress factor of $f = 0.745$, leading to a tensile force of 1013 $^{kN}/_{m}$. Based on an tensile strength of 240 $^{kN}/_{m}$ and a ply thickness of 0.75 mm, 4 plies are required to carry this load, leading to a cloth thickness of just 3 mm. When a safety factor of 3 is applied, the thickness becomes 9 mm. The contour length of the membrane is in this case 37.35 meters.

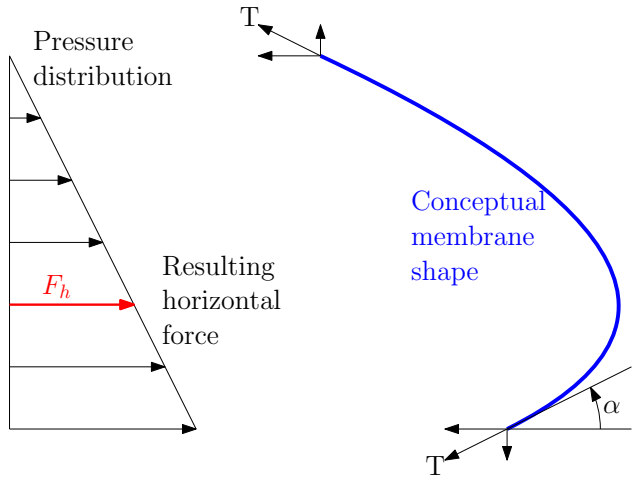


**Figure 2-1:** Conceptual design curve of the membrane

While the barrier runs for several kilometers along coastlines, the fabric can only be produced with a maximum width of 3.2 meters, such that a connection technique is required between the sheets. Although no details on the stitching technique for these connections are available, it will be assumed in this research that the connections are strong enough to act as crack-growth barriers.

## 2.3 Classical laminate theory

In this section the classical lamination theory is reviewed, which describes Hooke's laws to determine the stress and strain state under loading for composite materials. Also some failure criteria are reviewed.

### 2.3.1 Hooke's Law for anisotropic materials under plane stress condition

The basic equations for the state of stress of a continuous anisotropic body can be found in Chapter 1 of Lekhnitskii et al.[12]. A general anisotropic material consists of 81 independent elastic constants. Following the method of Daniel[13], the general equation of Hooke's law for anisotropic materials can be written as:

$$\boldsymbol{\sigma} = \boldsymbol{\mathcal{Q}}\boldsymbol{\epsilon} \tag{2-1}$$

In which $\boldsymbol{\mathcal{Q}}$ is the reduced stiffness matrix, $\boldsymbol{\sigma}$ the stress and $\boldsymbol{\epsilon}$ strain vector.

The full set of equations is reduced by the assumptions that $Q_{ij} = Q_{ji}$ and that specially orthotropic bodies contains two plains of symmetry. The stress-strain relation for an specially anisotropic body can be reduced to:

$$\begin{Bmatrix} \sigma_{11} \\ \sigma_{22} \\ \sigma_{33} \\ \tau_{23} \\ \tau_{13} \\ \tau_{12} \end{Bmatrix} = \begin{bmatrix} \mathcal{Q}_{11} & \mathcal{Q}_{12} & \mathcal{Q}_{13} & 0 & 0 & 0 \\ \mathcal{Q}_{21} & \mathcal{Q}_{22} & \mathcal{Q}_{23} & 0 & 0 & 0 \\ \mathcal{Q}_{31} & \mathcal{Q}_{32} & \mathcal{Q}_{33} & 0 & 0 & 0 \\ 0 & 0 & 0 & \mathcal{Q}_{44} & 0 & 0 \\ 0 & 0 & 0 & 0 & \mathcal{Q}_{55} & 0 \\ 0 & 0 & 0 & 0 & 0 & \mathcal{Q}_{66} \end{bmatrix} \begin{Bmatrix} \epsilon_{11} \\ \epsilon_{22} \\ \epsilon_{33} \\ \gamma_{23} \\ \gamma_{13} \\ \gamma_{12} \end{Bmatrix} \tag{2-2}$$

Since the cloth thickness is very small compared to the width and height, all stresses in the third direction can be omitted. The plate is then said to be in a condition of plane-stress.

$$\sigma_3 = \tau_{23} = \tau_{13} = 0 \tag{2-3}$$

And the stress-strain relation is reduced to the plane-stress equation:

$$\begin{Bmatrix} \sigma_{11} \\ \sigma_{22} \\ \tau_{12} \end{Bmatrix} = \begin{bmatrix} \mathcal{Q}_{11} & \mathcal{Q}_{12} & 0 \\ \mathcal{Q}_{21} & \mathcal{Q}_{22} & 0 \\ 0 & 0 & \mathcal{Q}_{66} \end{bmatrix} \begin{Bmatrix} \epsilon_{11} \\ \epsilon_{22} \\ \gamma_{12} \end{Bmatrix} \tag{2-4}$$

The entries are given as function of the material constants as:

$$\begin{aligned} \mathcal{Q}_{11} &= \frac{E_{11}}{1-\nu_{12}\nu_{21}} \quad (a), \qquad \mathcal{Q}_{12} = \frac{\nu_{21}E_{11}}{1-\nu_{12}\nu_{21}} \quad (c), \qquad \mathcal{Q}_{66} = G_{12} \quad (e), \\ \mathcal{Q}_{21} &= \frac{\nu_{12}E_{22}}{1-\nu_{12}\nu_{21}} \quad (b), \qquad \mathcal{Q}_{22} = \frac{E_{22}}{1-\nu_{12}\nu_{21}} \quad (d), \end{aligned} \tag{2-5}$$

In which $E$ are the Young's modulus in given direction, $\nu$ and $G$. Vica versa, the strains can be written as a function of the stresses by defining the compliance matrix $S$ as the inverse of the stiffness matrix $\boldsymbol{\mathcal{Q}} : \boldsymbol{\epsilon} = [\boldsymbol{\mathcal{Q}}]^{-1}\boldsymbol{\sigma} = \mathbf{S}\boldsymbol{\sigma}$. For the situation of plane-stress, the relation becomes:

$$\begin{Bmatrix} \epsilon_{11} \\ \epsilon_{22} \\ \gamma_{12} \end{Bmatrix} = \begin{bmatrix} S_{11} & S_{12} & 0 \\ S_{21} & S_{22} & 0 \\ 0 & 0 & S_{66} \end{bmatrix} \begin{Bmatrix} \sigma_{11} \\ \sigma_{22} \\ \tau_{12} \end{Bmatrix} \tag{2-6}$$

The entries of the compliance matrix as defined by Daniel[13] are:

$$\begin{aligned} S_{11} &= \frac{1}{E_{11}} \quad (a), \qquad S_{12} = -\frac{\nu_{21}}{E_{22}} \quad (c), \qquad S_{66} = \frac{1}{G_{12}} \quad (e), \\ S_{21} &= -\frac{\nu_{12}}{E_{11}} \quad (b), \qquad S_{22} = \frac{1}{E_{22}} \quad (d), \end{aligned} \tag{2-7}$$

The in-plane stress-strain relations can be determined with 4 independed material properties, $E_{11}, E_{22}, G_{12}$ and $\nu_{12}$. $\nu_{21}$ is a depended property, since its related to $E_{11}, E_{22}$ and $\nu_{12}$ by the relation:

$$\nu_{21} = \nu_{12}\frac{E_{22}}{E_{11}} \tag{2-8}$$

#### Ply rotation

The stiffness properties of a laminate with respect to the reference or loading x-y coordinate system are depended on the alignment of plies in the principle axis system 1-2 described by the rotation or play angle $\theta$ between the principle axis 1-2 and the x-y coordinates system. The equations to rewrite the stiffness properties from the x-y to the 1-2 coordinate system by rotation $\theta$ are given in Appendix A Eq. (A-8a) till Eq. (A-8f). Evenso, the stress and strain can be translated from coordinate system x-y to the 1-2 coordinate system, as shown in Figure A-1 by a tensor rotation with angle $\theta$. The equations are given in Eq. (A-9) and Eq. (A-10).

### 2.3.2 Elastic behavior of a lamina

The stresses acting on a ply in a laminate, can be described as a resultant forces and moments, as shown in Figure 2-2. The definition of the force resultants are given in Eq. (2-9) and the moment resultants in Eq. (2-10).

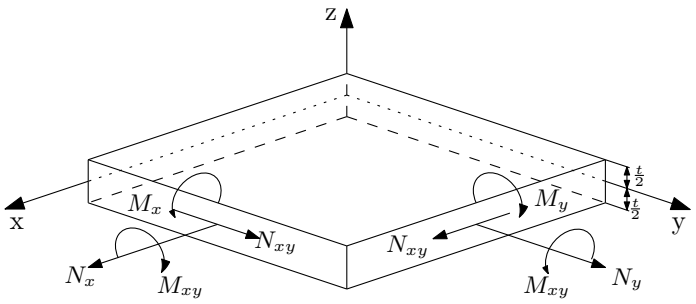


**Figure 2-2:** The force and moment resultant of a ply

$$\begin{bmatrix} \mathcal{N}_x \\ \mathcal{N}_y \\ \mathcal{N}_{xy} \end{bmatrix} = \int_{-t/2}^{t/2} \begin{bmatrix} \sigma_x \\ \sigma_y \\ \tau_{xy} \end{bmatrix} dz \tag{2-9}$$

and:

$$\begin{bmatrix} \mathcal{M}_x \\ \mathcal{M}_y \\ \mathcal{M}_{xy} \end{bmatrix} = \int_{-t/2}^{t/2} \begin{bmatrix} \sigma_x z \\ \sigma_y z \\ \tau_{xy} z \end{bmatrix} dz \tag{2-10}$$

In Eq. (2-9), $t$ is the ply thickness and $\mathcal{N}_x, \mathcal{N}_y, \mathcal{N}_{xy}$ the normal and shear forces per unit length. $\mathcal{M}_x, \mathcal{M}_y, \mathcal{M}_{xy}$ in Eq. (2-10) are the moment resultants.

The force deformation relationship is given within the CLT and given by the equation:

$$\begin{bmatrix} \boldsymbol{\mathcal{N}} \\ \hdashline \boldsymbol{\mathcal{M}} \end{bmatrix} = \left[\begin{array}{c:c} \boldsymbol{\mathcal{A}} & \boldsymbol{\mathcal{B}} \\ \hdashline \boldsymbol{\mathcal{B}} & \boldsymbol{\mathcal{D}} \end{array}\right] \begin{bmatrix} \boldsymbol{\epsilon} \\ \hdashline \boldsymbol{\kappa} \end{bmatrix} \tag{2-11}$$

In which $\boldsymbol{\mathcal{A}}$ is the in-plane extensional stiffness matrix, $\boldsymbol{\epsilon}$ the strain vector $\boldsymbol{\kappa}$ the curvature vector, $\boldsymbol{\mathcal{N}}$ the normal forces and $\boldsymbol{\mathcal{M}}$ the bending moments. $\boldsymbol{\mathcal{B}}$ is the in-plane/flexural coupling matrix and $\boldsymbol{\mathcal{D}}$ bending stiffness matrix. In this research, where only the in-plane 2-dimensional response of the fabric is taken into account, no out-of plane curvatures $\kappa$ nor bending moments $\boldsymbol{\mathcal{M}}$ are assumed to be present. Therefore the $\boldsymbol{\mathcal{B}}$ and $\boldsymbol{\mathcal{D}}$ matrices and the moments ar omitted from the equation, reducing it to:

$$\begin{bmatrix} \mathcal{N}_x \\ \mathcal{N}_y \\ \mathcal{N}_{xy} \end{bmatrix} = \begin{bmatrix} \mathcal{A}_{11} & \mathcal{A}_{12} & \mathcal{A}_{16} \\ \mathcal{A}_{21} & \mathcal{A}_{22} & \mathcal{A}_{26} \\ \mathcal{A}_{61} & \mathcal{A}_{62} & \mathcal{A}_{66} \end{bmatrix} \begin{bmatrix} \epsilon_x \\ \epsilon_y \\ \gamma_{xy} \end{bmatrix} \tag{2-12}$$

The entries $\mathcal{A}_{ij}$ of the matrix are a function of the stiffness matrix, thickness and distance to the center line of a laminate, defined as $\mathcal{A}_{ij} = \sum_{k=1}^{n} Q_{ij}^{k}(z_k - z_{k-1})$. In which k is the ply number counting from the top surface and n the total number of plies. For a single ply, as used in this research, this equation simply reduced to:

$$\mathcal{A}_{ij} = \mathcal{Q}_{ij} t \tag{2-13}$$

Since for the situation of plane stress holds that $\mathcal{Q}_{16} = \mathcal{Q}_{26} = \mathcal{Q}_{61} = \mathcal{Q}_{62} = 0$, the equivalent entries in the $\boldsymbol{\mathcal{A}}$ matrix, $\mathcal{A}_{16} = \mathcal{A}_{26} = \mathcal{A}_{61} = \mathcal{A}_{62}$, are 0 as well.

By inverting the $\boldsymbol{\mathcal{A}}$ matrix, defining the compliance matrix $\boldsymbol{a}$ as $[\boldsymbol{\mathcal{A}}]^{-1} = \boldsymbol{a}$, the relation of Eq. (2-12) can be rewritten to:

$$\{\boldsymbol{\epsilon}\} = [\boldsymbol{\mathcal{A}}]^{-1} \{\boldsymbol{\mathcal{N}}\} = [\boldsymbol{a}] \{\boldsymbol{\mathcal{N}}\} \tag{2-14}$$

### 2.3.3 Lamina Strength and Failure criteria

To determine the allowable loads on the Dyneema® cloth under essential undisturbed conditions, failure laws are used as based on the maximum allowable stress and strain. Three theories are used, the maximum stress, maximum strain and Tsai-Hill law which can be found in literature like Kassapoglou[14].

When the applied loads on a laminate are high they may exceed the strength of the material leading to failure. As shown by Kassapoglou[14], it is possible to simplify the damage criterion on macro-mechanics level, based in stress or strain limits. These values are determined experimentally.

The maximum stress limits are defined as:

- $\mathbf{X}^t$: The tensile stress limit in warp direction.
- $\mathbf{X}^c$: The compressive failure in warp direction.
- $\mathbf{Y}^t$: The tensile failure in weft direction.
- $\mathbf{Y}^c$: The compressive stress limit in weft direction. And
- $\mathbf{S}$: Pure shear failure stress.

Evenso, the maximum strain limits are defined as:

- $\epsilon^t_{x_u}, \epsilon^c_{x_u}$, the tensile and compressive strain limits in warp direction.
- $\epsilon^c_{y_u}, \epsilon^c_{y_u}$ the tensile and compressive strain limits in weft direction
- $\gamma_{xy_u}$ the shear strain limit.

The alignment of the strength criteria with the principle axis is shown in Figure 2-3. For the definition of the failure criteria in this research, the warp direction equals the 1-direction.

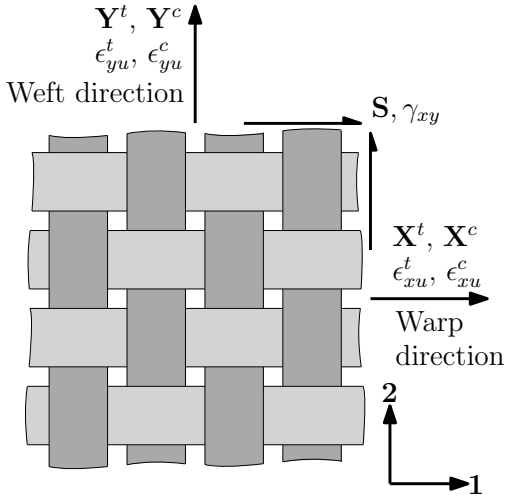


**Figure 2-3:** Failure parameters of a plain weave composite lamina

### Maximum Stress Failure Theory

Within the maximum stress theory, the principle stresses, $\sigma_x$,$\sigma_y$,$\tau_{xy}$ within a ply are compared with their strength values. The failure laws are given in Eq. (2-15) and are depended whether the stresses are in compression or tensile.

$$\begin{aligned} \sigma_x &< X^t \text{ or } X^c \\ \sigma_y &< Y^t \text{ or } Y^c \\ |\tau_{xy}| &< S \end{aligned} \tag{2-15}$$

### Maximum Strain Failure Theory

A second failure theory is the maximum strain theory, in which the principle strains $\epsilon_x$, $\epsilon_y$ and $\gamma_{xy}$ are compared with the allowable strains, $\epsilon^t_{x_u}, \epsilon^c_{x_u}$ the tensile and compressive strain limits in warp

direction, $\epsilon^c_{y_u}, \epsilon^c_{y_u}$ the tensile and compressive strain limits in weft direction and $\gamma_{xy_u}$ shear strain limit of the ply. The equation are given in Eq. (2-16).

$$\begin{aligned} \epsilon_x &< \epsilon^t_{x_u} \text{ or } \epsilon^c_{x_u} \\ \epsilon_y &< \epsilon^t_{y_u} \text{ or } \epsilon^c_{y_u} \\ |\gamma_{xy}| &< \gamma_{xy_u} \end{aligned} \tag{2-16}$$

#### Tsai-Hill Failure Theory

Both in the maximum stress as the maximum strain criteria, each parameter is compared individually with their corresponding allowable. In reality, stress and strain may interact with each other, leading to a failure at which each individual component did not reach its critical value. The Tsai-Hill criterion consists of an equation that does account for this interaction and is defined as[14]:

$$\frac{\sigma_x^2}{X^2} + \frac{\sigma_y^2}{Y^2} - \frac{\sigma_x \sigma_y}{X^2} + \frac{\tau_{xy}^2}{S^2} = 1 \tag{2-17}$$

In Eq. (2-17), failure occurs once the left side of the equation, which is a function of the all three stresses, reaches 1.

## 2.4 Linear Elastic Fracture Mechanics (LEFM)

For load bearing structures two types of strength failure exist. The first one, the yielding-dominant failure, in which significant defects warp and interrupt the crystal lattice space within the material. General plasticity of the gross section occurs in this case. The second one, is the fracture-dominant failure in which fracture occurs before yielding of the gross section. Plasticity is highly localized and occurs at location of stress concentrations, for example around crack tips.

The first accepted solution to a fracture-dominant problem was given by Griffith et al.[15], who has developed the concept that a crack will propagate if the total energy of the system is lowered. A decrease in elastic strain energy, is counteracted by the energy required to create new crack surfaces. Based on Griffith's theorem, Irwin developed the concept of the energy release rate $\mathcal{G}$. And by using the stress field equations from Westergaard[16], Irwin showed that the stresses and displacements at a crack tip could be evaluated using a single constant, the stress intensity factor (SIF), $\mathcal{K}$. This led to the development of the LEFM, with $\mathcal{K}_c$ critical stress intensity factor and $\mathcal{G}_c$ critical energy release rate as material properties governing fracture. These conditions are valid under essentially elastic conditions, in which no, or very small, local plasticity occurs around the crack tip and the plastic zone size should be much smaller than the crack length. Note that these laws are firstly developed to determine the fracture toughness of isotropic materials, especially metals. Later, these methods are adapted to be applicable for composites.

#### Modes of Fracture

When a body containing a crack is loaded, the opposite sides of the crack surface will move with respect to each other. Within fracture mechanics, three independent modes of movement are distinguished based on the type of loading and displacement direction, as sketched in Figure 2-4. Mode I is the in-plane crack opening loading under pure tension. Mode II, in-plane shearing under shear loading. And Mode III, out-of-plane tearing, due to loading under out-of-plane shear. In general, problems can exists based on one or a combination of several loading modes.

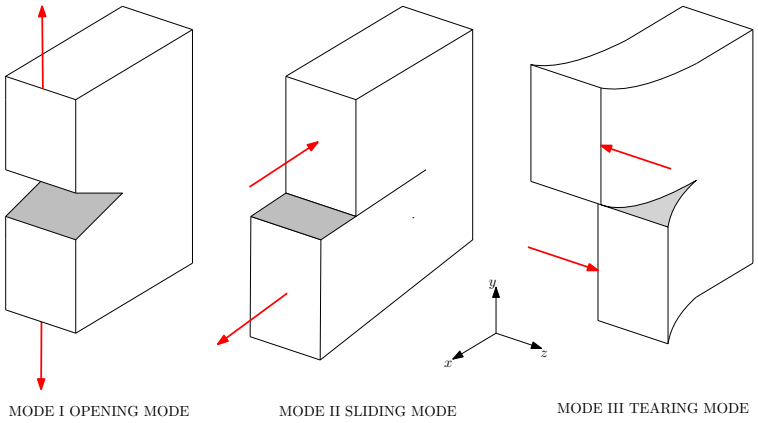


**Figure 2-4:** Fracture Modes

### 2.4.1 The elastic stress field around a crack tip

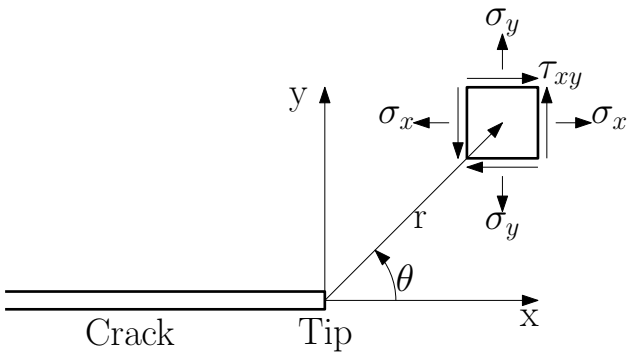


**Figure 2-5:** Stress Components around the crack tip

Figure 2-5 shows the components of stress at the vicinity of cracktip, which is split in 3 stresses. $\sigma_x$, $\sigma_y$ and the shear stress $\tau_{xy}$ as function of the coordinates $(r, \theta)$.

Considering a central and traction free crack with length 2a in an infinite plate, loaded uniformly with a biaxial stress, Westergaard[16] has been able to describe the solution to the stress field around the crack tip as given in Figure 2-5, using a biharmonic stress function $\Phi$ as defined in Eq. (2-18).

$$\Phi = Re\bar{\bar{\Phi}}(z) + yIm\bar{\Phi}(z) \tag{2-18}$$

with $\Phi(z) = \sigma_0 \left(1 - \frac{a^2}{z^2}\right)^{-1/2}$ an $\bar{\bar{\Phi}}$ and $\bar{\Phi}$ the second and first integral respectively. The complete derivation for the stress functions around the crack tips is given in Janssen et al.[17] and Anderson[18]. In the resulting equations for $\sigma_x$, $\sigma_y$ and $\tau_{xy}$ the higher order terms are neglected, therefore these equations hold for small values of $r$ around the crack tip only.

For a plate with an uni-axial loading in the $y$-direction, the stress field can not be solved by these Westergaard equations due to the constraint that at $y = 0$, $\sigma_x = \sigma_y$. Irwin[19] proposed a solution that subtracts the remote stress $\sigma$ from the expression of $\sigma_x$. Applying this principle to the equation for $\phi$ of the biaxial case the boundary conditions are satisfied. This leads to the exact same stress field equations, except for $\sigma_x$. However, the remote stress $\sigma$ at the vicinity of the crack tip is much smaller than $\sigma_x$, therefore this correction can be omitted.

The Westergaard equations are extended to anisotropic materials by Lekhnitskii et al. (1968)[12], resulting in complex functions for the strain and displacement fields, which are given in App. B.1.

### 2.4.2 Stress intensity factors

The parameters $\mathcal{K}_{I,II,III}$, representing the stress intensity factors, are first introduced by Irwin[19] and is defined as measurement for the strength of the singularity at the crack tip. The general formulation of the SIF for mode I, II and III are given in Eq. (2-19).

$$\begin{bmatrix} \mathcal{K}_I \\ \mathcal{K}_{II} \\ \mathcal{K}_{III} \end{bmatrix} = \lim_{r \to 0} \sqrt{2\pi r} \begin{bmatrix} \sigma_y(r,0) \\ \tau_{yx}(r,0) \\ \tau_{yz}(r,0) \end{bmatrix} \tag{2-19}$$

Crack extension will occur when $\mathcal{K}$ reaches a critical value $\mathcal{K}_c$, which is a bulk material property. An overview of stress intensity factors for a wide range of geometries and cracks is given by Tada et al.[20]. The Mode I stress intensity factor can be generalized as

$$\mathcal{K}_I = \sigma\sqrt{\pi a} \cdot F\left({}^{a}/_{W}\right) \tag{2-20}$$

in which $a$ and

$$F({}^{a}/_{W})$$

a geometry correction factor as function of crack size and width. For the center cracked tensile specimen (CC(T)) specimen, used in this research, the correction factors are stated in Section 2.4.5

### 2.4.3 The SERR

The energy release rate $\mathcal{G}$ is defined by Irwin[21] as the available energy per increment of crack extension per unit thickness. This energy is released from an elastic structure when the crack grows and a new crack surface is created. $\mathcal{G}$ is developed from the Griffin energy theory and for a wide plate with crack of length $2a$ in plane stress $\mathcal{G}$ is defined as:

$$\mathcal{G} = -\frac{d\Pi}{dA} = \frac{\pi\sigma^2 a}{E} \tag{2-21}$$

With $\Pi$ representing the potential energy. The full derivation of this equation can be found in Chapter 2.4 of Anderson[18]. Similar to the critical stress intensity factor, at the moment the strain energy reaches a critical value, $\mathcal{G}_c$ defined by Eq. (2-22), crack extension occurs.

$$\mathcal{G}_c = -\frac{dW_S}{dA} = 2w_f \tag{2-22}$$

In which $w_f$ is the surface energy per unit area. Assumped constant for isotropic materials. In terms of the compliance $\mathrm{C}(\Delta/P)$ the equation for $\mathcal{G}$ can be rewritten as:

$$\mathcal{G} = \frac{P^2}{2B}\frac{dC}{da} \tag{2-23}$$

Which according to Anderson holds for both load as displacement control fracture testing.

### 2.4.4 Relation between $\mathcal{K}_c$ and $\mathcal{G}_c$ for an anisotropic material

For an anisotropic material under plane stress, the relationship between the critical stress intensity factor and critical strain energy release rate is defined by Tada et al.[20] as:

$$\mathcal{G}_i = \mathcal{C}\mathcal{K}_i^2 \tag{2-24}$$

Where $i$ refers to the mode of fracture. The value of C depends on the type of material and the fracture mode. For an anisotropic material under Mode I loading, C is defined as:

$$\mathcal{C} = -\frac{S_{11}}{2} Im\left(\frac{\mu_1 + \mu_2}{\mu_1 \mu_2}\right) \tag{2-25}$$

In which $\mu_1$ and $\mu_2$ are the roots of the 4th order polynomial defined as:

$$S_{11}\mu^4 - 2S_{16}\mu^3 + (2S_{12} + S_{66})\mu^2 - 2S_{26} + S_{22} = 0 \tag{2-26}$$

Other values for C for isotropic, orthotropic and anisotropic materials under different modes of fracture are given in Table B-1.

### 2.4.5 The center cracked tensile specimen (CC(T)) test specimen

Due to the thin and flexible nature of the cloth, the only geometry applicable in this research to determine the fracture toughness characteristics is the center cracked tensile specimen specimen. The lay-out of the geometry is given in Figure 2-6. In which $W$ is half the width, $a$ half the crack length and $L$ half the height of the specimen. The width over height is constraint to $2W < 3L$. This constraint is required such that the stress has enough area above and below the crack can level out to a nominal stress distribution $\sigma_0$. So far, the stress distribution around the crack tip, as derived by Westergaard, has been derived for a crack in an infinite body. These solutions may be used when the crack is much smaller than the size of the body, $a << W$. When the crack size becomes in the order of magnitude of the width of the plate, the stress intensity factor will be influenced by the body. When this is the case, a correction factor must be added to the SIF equation given in Eq. (2-19). This factor is defined as the geometry correction function $F(a/W)$, so that $\mathcal{K}_I = \sigma\sqrt{\pi a} \cdot F\left(a/b\right)$. The function is depended on the width of the specimen, $2W$ and the crack length $2a$. Most correction functions are determined empirically. Two of the functions, as provided by Tada et al.[20] or Janssen et al.[17] are given by Eq. (2-27) and Eq. (2-28)

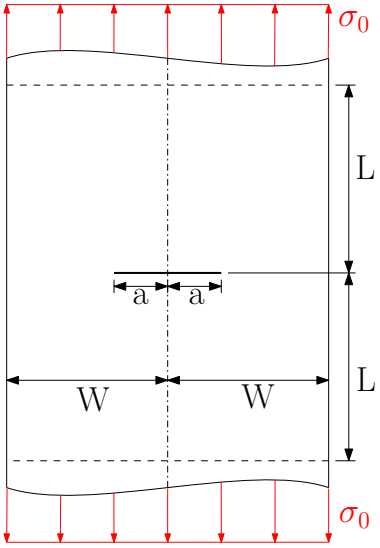


**Figure 2-6:** The center cracked tensile specimen (CC(T)) test specimen

**Irwin's Formula:**
Accuracy: 5% for $a/2W \leq 0.25$

$$F\left(a/W\right) = \sqrt{\frac{2W}{\pi a} \tan\frac{\pi a}{2W}} \tag{2-27}$$

**Fedderson's Formula:**
Accuracy: 0.1% for any $a/W$

$$F\left(a/W\right) = \left[1 - 0.025\left(a/W\right)^2 + 0.06\left(a/W\right)^4\right]\sqrt{\sec\frac{\pi a}{2W}} \tag{2-28}$$

Lei et al.[22] investigated the fracture behavior of a CC(T) specimen analytically, starting with defining the SIF as a function of load as:

$$K = \frac{P\sqrt{\pi a}}{2tW}F\left(a/W\right) \tag{2-29}$$

In which $P$ is the applied load.

The limit load function for a CC(T) specimen is given by Lei et al.[22] as:

$$P_L = \sigma_y 2tW M\left(a/W\right) \tag{2-30}$$

In which $\sigma_y$ is the yield stress of the material and $M\left(a/W\right)$ is the Von Mises plane stress limit load function defined as:

$$M\left(a/W\right) = 1 - \left(a/W\right) \tag{2-31}$$

#### Boundary conditions

Using the CC(T) specimen for fracture toughness testing does alter the boundary conditions when compared to the actual tsunami barrier. At the barrier, the sides of the cloth will by fixed together constraining te lateral movement of the edges when loading in tensile. During testing, the sides will not be constrained and therefore the edges are allowed to move laterally.

### 2.4.6 Application of fracture mechanics on composite materials

In general, the damage formation and evolution within a composite ply for a given loading condition, is lay-up depended. The failure modes due to fracture can be distinguished into three main types, interlaminar, intralaminar and translaminar. Interlaminar failure consist of fiber fracture, matrix fracture and fiber pull-out in a ply. Interlaminar fracture toughness referes to interface damage between the plies, like delamination. Translaminar failure is failure due to out of plane loading like impact damage or bending. In this research, intralaminar fracture mechanics is considered, since the material consist only of one ply. Failure modes included are thus, fiber failure, fiber pull-out, matrix cracking and matrix release.

Sih et al.[23] and Wu[24] where one of the first to apply the principles of SIF on orthotropic plates showing that the stress distribution around the crack tip is depended on the geometry and orientation of the crack. Wu stated that in order to apply the SIF concept in anisotropic bodies, the hypotheses is required that the crack is fixed with respect to the elastic symmetry of the plate. Also the orientation must be known. By performing a series tests on balsa wood and glass fiber reinforced plastic (GFRP) he proved that the SIFs where material constants.

The major differences in applying LEFM towards composites is the direction of crack growth, which is depended on fiber orientation. Crack tip displacement under a single mode load, can result in a mixed mode I & mode II displacement fields. Also, the material crack tip stresses are function of complex parameters $\mu_1, \mu_2, \mu_3$ which are functions of the material property and orientation and are acquired by solving the $4^{\text{th}}$ order polynomial as given in Eq. (B-4)[25]. It can therefore not be said

that the principles of linear-elastic fracture mechanics hold for orthotropic materials in general. Therefore, in each case it must be examined independently if LEFM is applicable.

Most research on intralaminar fracture toughness on composites is done on UD orientated fibers. Parhizgar et al.[25] found that the application of linear elastic fracture intensity was defined as:

$$\mathcal{K}_{Ic} = (0.739\theta^2 + 0.19\theta + 1)\mathcal{K}_{Ic_0} \tag{2-32}$$

Where $\theta$ is the fiber orientation angle and $\mathcal{K}_{Ic_0}$ the critical stress intensity factor for $\theta = 0$.

Marissen et al.[26] applied the principles of LEFM on quasi-isotropic unidirectional GFRP laminates, with sharp center notches. $\mathcal{K}-\mathcal{R}$-curves where constructed by adapting a crack-bridge model, which relieves the stress due to the presence of intact $\pm 45$ deg layers at the crack tip. The similarity of the $\mathcal{R}$ -curves for different initial crack lengths showed the validity of applying LEFM on quasi-isotropic laminates.

The stress equations around a crack in an anisotropic body are first derived by Lekhnitskii et al.[12]. The equations under a Mode I loading are given in Eq. (B-1) till Eq. (B-3). The displacements $u$ in x-direction and $v$ in y-direction of the body around the cracktip are given by Eq. (B-5) and Eq. (B-5).

### 2.4.7 Fracture toughness testing on Dyneema®

Several papers have been published in which fracture toughness properties of Dyneema® has been investigated. Porras et al.[27] and Lässig et al.[28] determined the interlaminar fracture toughness using Dyneema® laminates with uni-directional (UD) plies and Double cantilever beam (DCB) test specimens. The failure mode is delamination between the plies. Altough the failure mode is different than in this research, they show the difficulties in testing Dyneema® due to the difficulty in machining and sufficiently clamping test specimens, such that now slip occurs. Also, the end-notch flexure (ENF) specimens used, tend to snap before crack growth is observed. Lässig et al.[28] solved this issue by testing on relatively thick ENF specimen on which steel plates are bonded on the top and bottom surface.

#### Effect of loading rate

Since crack growth is essentially a dynamic event, the fracture toughness related properties of the material can be depended on the strain or loading rate. May et al.[29] investigated this effect by Interlaminar Mode I fracture toughness testing on Dyneema® HB26. Using very thick DCB test specimens, at loading rates of 1, 10 and 100 $^{mm}/_{s}$ and determined the fracture toughness by the area method defined as:

$$\mathcal{G}_{Ic} = \frac{dW}{dA} = \frac{W_{total} - W_{elastic}}{t \cdot a_{eff}} \tag{2-33}$$

In which $dW$ represents the energy change by crack propagation, $dA$ the increase in crack surface $t$ is the thickness of the specimen, and $a_{eff}$ the effective crack length.

He showed that for loading rates below 10 $^{mm}/_{s}$, no change in fracture toughness is observed. Above this rate, the critical energy release rate increases with increasing loading rate. Testing with low strain rates is therefore conservative for determining the most critical SERR.

## 2.5 Numerical modeling with peridynamics

The composition of a fiber-reinforced, strong stiff fibers embedded in a soft resin, makes the physics of damage initiation and propagation less understood as for metals. Notches and cut-out included in composites structures do not only reduce the overall strength but also serve as a potential location of damage initiation. Under the assumption of homogeneity, a lamina has orthotropic elastic properties, which are suitable for stress-strain analysis. However, when failure is included, the different failure modes such as delamination, fiber failure or matrix cracking, are inherent to the inhomogeneous characteristic of the composite. Each lamina with different fiber orientation must therefore be modeled with distinct fiber and matrix properties so that the inhomogeneous properties of the composite are retained within the simulation. Within the framework of finite elements method (FEM), it is quite challenging to predict failure and residual strengths in a material. Remeshing may be required and cracks can only grow in certain directions. Although the use of special elements, such as cohesive elements or the eXtended finite element method (XFEM)[30] may be able to predict crack growth, the methods require a predefined damage path and rely on external crack-growth criteria, that prescribes the evolution of damage initiation and growth based on local conditions. The challenge in obtaining fracture parameters experimentally and generalizing the data into the required criteria, is especially for composites, a major obstacle for modeling using the conventional methods.

The challenge in failure prediction along a arbitrary path within a body, using the concepts of fracture mechanics in conjunction with FEM, arises from the mathematical foundation of the classical continuum mechanics. The main equation of motion within the classical continuum mechanics theory, using the conservation of linear momentum, is written as:

$$\rho(\mathbf{x})\ddot{\mathbf{u}}(\mathbf{x},t) = \nabla\boldsymbol{\sigma} + \mathbf{b}(\mathbf{x},t) \tag{2-34}$$

In which $\mathbf{x}$ is the position vector of a material point, $\rho(\mathbf{x})$ represents the density of the body as function of $\mathbf{x}$, $\ddot{\mathbf{u}}(\mathbf{x},t)$ the acceleration of point $\mathbf{x}$ as function of time $t$, $\nabla$ the divergence operator, $\boldsymbol{\sigma}$ the stress tensor. $\mathbf{b}(\mathbf{x},t)$ is the body force vector.

The problem with using the classical equation of motion is that the spatial derivatives, contained in the divergence operator $\nabla$ and associated with the stress tensor $\boldsymbol{\sigma}$, are by definition, not defined along the boundaries of discontinuities such as cracks, enforcing the requirement of special techniques. In this research, a numerical method is proposed which removes the limitation of the partial derivatives by redefining the equation of motion. This method, called Peridynamics (PD), is first introduced in by Silling (2000)[31] as a non-local theory, in which an integral equation describes the pairwise interaction between two material points. These materials points do not only interact with their direct neighbors, but with all other material points that lie within a certain region, called the horizon.

Since the introduction of the peridynamic theory, several papers have been published in which the crack propagation of orthotropic materials successfully has been researched, for both quasi-static as dynamic loading. Kilic et al.[32] was able to predict the basic failure modes in several laminate lay-ups with pre-existing central notch, capturing the fiber, matrix and delamination failure modes.

In this section, a review is given of the mathematical framework of the PD theory. The complete theory of PD is given by Silling[31], Silling et al.[33] and Madenci et al.[34].

### 2.5.1 Mathematical foundation

#### Equation of motion

Silling[31] reformulated the equation of motion by replacing the divergence operator with an integral

equation, which by definition, is defined along the boundaries of discontinuities. Let $\mathbf{x}$ be a material point that interacts with all particle points $\mathbf{x}'$ within its spherical neighborhood $\mathcal{H}_{\mathbf{x}}$, as can be seen in Figure 2-7. The radius of $\mathcal{H}_{\mathbf{x}}$, called its horizon, is denoted by $\delta$.

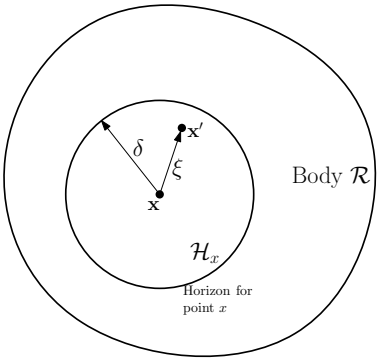


**Figure 2-7:** Interaction of material point $\mathbf{x}$ with material point $\mathbf{x}'$ within body R.

The main peridynamic equation of motion as derived by Silling[31] replaces the the divergence operator $\nabla$ in Eq. (2-34) by the integral equation, which calculates the resulting internal resultant force on material point $\mathbf{x}$ due to all interactions with all other material points $\mathbf{x}'$ within $\mathcal{H}_{\mathbf{x}}$. The peridynamic equation of motion is shown in Eq. (2-35)

$$\rho(\mathbf{x})\ddot{\mathbf{u}}(\mathbf{x},t) = \int_{\mathcal{H}_{\mathbf{x}}} \mathbf{f}(\mathbf{u}(\mathbf{x}',t) - \mathbf{u}(\mathbf{x},t), \mathbf{x}' - \mathbf{x}) d\mathcal{V}_{\mathbf{x}} + \mathbf{b}(\mathbf{x},t) \tag{2-35}$$

In which $\mathcal{H}_{\mathbf{x}}$ is de domain around particle at $\mathbf{x}$ defined by the horizon distance denoted by $\delta$. $\mathbf{f}(\mathbf{u}(\mathbf{x}',t) - \mathbf{u}(\mathbf{x},t), \mathbf{x}' - \mathbf{x})$ represents the pairwise response function between material points at $\mathbf{x}$ and $\mathbf{x}'$, due to the displacements given by the vectors $\mathbf{u}$ and $\mathbf{u}'$. Which is integrated over the volume of the body within the horizon $\mathcal{H}_{\mathbf{x}}$.

The initial bond length between the material particles at $\mathbf{x}$ and $\mathbf{x}'$ is defined as $\boldsymbol{\xi}$. The relative displacement of the material particles at $\mathbf{x}$ and $\mathbf{x}'$ is defined as $\boldsymbol{\eta}$. Hence, $\boldsymbol{\xi} = \mathbf{x}' - \mathbf{x}$ and $\boldsymbol{\eta} = \mathbf{u}(\mathbf{x}',t) - \mathbf{u}(\mathbf{x},t)$. In deformed state, the relative position vector is represented by $\boldsymbol{\xi} + \boldsymbol{\eta}$.

When the coordinates in deformed state are defined as $\mathbf{y} = \mathbf{u} + \mathbf{x}$ and $\mathbf{y}' = \mathbf{u}' + \mathbf{x}'$, the stretch $s$ between two material points can be defined as:

$$s = \frac{|\boldsymbol{\xi} + \boldsymbol{\eta}| - |\boldsymbol{\xi}|}{|\boldsymbol{\xi}|} = \frac{|\mathbf{y}' - \mathbf{y}| - |\mathbf{x}' - \mathbf{x}|}{|\mathbf{x}' - \mathbf{x}|} \tag{2-36}$$

Substituting Eq. (2-36) into the bond-force function $\mathbf{f}$ and by defining $c$ as peridynamic material parameter, $\mathbf{f}$ can be written as:

$$\mathbf{f} = cs\frac{\mathbf{y}' - \mathbf{y}}{|\mathbf{y}' - \mathbf{y}|} \tag{2-37}$$

For an isotropic linear material, the value of $c$ is derived by Silling et al.[33] in explicit form as $c = {}^{18\kappa}/_{\pi\delta^4}$, where $\kappa$ is the material bulk modulus. The derivation of peridynamic material properties for orthotropic materials, such as a UD-lamina and laminates, is given by Oterkus et al.[35]. In Section 2.5.2, the most important parameters are reviewed.

### 2.5.2 Peridynamic Material properties for an Orthotropic lamina

When modeling a fiber-reinforced composite lamina, the dependency of the fiber-orientation must be included, leading to different PD parameters. Figure 2-8a shows the interaction of particle $i$

with all particles within its neighborhood $\mathcal{H}_\mathbf{x}$. The fiber orientation with respect to the x-axis is given by angle $\theta$ and the angle between the bond-vector and the x-axis is defined as $\phi$. Point $q$ is an arbitrary material point that interacts with point $i$ along the fiber direction ($\phi = \theta$). Point $p$ is an arbitrary material point that interacts with material point $i$ at any other direction ($\phi \neq \theta$).

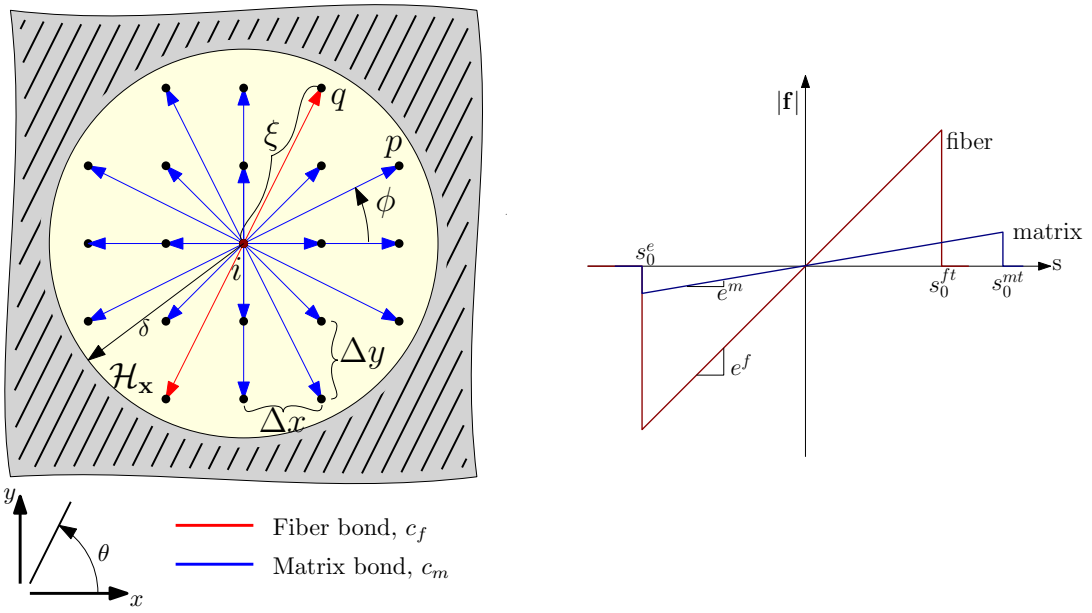


**(a)** Definition of the material bonds as function of the bond angle $\phi$

**(b)** The bond force density $|\mathbf{f}|$ as function of the bond strain $s$ in fiber and matrix direction

**Figure 2-8:** Definition of peridynamic material constants

The composite material can then be expressed by two peridynamic constants, the peridynamic material constant in fiber direction $c_f$, and the peridynamic material constant in any other direction $c_m$. The two stretch functions are given in Figure 2-8b. The limit stretch of $c_f$ and $c_m$ are given by $s_0^{ft}$ and $s_0^{mt}$ respectively. When modeling, the PD material constant $c$ from Eq. (2-37) will take the form:

$$c = \begin{cases} c_f + c_m & \text{for } \phi = \theta \\ c_m & \text{for } \phi \neq \theta \end{cases} \tag{2-38}$$

The equations defining the values of $c_f$ and $c_m$ are derived by Oterkus et al.[36] as:

$$c_f = \frac{Q_{11} - Q_{22}}{\frac{1}{2}\sum_{q=1}^{Q} \xi_{qi} V_q} \tag{2-39}$$

$$c_m = \frac{24 Q_{12}}{\pi t \delta^3} = \frac{8 Q_{22}}{\pi t \delta^3} \tag{2-40}$$

$\nu_{12} = 1/3$ in case of plane stress or $\nu_{12} = 1/4$ in case of plane strain.

### 2.5.3 Critical stretch and damage initiation

Damage can be introduced in the peridynamic calculation by defining failure laws based on a critical stretch between material points and removing the pair-wise force interaction once that value is reached. This principle is shown in Figure 2-9. In the figure, a peridynamic material point

grid is shown with a crack line and all pair-wise of material point $i$ within its neighborhood $\mathcal{H}_{\mathbf{x}}$. The failure of material point $i$ is modeled by removing all bond-forces running through the crack, marked dashed red. When this is done for all bond-force vectors between all material points within the body, a crack front will form naturally without the use of special techniques.

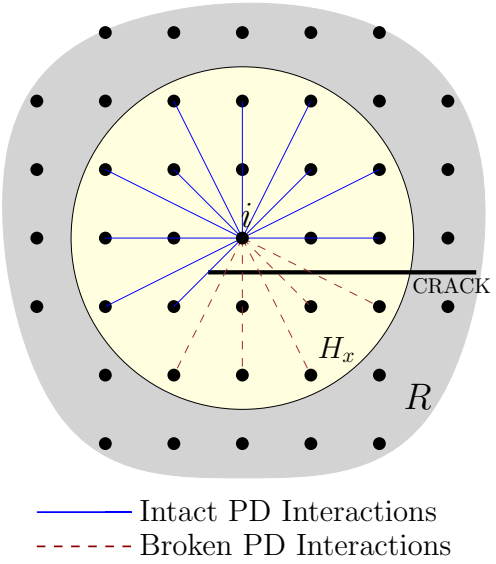


**Figure 2-9:** Schematic representation of a crack within a PD body. The pair-wise bond-forces of point $i$ running through the crack, marked dashed-red, are eliminated.

The damage progression is included by defining a stretch limit or critical stretch value $s_0$. Once the stretch between two material points reaches this value, the pair-wise force between those material points cease to exists and is removed from the calculation.

Mathematically, failure is added to the calculation by multiplying the force relation $\mathbf{f}$ given in Eq. (2-37) with the failure parameter derived by Silling[31] as $\mu(\mathbf{x}'-\mathbf{x},t)$. Resulting in the following equation for $\mathbf{f}$:

$$\mathbf{f} = \mu(\mathbf{x}'-\mathbf{x},t)cs\frac{\mathbf{y}'-\mathbf{y}}{|\mathbf{y}'-\mathbf{y}|} \tag{2-41}$$

The inexplicit expression for the failure parameter $\mu$, is defined by Silling[31] as:

$$\mu(\mathbf{x}'-\mathbf{x},t) = \begin{cases} 1 & \text{if } s(\mathbf{x}'-\mathbf{x},t') < s_0 \text{ for all } 0 < t' < t \\ 0 & \text{otherwise} \end{cases} \tag{2-42}$$

Although this equation is derived for an isotropic material, the directional property can be implemented by substituting the corresponding failure criteria from Eq. (2-43) for $s_0$, corresponding with the actual direction of the vector for the pair-wise bond force. The equations for the limit stretch for an elastic UD ply are derived by Hu et al.[37] as function of the ultimate stress and Young's modulus and are given in Eq. (2-43).

$$\begin{cases} s_0^{ft} = \dfrac{\mathbf{X}^t}{E_{11}}, & s \geq 0 \quad \text{Critical bond tensile stretch in fiber direction} \\ s_0^{fc} = \dfrac{\mathbf{X}^c}{E_{11}}, & s < 0 \quad \text{Critical bond compressive stretch in fiber direction} \\ s_0^{mt} = \dfrac{\mathbf{Y}^t}{E_{22}}, & s \geq 0 \quad \text{Critical bond tensile stretch in matrix direction} \\ s_0^{mc} = \dfrac{\mathbf{Y}^c}{E_{22}}, & s < 0 \quad \text{Critical bond compressive stretch in matrix direction} \end{cases} \tag{2-43}$$

The total damage at a material point, denoted by $\phi(\mathbf{x}, t)$, is derived by Silling[31] as the weighted ratio between the total number of interactions of a material point within $\mathcal{H}_{\mathbf{x}}$and the broken interaction. The extend of damage is defined by a value between 0 and 1. 0 Indicates no damage at a material point and a value of 1 indicates that all bonds are broken. However when a value reaches 0.5 during simulation, cracking is initiated. The equation for $\phi(\mathbf{x}, t)$ is derived as:

$$\phi(\mathbf{x}, t) = 1 - \frac{\int_{\mathcal{H}_{\mathbf{x}}} \mu(\mathbf{x}' - \mathbf{x}, t) d\mathcal{H}_{\mathbf{x}}}{\int_{\mathcal{H}_{\mathbf{x}}} d\mathcal{H}_{\mathbf{x}}} \tag{2-44}$$

## 2.6 Conclusion

For the fracture characterization of the cloth with Dyneema® fibers, the case of the flood barrier is translated to a laboratory setting. Since the thickness of the cloth is very small compared to the height and width, the cloth can be assumed thin-walled. Furthermore, since the material provided by DSM consists of a one-ply plain weave fabric, interlaminar defects like delamination can not occur physically during testing. So only intra-laminar fracture mechanics are taken into account, which are based on fiber and matrix failure. Also, since the structure is assumed thin-walled, the stress in the thickness direction can be neglected, eg $\sigma_z = 0$. Therefore the cloth can be assumed to be in a plane-stress condition.

Although a wide variety of geometries can be used for fracture toughness testing, only CC(T) specimens can be applied due to the thin and flexible nature of the single ply plain weave material. Large panel testing will be performed to investigate if infinite plate conditions can be assumed. Using CCT specimen for fracture mechanics testing does alter the boundary conditions with respect to the material of the tsunami barrier due to the fact that the left and right boundaries will not be constraint during testing. While in the tsunami barrier, connections between panels must be present in order to create cloths long enough to protect a beach.

The first estimation on the fracture toughness properties will be based on the anisotropic stress field equations within the LEFM theory, in order to investigate whether the assumptions on which the theorem is based on, holds when applied on the plain-weave fabric.

A numerical fracture simulation will be performed based on the peridynamics theory, PD is preferred over other techniques like XFEM or virtual crack closure technique (VCCT) since it is not depended on partial derivate equations, that by definition, do not exist along the boundary of discontinuities. Also, the method is particle based, preventing errors due to mesh distortion or hour-glassing effects when elements become distorted. Since the method is so far only developed for a UD lamina, the material model has to be extended for the implementation of plain weave properties.

# Chapter 3

# Research definition

The literature review in the previous chapter provides the theoretical content required for this research, in order to answer the main research question, as stated in the introduction:

> *"What are the intra-laminar fracture toughness characteristics of a notched cloth with Dyneema® Fibers under quasi-static loading and can a tool be developed to determine the critical damage of the flood barrier?"*

The main research question consists of two parts. The first part of the main research question focuses on the characterization of fracture toughness parameters, such as the crack intensity factor and strain energy release rate and the damage mechanism involved in the process. This will be done by performing fracture mechanics tests on material provided by DSM Dyneema® .

The second part, focuses on the application of fracture toughness theorem or numerical fracture models to develop a predictive method, which can be used to determine the allowable damage in the tsunami barrier. For the predictive model, two methods will be used. First, an analytical approach based on the linear-elastic fracture mechanics (LEFM). And secondly, a numerical damage progression model based on the peridynamics (PD) framework.

## 3.1 Sub-research question

For this research, only single ply material is available and since the material is flexible, only center cracked tensile specimen (CC(T)) specimens are suitable for fracture testing. This fits well in the case of the tsunami barrier, where the perforation is present within a large material field, such that infinite plate conditions might be assumed.

Based on this literature review, several subquestions have been formulated in order to answer the main research question.

1. Can the intra-laminar fracture toughness parameters of the cloth with Dyneema® fibers be determined using a CC(T) specimen?

2. Is the LEFM theory applicable to determine a critical stress intensity factor and strain energy release rate for the fabric based on CC(T) specimen, such that failure of the tsunami barrier can be described using these constants analytically?

3. Can the crack growth of the Dyneema® fabric be modeled with peridynamics and can the model be used to determine critical crack sizes in the tsunami barrier?

## 3.2 Scope

To investigate the fracture mechanics of the cloth with Dyneema® fibers, the case of the tsunami barrier, has to be translated into a laboratory setting, such that known fracture mechanics methods or numerical models can be compared with results from fracture toughness tests. Although a tsunami is a dynamic event, in order to meet the above mentioned requirement, all tests will be performed under quasi-static loading.

Also, this research focuses on the situation after initial damage initiation. It is not part of this research to investigate the damage initiation due to impact, since that would be an investigation in a complete different field.

The material for testing, is provided by DSM Dyneema® and consists of a single plain-weave ply, impregnated on both sides with an plastomer resin. Creating laminates out of the ply material is possible, but might alter the engineering properties. Therefore, all testing will be performed on a single ply material as it is delivered by DSM.

To develop a predictive method for the allowable damage of the flood barrier, known fracture mechanics concepts, first analytical, secondly numerical, will be used with their known material damage laws, as reviewed in Chapter 2. It is not within the time-frame of the research to develop a complete new material failure model.

# Chapter 4

# Methodology

In this chapter, the methodology of the research and the set-up of the experiments is explained. The research consists of 4 experimental parts:

- Coupon tests
- Fracture mechanics tests using center cracked tensile specimen (CC(T)) specimens
- Analytical solution using linear-elastic fracture mechanics (LEFM)
- Numerical simulation using the peridynamics (PD).

The coupon tests are required to determine the engineering constants, and main failure properties of the fabric as used in the classical lamination theory. The tests are defined in Section 4.1. Fracture mechanics tests will be performed on CC(T) specimens, with different dimensions and initial crack lengths. The different sizing in test specimens is done to investigate if any sizing effects are present. Different initial crack lengths to investigate the difference in finite and infinite plate theorem. Furthermore, the dimensions of the test specimens are contraint by the dimensions of the test bench.

In Section 4.3 the setup for mechanical testing is explained and how the test data is acquired. Section 4.5 contains the setup for the numerical simulation of this research.

## 4.1 Coupon tests

Tensile tests are performed to determine the engineering constants of the material and the main failure parameters. Tests are performed according to American Society for Testing and Materials (ASTM) standard test methods. In Table 4-1 an overview of used ASTM standards and corresponding parameters is given.

**Table 4-1:** Test standards for material property testing

| Standard | Parameters |
|---|---|
| ASTM-D3039[38] | $E_{11}, E_{22}, \mathbf{X}^t, \mathbf{Y}^t, \boldsymbol{\epsilon}_1^u, \boldsymbol{\epsilon}_2^u$ |
| ASTM-E132[39] | $\mu_{12}$ |
| ASTM-D3518[40] | $G_{12}, S, \gamma_{12}^u$ |
| ASTM-D792[41] | $\rho$ |

## 4.2 Fracture toughness tests

For fracture toughness testing, no standard test methods are defined for composite CC(T) specimens under plane stress conditions. Test methods developed for plastics, like ISO-13586[42], are usually defined for compact tension specimen (C(T)) or single-edge notched bend specimen (SE(B)) specimens. For metals, ASTM-E561[43] exist for K-R curve testing on C(T) and CC(T) specimens. This method is used as guideline for fracture toughness testing of the Dyneema® cloth CC(T) specimen.

### 4.2.1 Specimen design

#### Tensile test specimens

The dimension of the geometry according ASTM-D3039[38] is given in Figure 4-1. The test section is 150 by 25 $mm$ in length and width. The clamp area is 120 mm long, as the clamping area is maximized within the dimensions of the clamping plates of the test bench.

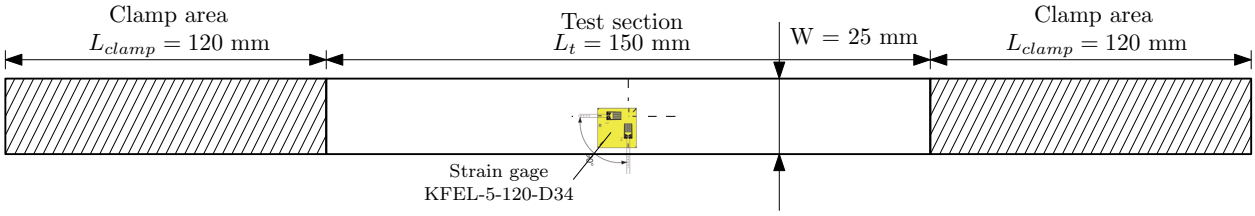


**Figure 4-1:** Dimension of the tensile tests specimens

At the central longitudinal axis of the tensile test specimen, a strain gage is applied to measure the longitudinal and transverse strain up to 10-15%. At the other side of the specimen, the speckle pattern is sprayed for the digital image correlation (DIC) system.

#### CC(T) specimens

For fracture testing, 3 different dimensions are used in widths of 120, 288 and 900 $mm$. The geometry of the test specimens is based on the available clamps and chosen such that relationship $3L \geq 2W$ holds, within the margin of the bench. The test samples used at the MTS 3500kN fatigue bench, are clamped using 2 cm diameter bolts. This requires the test samples to contain a hole pattern at the clamping area. The bolts have to follow the pattern of the clamp tool so that the center line of the test sample is aligned with the center line of the test bench. The dimensions of the CC(T) test specimens are given in Figure 4-2.

The initial crack lengths $2a_0$ are cut according to Table 4-2. Which also shows the number of specimens of each type and on which test bench they will be tested.

### 4.2.2 Specimen production

#### Cutting-tool

The material, as is delivered by DSM, is a finished product on a roll of 2.8 by 10 meters long, at which the fibers are already impregnated by the plastomer resin. Therefore, only cutting is required to produce the test samples. Dyneema® is known for its difficulty to cut and due to the size of the specimens up to 900 by 1620 mm, the only possible way to accurately cut specimens is by using an automated cutting machine. In this research a Gerbercutter DSC2500[44] is used which is available in the ASML composite lab. The machine consists of a vacuum table and a tool head which allows the cut-tool to rotate 360°. This allows the machine to cut circular holes as well. The cut pattern, as shown in Figure 4-2, is drawn using Catia and loaded into the pre-processing computer of the Gerbercutter through a .dxf file. This allows the machine to program the entire path of test sample at once, including the hole pattern and initial crack, reducing the change of misalignments. For cutting, a straight knife is used with an applied pressure of 35 bar. Although Dyneema® is difficult to cut, the cut edges were smooth, straight and no frayed fibers at the edges where present.

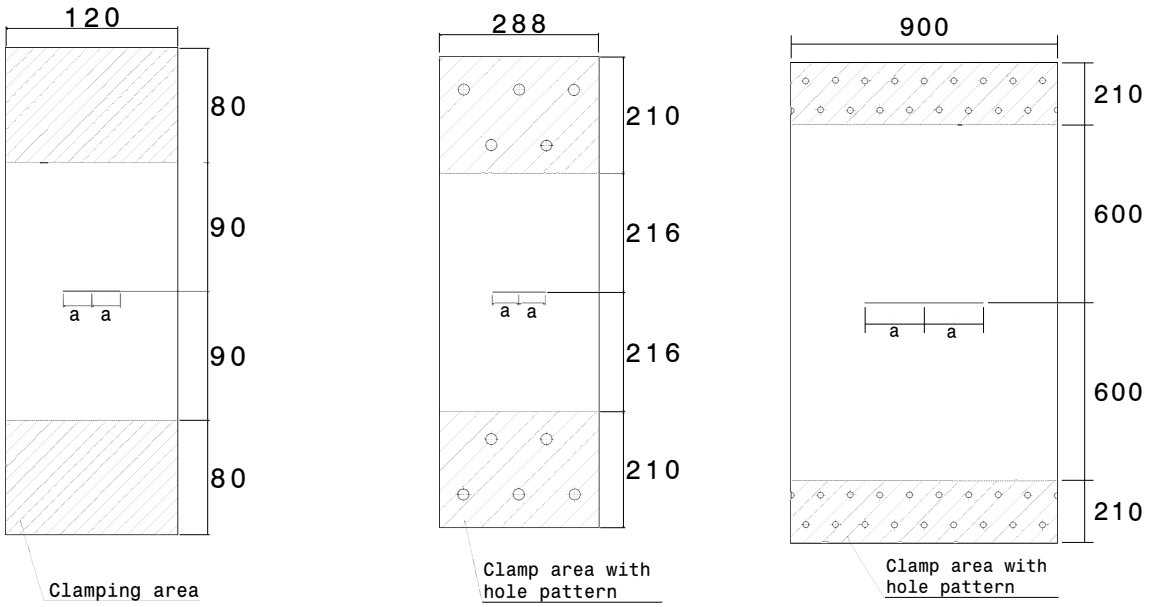


**(a)** Specimen size of the small scale fracture toughness test

**(b)** Specimen size of the medium scale fracture toughness test

**(c)** Specimen size of the large scale fracture toughness test

**Figure 4-2:** Dimension of the geometry of the CCT test specimens for the fracture toughness testing, the initial crack length a is variable. All dimensions are shown in millimeters.

**Table 4-2:** Fracture Toughness Test Matrix

| Width | Initial crack length | Ratio | Number of specimens | Bench |
|---|---|---|---|---|
| 2W | $2a_0$ | $\frac{2a_0}{2W}$ | n | |
| mm | mm | - | - | |
| 120 | 0 | - | 2 | Zwick 250kN |
| 120 | 30 | 0.25 | 2 | Zwick 250kN |
| 120 | 40 | 0.333 | 3 | Zwick 250kN |
| 120 | 50 | 0.417 | 2 | Zwick 250kN |
| 288 | 0 | - | 1 | MTS 3500kN |
| 288 | 96 | 0.333 | 3 | MTS 3500kN |
| 900 | 0 | - | 1 | MTS 3500kN |
| 900 | 200 | 0.222 | 1 | MTS 3500kN |
| 900 | 250 | 0.278 | 1 | MTS 3500kN |
| 900 | 300 | 0.333 | 3 | MTS 3500kN |
| 900 | 350 | 0.389 | 1 | MTS 3500kN |
| 900 | 400 | 0.444 | 1 | MTS 3500kN |

## 4.3 Test-bench setup

The mechanical tests are performed to determine the material properties and fracture toughness parameters. Three test benches are used in this research:

- Zwick static bench, max load 250kN, with hydraulic clamps
- MTS Fatigue bench, max load 3500kN, with bolted clamps

The tensile tests and small scale fracture tests are performed on the Zwick Tensile Machine which

has hydraulic clamps and up to 450bar of clamping pressure. The limit load of the bench is 250kN, which is well above the expected failure force of the notched Dyneema® fabric.

The medium and large scale fracture toughness tests are performed on the MTS 3500kN fatigue bench. In this case, specimens are clamped using bolts. To prevent slip of the specimen, the bolts are pre-tensioned at 750 $Nm$ of torque, which is the maximum allowable pre-tension on the bolts. Since the bolts have a diameter of 20 mm, in theory the 'clamp force' generated by the pre-tension of 750Nm, equals 187.5 kN. Which is calculated by the equation $T = KDP$. In which $T$ is the applied torque, $K$ the friction coefficient of steel equal to 0.2, $D$ the bolt diameter and $P$ the force. Since 21 bolts are used on one side, the total clamping force is 3937 kN. Divided by the area of the clamps, this will give a theoretical pressure of 21.6 MPa. This value can be considered as a theoretical value only. The actual axial force within the bolt due to tensioning is depended on several factors like the geometry of the bolts (tread length and pith), dissipation of torque due to plastic deformation of the bolt or the washers and the actual friction coefficient of the steel bolts and nut. Also, the torque is applied by using an analog wrench. Tese factors make it not possible to measure the actual closing pressure.

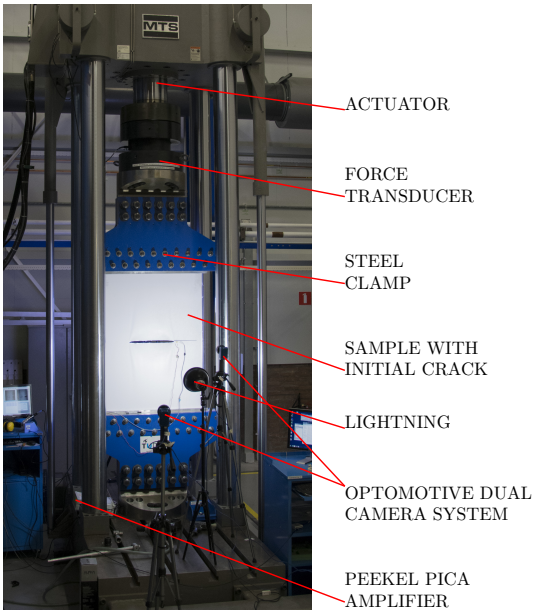


**(a)** Setup of the MTS fatigue bench with optomotive camera system and strain gage attached rigt of the crack tip.

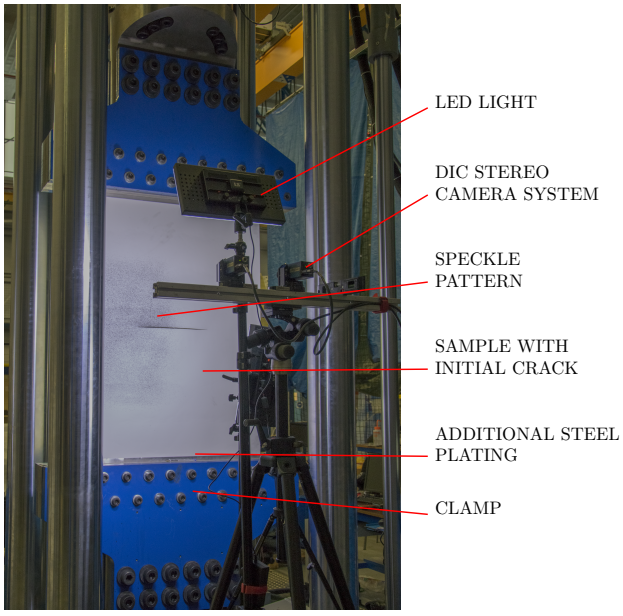


**(b)** Setup of the DIC camera system with the speckle pattern around the left crack tip.

**Figure 4-3:** Setup of the test bench with the DIC, optomotive camera system and peekel strain gage devices

A third bench, the MTS 250kN fatigue bench, is used for preliminary testing on specimens of 288 mm width, which are the dimensions of one of the available clamps. This bench is used to investigate test settings and the application of buckling guides. The results of those test for fracture mechanics testing were invalid, due to the fact that all specimens failed due to slip within the clamps, showing the difficulty in constraining the Dyneema® fabric. However, it showed the applicability of buckling guides to prevent out-of-plane deflection,e which will be explained in Section 4.3.3.

### 4.3.1 Test conditions

Both the tensile and the fracture tests are performed under displacement controlled quasi-static conditions with a loading rate of 2 $^{mm}/_{min}$, until ultimate failure occurs. Specimens are not unloaded

during the tests. All tests will be conducted at room temperature.

### 4.3.2 Specimen clamping

The specimens tested on the Zwick 250 kN machine, are clamped using the hydraulic clamps using steel plates with a dimension of 120x80 mm. The maximum pressure that can be applied by the bench is 450bar.

The specimens tested on the MTS 3500kN fatigue machine, are clamped using 2cm diameter bolts with a torque of 750 Nm per bolt. A total of 21 bolts is used at each side. The spacing between bolts at a row is 10 cm.

Due to the high clamping force, it is possible that the corners of the steel plates cut into the material, damaging the fibers and invalidating the tests. Therefore, additional steel plates are inserted, which are about 2 cm longer than the steel plates from the bench itself, as can be seen in Figure 4-4. The extra length prevented the sharp corners of the steel plates to cut into the material.

**Figure 4-4:** Additional steel plating, inserted in the bench to prevent cutting of the fibers

### 4.3.3 Application of buckling guides

During fracture toughness testing of laterally unsupported CC(T) specimens with relative small sheet thickness, the compressive stress that develops laterally due to tensile loading, may result in buckling of the areas above and beneath the crack. When buckling occurs, the validity of the $\mathcal{K}$ -test may seriously be compromised, according to Zhu et al.[45], especially when the compliance method is used to determine crack size. Buckling can be prevented by applying anti-buckling guides at area's where buckling is anticipated.

For initial fracture toughness tests of the Dyneema® fabric have been performed on the MTS 250kN fatigue bench. At these tests, plexiglass buckling guides were used separation by 0.8 mm. The results show that in case of the Dyneema® fabric, the effect of the buckling guides is limited due to buckling of the fibers on microscale between the plate, as can bee seen in Figure 4-5. To prevent micro-buckling, the buckling guides must be applied with a relative high pressure onto the surface of the fabric, which influence the force measured at the bench and squeezes strain gages in case they're applied. Or a second option is using very thick plexiglass plates. But a second drawback in using buckling guides, is that the DIC system must be calibrated through the glass and the refraction of light will decrease the accuracy of the correlation.

Based on the drawbacks and the limited effect of buckling guides for Dyneema® fibers, buckling guides are not used in this research further on, allowing out of plane deflection during the fracture

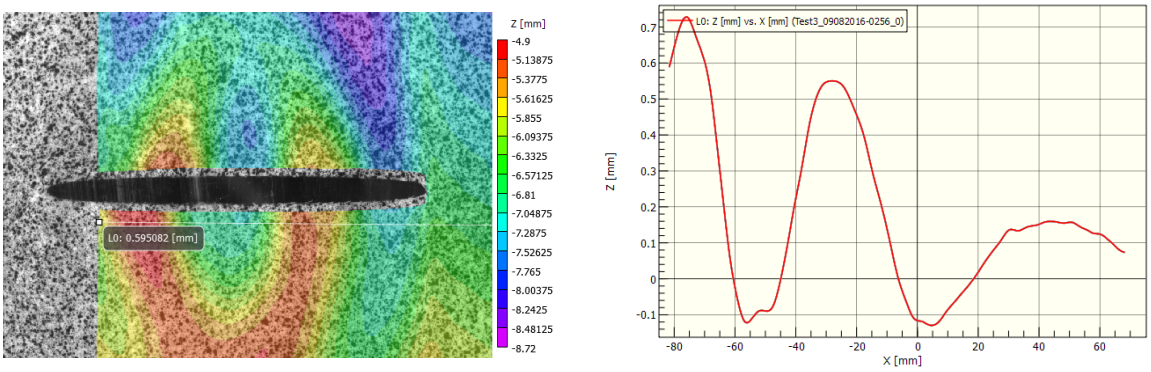


**(a)** Out of plane deflection of the lamina within buckling guides

**(b)** Graph of the defection in Z along the x-axis just below the crack.

**Figure 4-5:** Effect of the application of buckling guides on the out-of-plane deflection of the plate during testing.

toughness tests. However, de out-of-plane deflection will be similar to the in-service loading in case of the damaged tsunami barrier, where the water pressure acting on the membrane will deflect the edges of the crack.

### 4.3.4 Data acquisition

Data acquisition is performed by 4 systems:

- Test bench MTS or Zwick with multiXtens fine strain extensometer
- DIC system
- Strain gages with Peekel Pica Amplifier
- Optomotive camera system

In the following paragraphs each system is explained in more detail.

#### Force and displacement measurement

The force and displacements are both measured by the test machines. These values are required to determine the actual stress and strains on the specimen. The force is captured by a loadcell that is fit onto the cross-head of the machine. The displacement is measured by the cross-head travel. The force and displacement data are recorded in a data file and are send to the DIC camera system through an analog signal.

Additional the Zwick 250kN machine is equipped with a multiXtens fine strain extensometer for fine strain measurements between two given points. This extensometer is used during coupon testing.

#### Strain gages

Strain gages are used to measure the strain at certain locations of the specimen.

On to several test specimens strain gages are bonded, to measure the strains in longitudinal and transverse directions during testing, such that they can validate the calculated strains from the digital image correlation. The strain gages are of type KFEL biaxial high-elongation gages, containing two strain foils aligned at 90° with respect to each other. This allows the gage to measure both the tensile and the transverse strains. This type of strain gage is chosen since it has a high

strain range of max 15%. The properties are given in Table A-1. The voltage of the strain gages are amplified by Peekel Picas Multichannel Amplifier. The amplification settings are given in Table A-2. The signals are send to both the bench and the DIC system for comparison between the strains measured by the DIC and by the strain gages. One problem of applying strain gages onto the fabric, is the fact that Dyneema® and the plastomeric resin used are difficult materials to bond to, so during testing it must be monitored if the bonding holds and the signal of the strain gages are a representative measure of strain.

### Digital image correlation (DIC)

To obtain a full strain field, such that the stress intensity at the crack-tip can be determined, digital image correlation (DIC) is used. DIC consist of a stereo camera setup which captures images on an interval base. The setup is shown in Figure 4-3b. The camera's consists of a grey-tone optical sensor with a resolution of 4MP. System calibration and image capturing is performed using the VicSnap software of Correlated Solutions. VicSnap can be programmed to acquire image on an interval basis independently, or it can be triggered by the bench when the MTS machine is used. It is not possible to trigger the camera's with the Zwick bench, due to limitations in de Zwick software. The stereo set-up of the camera's allows the DIC to reconstruct the 3-dimensional surface of the body, such that out-of-plane deformations can be determined.

DIC works by the principle of calculating the displacement of the surface of a body, by performing a correlation between speckles on the the surface of the body. When a body deforms, the local displacement between speckles changes and by calculating the relative displacement between the speckles, the local strains can be determined. On the surface of the test specimens, the speckle pattern is applied by gently spraying black paint from an aerosol can. The optimal speckle size, according the the DIC manual is 3x3 pixels. There is however, no method available to control the speckle-pixel ratio, since the distance of the camera's is variable with respect to the test specimen and the spraying method does not allow proper size control of the speckles themselves. Therefore, at each test the system is re-calibrated.

With each image capture, VicSnap creates a data file in which the time and step is recorded, together with 4 analog input signals. 2 ports are reserved for the current load and displacements from the test-bench, the other two are used for the signal of the strain gages if applied. At each DIC image, therefore the load, displacement and if applicable the voltage from the strain gages are known.

Post-processing of the DIC images is performed using Vic3D v7[46] software which provides several correlation algorithms. For this research, the zero-normalized squared differences correlation zero-normalized squared differences correlation criterion (ZNSD) algorithm is used, which is unaffected by offset and scale in lightning. Details of this algorithm can be found in Sutton et al.[47]. For post-processing, an area if interest is marked, and a subset size and step-size must be determined. Larger subset sizes lead to better traceability of pixel groups within the subset, but decreases the accuracy. While a smaller subset may lead to areas where no displacement can be detected. The actual stepsize is determined for each sample separately based on the size of the largest paint dots. In this research, the subset size is usually around between 27 and 31 pixels. The step-size is the height and width grid-spacing between analysis points during correlation. A smaller step-size leads to more accurate correlations, at the cost of more computational time. The step-size should never be larger than half the subset size and in this research, a step-size of 4 is used. Additional settings for the DIC correlation are given in Table A-3.

### Optomotive camera system

The optomotive camera systems is a dual camera system with 4 megapixel sensors. The system is used to take detailed photos of areas of interest, especially around the crack tip. It cannot be used for displacement or strain analysis like the DIC system. The cameras are remote controlled and can by triggered by a time interval or as with the DIC by the MTS machine. If controlled by the MTS bench, the camera can be triggered at certain force interval. Advantage of this system is that the DIC and de Optomative systems can be triggered at the same time.

### Set-up data acquisition

The machines mentioned in the previous paragraphs will be interlinked with each other, such that data can be recorded simultaneous. The setup of the various measurement devices is given in Figure 4-6.

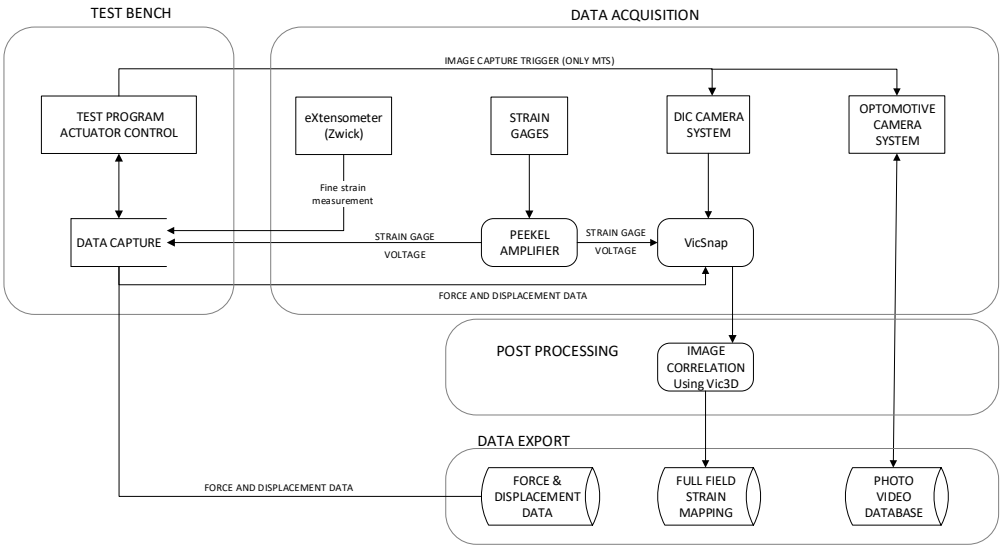


**Figure 4-6:** Flowchart of data acquisition setup

## 4.3.5 Microscopy

In addition to the data generated by the test bench, DIC, strain gages or optomotive, investigation on the fracture surface can be performed by visible inspection using microscopes. Two types microscopes are available at the DASML facility, the Leica optical microscope and the JEOL scanning electron microscopy (SEM). The Leica optical microscopes has a magnification up to 250 times and is especially used to examine cross-section area of laminates and is equipped with camera's to obtain and save the picture. The software used also provides measurement tools. The second microscope available is the JEOL SEM, which can be used to examine the surface of crack lines and to measure the chemical composition of the material. Since the electron microscope has a magnification op to a million times, it is able to examine the individual fibers, matrix and contact areas.

## 4.4 Analytical solution using LEFM

The LEFM, reviewed in Section 2.4, is an approach to determine the stress field around the crack tip and failure loads of the panels analytically. The procedure will be based on the stress equations around the crack tip of a sharp notch within an anisotropic plate, as derived by Lekhnitskii et al.[12] and given in Section B.1.1. As loading condition, the results from the DIC analysis and with its actual load will be used to compare the analytical stress field with the stress field obtained by the DIC.

The required stress intensity factor $\mathcal{K}_I$ will be calculated following the procedure in Section 2.4.5.

First, the method will by applied to the small test specimen with an width of 130mm initial crack of 40 mm. If the method proves applicable, for all other test specimen the strain energy release rate (SERR) will be determined as well.

## 4.5 Numerical fracture simulation

To develop a progressive damage model, peridynamics (PD) is used. The model will be build corresponding with the fracture toughness test specimens, such that geometry and boundary conditions are similar.

### 4.5.1 Discretization

When a body is discretized, the body is divided into cubic sub-domains as shown in Figure 4-7. For each material point $i$, is determined which particle is within its neighborhood, such that the pairwise bond force can be assigned, as shown in Figure 4-7a. When using a horizon radius of $\delta = 3\Delta x$, each material point has 28 pairwise bond functions. This step is repeated for each material point in $\mathcal{R}$, with as results a grid of pairwise interactions as shown in Figure 4-7b.

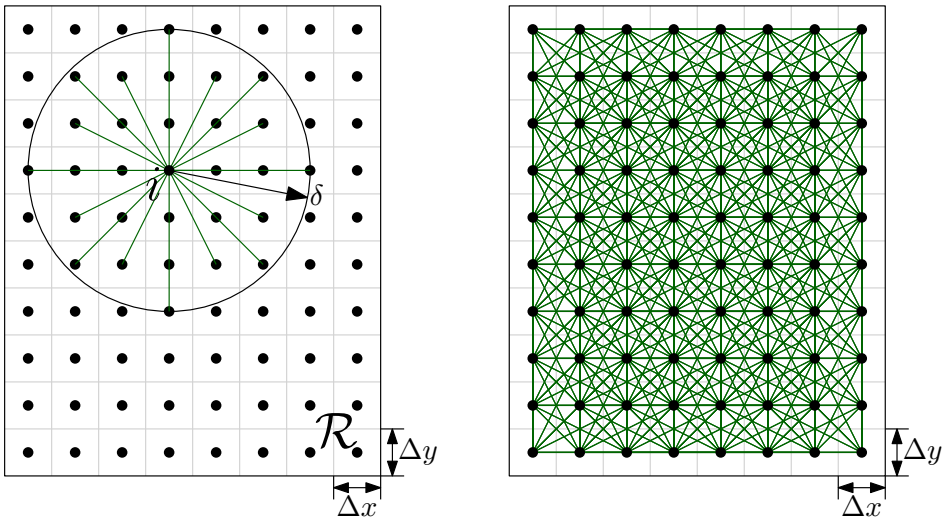


**(a)** Interaction of material point i with all particles within it's neighborhood

**(b)** Total grid of pairwise bond forces between all particles in the body

**Figure 4-7:** Discretization of body $\mathcal{R}$ into PD subdomains

#### Equation Of Motion

Since the main equation of motion of the PD is based on an integro-differential equation, as given in Eq. (2-35), a collocation method is used to solve the equation numerically. The main equation of motion is rewritten by Madenci et al.[34] to:

$$\rho(\mathbf{x}_i)\ddot{\mathbf{u}}(\mathbf{x}_i, t) = \sum_{j=1}^{M} \mathbf{f}(\mathbf{u}(\mathbf{x}_j, t) - \mathbf{u}(\mathbf{x}_i, t), \mathbf{x}_j - \mathbf{x}_i) v_j \mathcal{V}_j + b(\mathbf{x}_i, t) \tag{4-1}$$

When the forces of material particle $x_i$ are integrated over its horizon, the entire volume $\mathcal{V}_j$ of material point $x_j$ is taken into account. $v_j$ is the volume correction factor, to improve the approximation for domains that fall partly put of the horizon $\delta$ of particle $x_i$. The equations to determine the value of the volume correction factor are given in Section C.1.4.

#### Time scheme

When the acceleration $\ddot{\mathbf{u}}_i$ is determined at time step $n$, explicit forward and backward difference techniques can be used to determine the velocity and displacement at timestep $n+1$ in two steps. First the velocity $\dot{\mathbf{u}}_i$ at timestep $n+1$ is determined from the known acceleration $\ddot{\mathbf{u}}_i^n$ and the velocity $\dot{\mathbf{u}}_i^n$ at timestep $n$ using the following relation:

$$\dot{\mathbf{u}}_i^{n+1} = \ddot{\mathbf{u}}_i^{n+1} \Delta t + \dot{\mathbf{u}}_i^n \tag{4-2}$$

Next, with the velocity $\dot{\mathbf{u}}_i^{n+1}$ at timestep $n+1$ known, the new displacement $\mathbf{u}_i^{n+1}$ at time step $n+1$ is determined as:

$$\mathbf{u}_i^{n+1} = \dot{\mathbf{u}}_i^{n+1} \Delta t + \mathbf{u}_i^n \tag{4-3}$$

This process is repeated at every $(n+1)^{th}$ time step for all material points $(i+1)^{th}$.

### 4.5.2 Boundary conditions

The application of boundary conditions within the PD theory is different compared to finite elements method (FEM) methods. Since PD utilizes integro-differential equations, tractions or forces can not be applied directly cause then their volume integrations result in zero values. Boundary conditions are therefore applied as body forces, displacements or velocities over the incremental volumes at the boundary regions.

Two types of boundary conditions will be applied. For the validation, where no failure is included a pressure boundary will be applied, such that the displacement over the lamina can be calculated and compared with an analytical solution. For the fracture models, a velocity boundary condition will be applied. The boundary conditions are applied on a certain boundary region as shown in Figure 4-8. Extra material points are added at the top and bottom and marked as no-fail zones. The number of rows added, depends on the type of boundary condition.

#### Displacement controlled boundary condition

When a displacement controlled boundary conditions is used, as visualized in Figure 4-8a, the material points assigned to the boundary layer are set to a constant velocity. Denoting $V_{in}$ the initial boundary velocity, the boundary condition is written as:

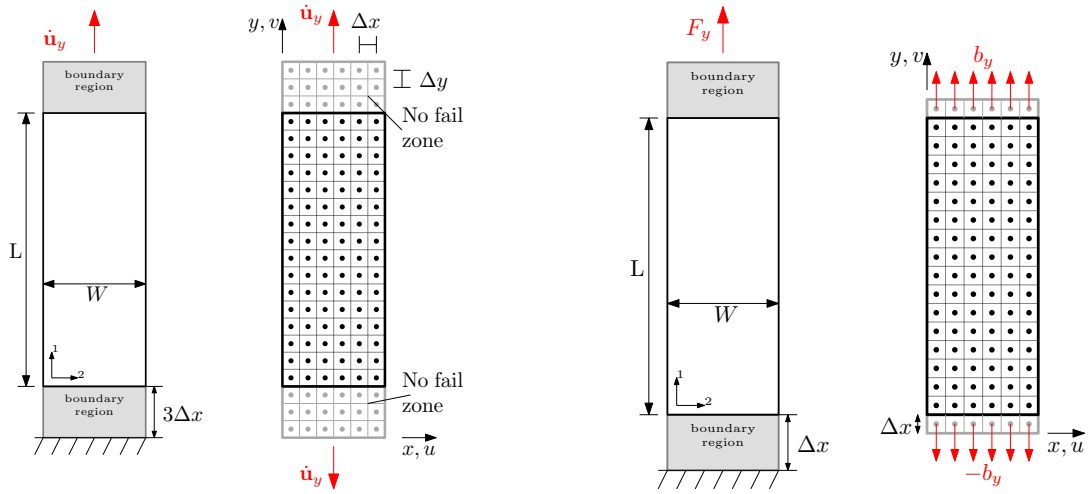


**(a)** Velocity boundary conditions **(b)** Force boundary condition

**Figure 4-8:** Visualization of the boundary conditions of the PD simulation compared with the boundary conditions at the test bench.

$$\begin{cases} \dot{\mathbf{u}}_{bnd}(x,t) & = 0 \\ \dot{\mathbf{u}}_{bnd}(y,t) & = V_{in} \end{cases} \tag{4-4}$$

When a velocity boundary condition is applied, the thickness of the boundary layer will be set to $3\Delta x$. This is done since the material points at the boundary suffer a decrease in stiffness due to the lower amount of bond-forces at the edges of a lamina. This may result in early failure along the edge of the boundary. And with a boundary region of $3\Delta$, the first row of material points which can develop damage has the same amount of bond-forces in the loading direction as the inner region of the lamina.

#### Force controlled boundary condition

For force controlled boundary conditions, the force $F$, applied in y-direction, is divided into incremental forces acting over over the incremental volumes of the material points in the boundary layer, as shown in Figure 4-8b. Let $\Delta$ be the spacing between material points, $N_x$ number of divisions of material points in x-direction and $N_{bnd}$ the number of divisions of material points in y-direction within the boundary area. The incremental volume of each material point, assuming cubic subdomains, is $\Delta V = \Delta^2 \cdot t$. The total volume of the boundary layer than equals: $\Delta V_\Delta = N_x \cdot N_{bnd} * \Delta V$. The applied force is divided over all material points within the boundary layer. The applied body force density per incremental volume in y-direction $b_y$ becomes:

$$b_y = \frac{F}{\Delta V_\Delta} \tag{4-5}$$

### 4.5.3 Initial crack

The initial crack can be implemented during the discretization process by removing all pairwise interactions that run through the crack surface. The process is shown in Figure 4-9. Figure Figure 4-9a shows the location of the initial crack within $\mathcal{R}$. All interaction between the material points are shown in green. All interactions that run through the crack, marked red in Figure 4-9b, are eliminated from the calculation. The resulting grid in which the crack-line is cleared from pair-wise force interactions is sketched in Figure 4-9c.

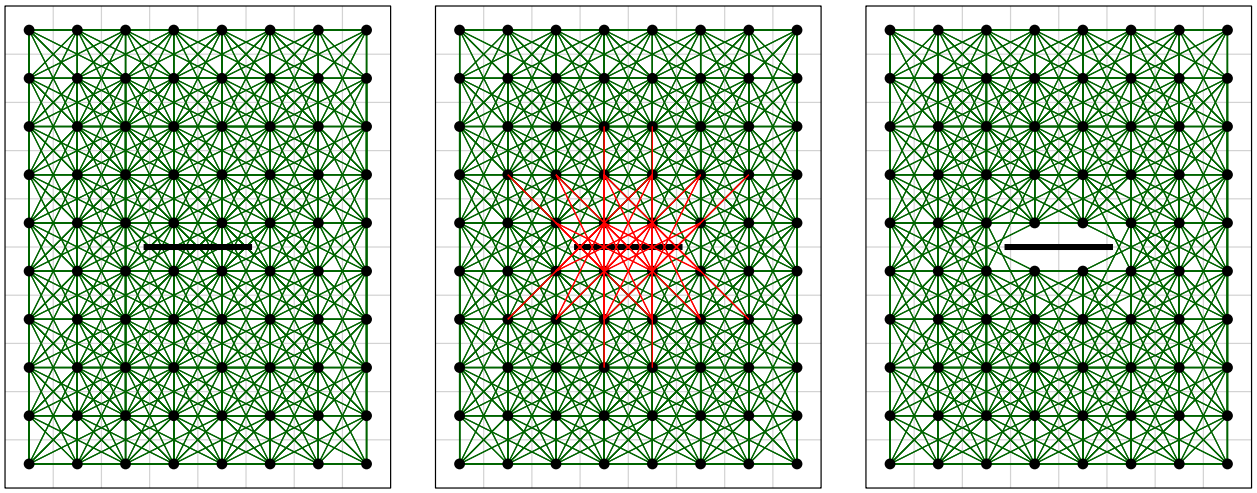

**(a)** Definition of the crack line within body $\mathcal{R}$

**(b)** All pairwise bond forces running through the crack, marked red, are eliminated

**(c)** Resulting grid of pairwise bonds with initial crack

**Figure 4-9:** Definition of a crack within the PD body

### 4.5.4 Model flowchart

The codes for the peridynamic simulation will be written in MatLab. The codes are based on the examples Fortran codes from Madenci et al.[34], which are translated to the MatLab language such that an initial framework is present. The program consists of 3 main parts which are visualized in the flowchart of the program shown in Figure 4-10. The first part is the pre-processing in which the variable input data is defined, like geometry, material properties, time step and initial crack length. Those are used to determine the peridynamic parameters. With the input data, the geometry is discretized and the bond-force vectors between the material points are determined. If applicable, the crack line in defined by eliminating the bond-force vectors that run through the crack. At last, the initial surface and volume correction factors are determined and the boundary conditions are applied.

Part 2 is the time integration. At each timestep, the surface and volume correction factors are redetermined for the force-vector, based on stretch between the material point at the current time step. This is required since the fracture surface may increase. Next, the sum of all forces acting on the material point are determined, using the current displacement vectors and stretch functions of the material. When a bond vector reaches the critical stretch, the bond failes and is eliminated from the calculation.

Last part of the code is the post-processing. In this step the data for the crack opening, crack growth is analyzed and figures, graphs and video files are exported.

An example MatLab code is added in App. C.2.

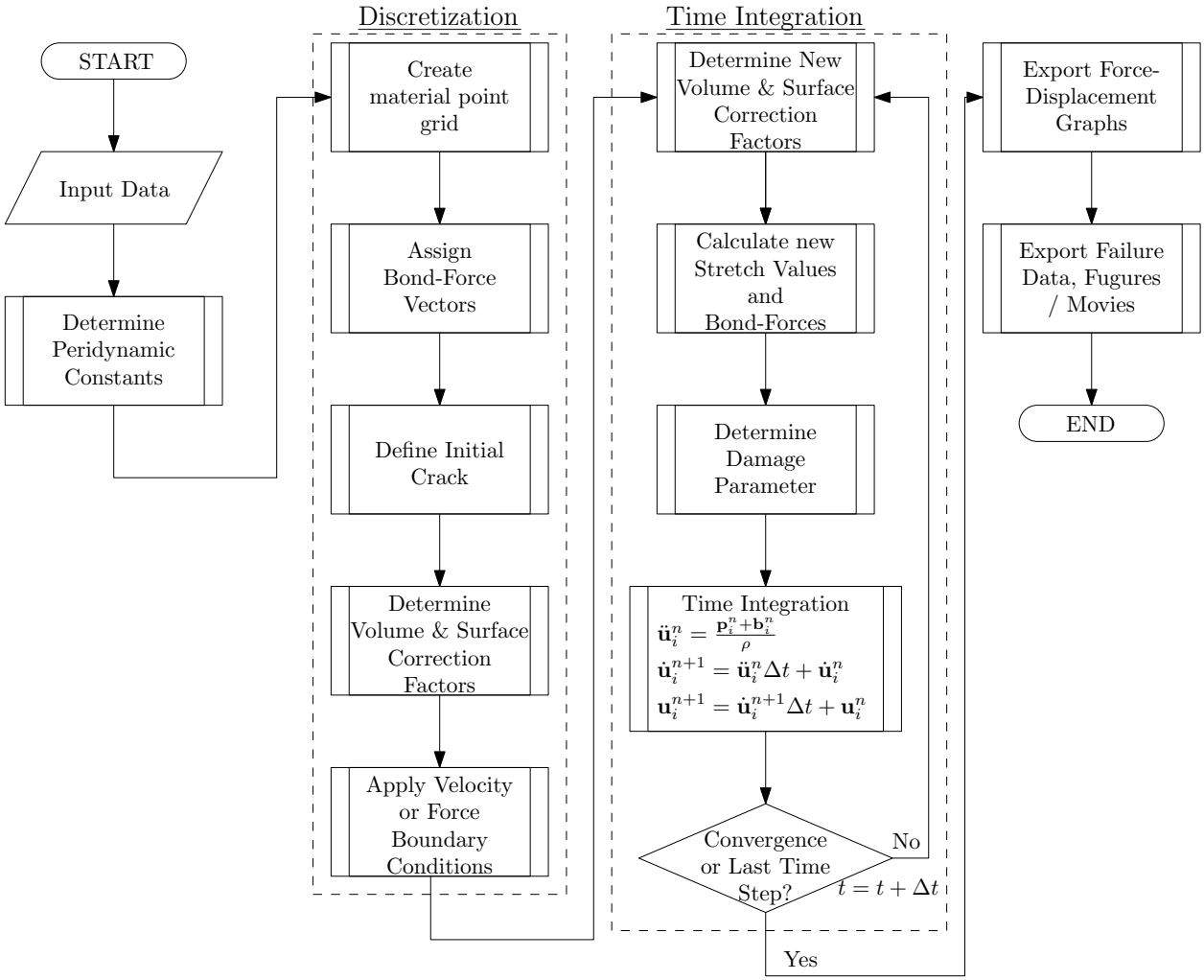


**Figure 4-10:** Flowchart of the peridynamic numerical fracture model

# Chapter 5

# Material Physical Properties and Engineering Constants

Before the fracture toughness properties of the Dyneema® fabric can be determined, the general physical properties and engineering constants must be known. Since the fabric itself is delivered already impregnated with the Queo 8210 plastomer, the properties determined are for the complete ply on macroscopic level. That means that nonlinear effects, which are present in fabric due to the waviness of the fibers, are already included in moduli and the failure parameters. To minimize any calculation or modeling errors, the material has be characterized as accurate as possible. Therefore, all tests are performed using the procedures from ASTM standard test methods and the mean values are determined using the statistical law from ASTM-D3039[38] as given in Section A.2.1. To determine the strains in the test specimens, a combination of strain gages and digital image correlation (DIC) is used, so that values can be compared with respect to each other and measurement errors can be limited.

The compressive values of the fabric will not be tested. Due to the thin and flexible nature of the material, immediate fiber buckling will occur when a compressive load is applied. It is therefore impossible to determine compressive values. They are however, compressive stiffness values required for the simulation, since tensile loading will induce transverse compression and otherwise elements will collapse. Therefore, the values will be set equal to the tensile values when required.

## 5.1 Physical properties

Two physical properties are determined, the ply thickness and density. The thickness is required to determine the stress inside the ply. The density is required to for the application of the equations of motion used in the peridynamic simulations.

### Ply thickness

The thickness is measured on several specimens, using a micrometer with flat anvil. The test results are given in App. A.2.2 and the raw measurement data in Table A-6. Due to the waviness of the ply, the thickness of the cross-section is not constant, as can be seen in the microscopic picture of the cross-section shown in Figure 5-2a. This irregularity is ignored in this research and an average value of the ply thickness used. The results of the tests are given in Table 5-1.

### Ply density

The density of the ply is required for the numerical simulation. The density is measured according to ASTM-D792[41] standard test method which is based on Archimedes' principle. The law states that the upward buoyancy forces acting on a body when submerged in a auxiliary liquid, equals the weight of the fluid displaced by the body. The test method is further explained in App. A.2.2 and the measurement data is in Table A-4.

The determined values for the thickness and density are given in Table 5-1.

**Table 5-1:** Physical properties of the Dyneema® fabric

| Property | Symbol | Unit | Value | Std Deviation | Relative error |
|---|---|---|---|---|---|
| Density | $\rho$ | $^{g}/_{cm^3}$ | 0.89 | 0.0099 | 1.1% |
| Thickness | $t$ | $mm$ | 0.71 | 0.0082 | 1.15% |

## 5.2 Engineering constants

The engineering constants are determined using the stress-strain curves of the tensile tests, which are given in Figure 5-1. Figure 5-1a shows the stress-strain relations for the tensile tests in warp direction. The graphs show a small nonlinear region at the start, followed by a straight line up the maximum stress where brittle failure occurs. No yielding is visible. The tensile tests in weft direction, given in Figure 5-1b show that the material pre-stretched up to a transition strain $\epsilon_{trans} = 8\%$, before the fibers are starting to take up loads. At ultimate stress, brittle failure is observed.

The third graph, Figure 5-1c, shows the in-plane shear stress-strain curve. The material properties in this direction is mainly depended on the properties of the plastomer resin. The curves shows a clear nonlinear stress-strain relation, with a failure strain of more than 30%. The failure stress is low and varies between the 5 and 6 MPa.

The last graph, Figure 5-1d, shows the longitudinal strain versus the transverse strain for the tensile tests in warp direction. These graphs are used Poisson's ratio, $\nu_{12}$ by applying Eq. (A-4).

From the test data, the engineering properties are determined. The statistical method and determinations of the mean values and relative errors is given in Section A.3. To calculate the derivatives of the slopes of the curves in order to determine the Young's moduli, the straight sections are taken. For the Young's modulus in weft direction, two derivatives are determined for each and for each section an transverse Piosson's ratio $nu_{21}$ is determined using Eq. (2-8). The calculated engineering constant are given in Table 5-2, and the statistical data is given in Table A-7.

**Table 5-2:** Dyneema® fabric engineering constants

| Constant | Symbol | Value | Unit | Comments |
|---|---|---|---|---|
| Youngs Modulus, warp dir | $E_1$ | 8.62 | GPa | |
| Youngs Modulus, weft dir | $E_2$ | 0.123 | GPa | For $0 < \epsilon_2 < 8\%$ |
| | $E_2$ | 5.07 | GPa | For $\epsilon_2 > 8\%$ |
| Shear Modulus | $G_{12}$ | 0.0248 | GPa | |
| Poisson's ratio dir 12 | $\nu_{12}$ | 0.37 | - | |
| Poisson's ratio dir 21 | $\nu_{21}$ | 0.0053 | - | For $\epsilon_2 < 8\%$ |
| | $\nu_{21}$ | 0.22 | - | For $\epsilon_2 \geq 8\%$ |

Similar to the engineering constants, the failure parameters are extracted from the test data. The values are given in Table 5-3 and the statistical data is given in Table A-7.

Based on the stress-strain graphs, showing the clear difference in behavior with respect to the different orientations, the material is nonlinear and anisotropic. The weft-direction will therefore be modeled as a bilinear material. This resulted in the calculation of two transverse Poisson's ratios and two stiffness matrices for each part of the stress-strain curve.

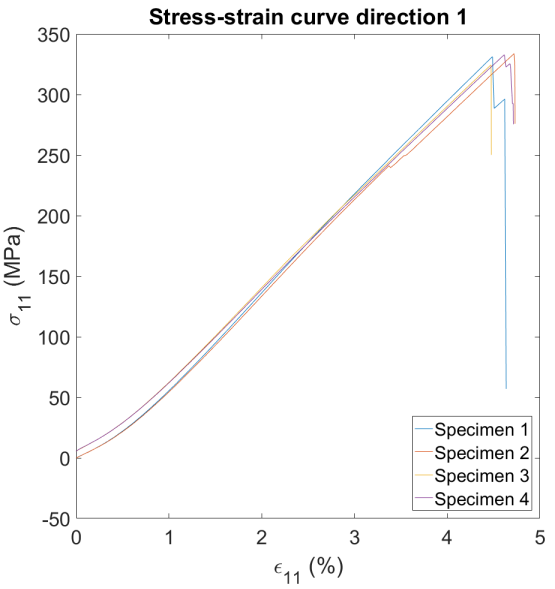


**(a)** Stress-strain curves with loading in the warp direction

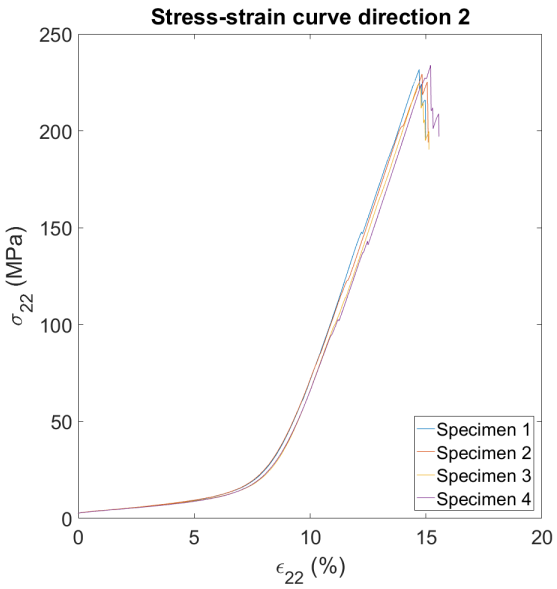


**(b)** Stress-strain curves with loading in the weft direction

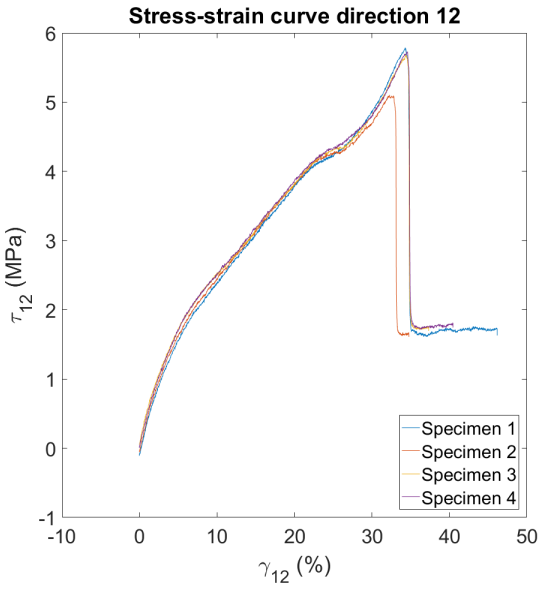


**(c)** Stress-strain curves with loading in the shear direction

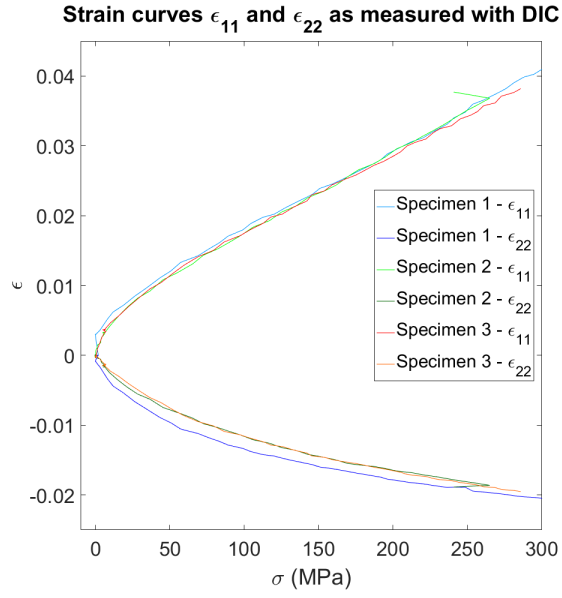


**(d)** Longitudinal versus the transverse strain, loading applied in warp direction

**Figure 5-1:** Stress-strain curves of the tensile tests in warp, weft and shear directions.

## 5.3 Microscopic analysis

To investigate why the difference in stiffness and tensile failure strength exist between the warp en weft direction, samples are investigated under the Leica optical microscope. Two cross-sections of the ply are shown in Figure 5-2. The left image, Figure 5-2a is taken when looking onto the cross-sectional area of the fibers in warp direction, with the weft direction running horizontally over and underneath the fiber yarns. The right image, shows the cross-sectional area of the fibers in running in weft direction, with the warp fiber bundle running from left to right.

**Table 5-3:** Dyneema® fabric failure properties

| Constant | Symbol | Value | Unit |
|---|---|---|---|
| Max Tensile stress, warp dir. | $\mathbf{X}^t$ | 331 | MPa |
| Max Tensile strain, warp dir. | $\epsilon^t_{x_u}$ | 4.2 | % |
| Max Tensile stress, weft dir. | $\mathbf{Y}^t$ | 229 | MPa |
| Max Tensile strain, weft dir. | $\epsilon^t_{y_u}$ | 13 | % |
| Max Shear Stress | $\mathbf{S}$ | 5.6 | MPa |
| Max Shear strain | $\gamma_{xy_u}$ | 36 | % |

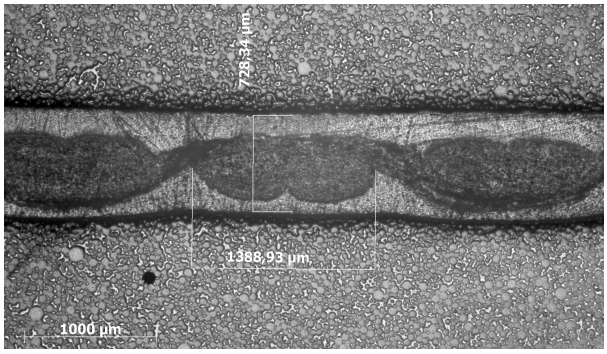


**(a)** Cross-section warp direction 2.5x magnification

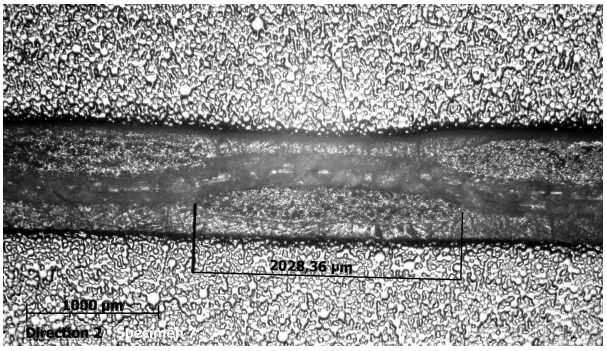


**(b)** Cross-section weft direction 2.5x magnification

**Figure 5-2:** Miscroscopic analysis of the cross section of the Dyneema® fabric.

When the two images are compared, a clear difference between the two cross-sections can be distinguished. Figure 5-2a shows fiber bundles that are quite compact with a width of about 1.3 mm. The height is approximate 0.43 mm. The weft-fibers, show a high waviness path around the fiber-bundles, forcing spacing between the warp yarns. in Figure 5-2b, the fiber bundles have a much more flat cross-sectional area, with a width of 2 mm. The warp-fibers, follow a rather straight path between the bundles. It can therefore be explained that the first 8% of stretch in the stress-strain curve of the weft direction, is caused by straightening the waviness out if the fiber bundle. This occurs to a lower extent in the warp direction, since the fiber path shows already a rather straight line. The difference in strength can be explained by the fact that the remaining waviness of the path in weft direction can never be a straight as the path in warp direction, due to the higher thickness of the fiber bundle in warp direction. This remaining curvature reduces the strength of the fibers, due to the loading of the fibers in shear locally.

## 5.4 Construction of the stiffness matrix

With the determined values for the Young's modulus and poisons ratio's the stiffness and compliance matrices can be constructed by substituting the values from Table 5-2 into the 5 equations given in Eq. (2-5).

The resulting stiffness matrices are given in Eq. (5-1).

$$\mathcal{Q}_{1,2} = \begin{cases} \begin{bmatrix} 8.64 & 0.046 & 0 \\ 0.046 & 0.123 & 0 \\ 0 & 0 & 0.0248 \end{bmatrix} (GPa) & \text{for} \quad \epsilon < \epsilon_{trans} \\ \begin{bmatrix} 9.37 & 2.04 & 0 \\ 2.04 & 5.5 & 0 \\ 0 & 0 & 0.0248 \end{bmatrix} (GPa) & \text{for} \quad \epsilon >= \epsilon_{trans} \end{cases} \tag{5-1}$$

Evenso, the compliance matrices can be constructed by substituting the values from Table 5-2 into the set of equations given in Eq. (2-7). The resulting compliance matrices are given in Eq. (A-7).

## 5.5 Conclusion

In this chapter, the material properties of the fabric with Dyneema® fibers have been determined by tensile tests according to ASTM standard test methods. The results show a very strong anisotropic and non-linear behavior of the fabric. The Stress-strain curves in warp direction, starts with a small nonlinear displacement, followed by a straight stress-strain curve with a Young's Modulus of 8.62 GPa. Brittle fracture occurs at a stress of 331 MPa. The stress-strain curves in weft direction however, non-linear part up to a strain of 8% where the fibers are stretched first. Followed by a straight stress-strain curve with a Young's Modulus of 5.07 GPa. Brittle failure occurs at a stress of 229 MPa. The bilinear stress-strain curves forces two different transverse Poisson's ratio's, with their intersection at 8% strain. The shear stress is carried mostly by the plastomer resin, and takes up a strain of 36% before failure. The shear failure stress is very low with a value of 5.3 MPa.

# Chapter 6

# Fracture Mechanics Testing

In this chapter, the test results are presented of the fracture mechanics tests as defined in Chapter 4. The test data as recorded by the test bench is given in Section 6.1, showing the force-displacement graphs and tables with failure loads and displacements. The results of the digital image correlation (DIC) analysis are given in Section 6.2. The crack growth and failure mechanics are discussed Section 6.3. The toughness of the material is determined in Section 6.4.

## 6.1 Test results

The fracture toughness tests are performed using center cracked tensile specimens (CC(T)s) specimens with 3 different widths and a variety of initial crack lengths, so that the sizing effects can be determined. In the following subsections, the force-displacement graphs of the small, medium and large scaled specimens are shown and evaluated.

### 6.1.1 Small scale fracture tests

The force-displacement graphs of the small-sized fracture test with a width of 120 mm samples are shown Figure 6-1. S01 is the reference un-notched sample. S02, S03 and S04 contain an initial crack of 40 mm, S05 and S06 30 mm and S07 and S08 50mm.

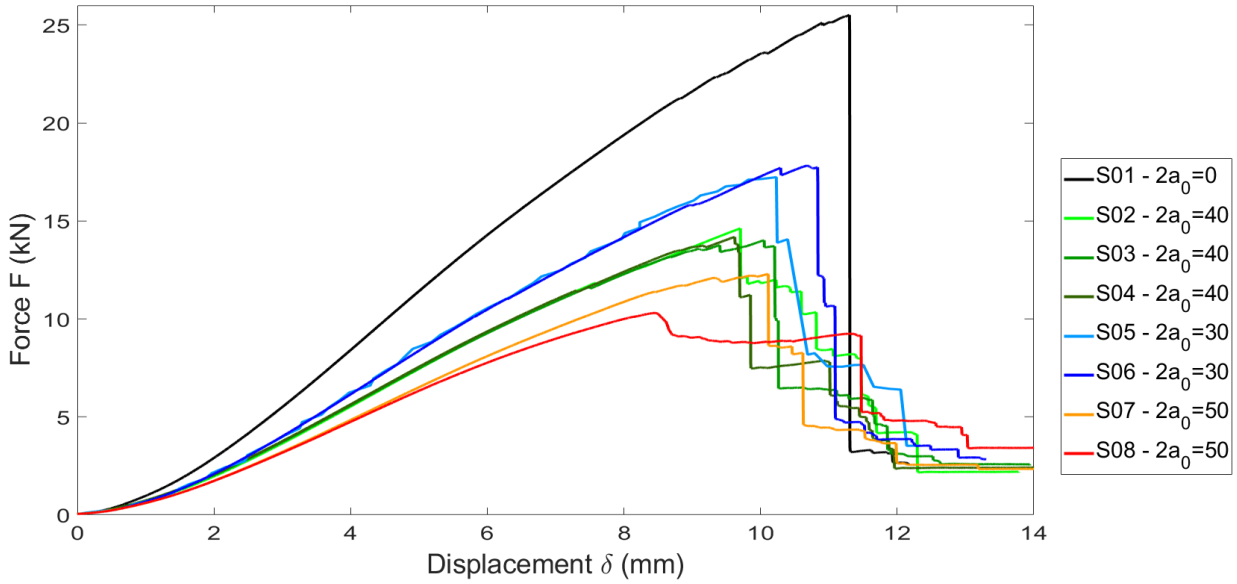


**Figure 6-1:** The force displacement graphs of the small sized fracture test samples. W=120 mm

The graph of sample S05 is the taken from the DIC output, since the data of this test was lost due to a crash in the bench software. The result is therefore less accurate since the sampling rate was 1

image per second. The result of sample S08 is invalid due to slip at the clamp, caused by a failure in the hydraulic clamps.

All specimens show a relative high residual stress after first failure, which are indicated by the horizontal sections between a displacement of 10 and 12 mm. This indicated that not all fibers fail at once. When the test is continued the force drops on intervals to a minimum force that does not reach zero. This residual force is carried by the Queo 8120 plastomer resin.

The failure loads and displacements are given in Table 6-1. The failure load is compared to the theoretical failure load, determined by the effective cross section as:

$$F_{th} = X^t \cdot (2W - 2a_0) \cdot t \tag{6-1}$$

With $X^t$ the failure stress, $W$ half the width, $a$ half the crack length and $t$ the thickness. In which only net-section stress is considered and any effects of stress concentration around the crack tip is not taken into account. The knockdown factor show the percentage at which the specimen failed with respect to the theoretical ultimate load. The last two rows show the displacement of the bench at failure, and the elongation of the test specimen with respect to the original length.

**Table 6-1:** Test results of the small scale fracture tests

| | | Specimen ID | | | | | | | |
|---|---|---|---|---|---|---|---|---|---|
| Parameter | Unit | S01 | S02 | S03 | S04 | S05 | S06 | S07 | S08 |
| Initial crack length | mm | 0 | 40 | 40 | 40 | 30 | 30 | 50 | 50 |
| Ratio $a/w$ | - | - | 1/3 | 1/3 | 1/3 | 1/4 | 1/4 | 0.42 | 0.42 |
| Theoretical failure load | kN | 28.18 | 18.78 | 18.78 | 18.78 | 21.13 | 21.13 | 16.43 | 16.43 |
| Failure load | kN | 25.51 | 14.62 | 14.01 | 14.18 | 17.73 | 17.82 | 12.29 | - |
| Knock down factor | % | 90.6 | 77.9 | 74.6 | 75.5 | 81.5 | 84.3 | 74.8 | - |
| Displacement at failure | mm | 11.3 | 9.7 | 10.05 | 9.6 | 10.2 | 10.6 | 10.1 | - |
| Elongation at failure | % | 6.3 | 5.4 | 5.6 | 5.3 | 5.7 | 5.9 | 5.6 | - |

All samples had a final failure well below the expected failure strength. The reference specimen, S01, has a strength of 90.6% of the theoretical failure load. This indicates that besides failure due to the limit of the material The notched specimens experienced a maximum failure strength between the 74.8% and 77.9%, with the exception of S05 and S06 which failed at 81.5% and 84.3%. In this case no effects of stress intensity are considered. The failure displacements have a variation of values between the 9.6 and 10.6 mm which corresponds to a failure elongation between the 5.4 and 5.9 %. These values are 28% up to 40% higher than expected from the value for ultimate strain of $\epsilon^t_{x_u} = 4.2\%$ as shown in Table 5-3.

### 6.1.2 Medium size fracture tests

For the medium sized samples with a width of 288 mm, 5 samples are tested, two un-notched, M01 and M02 and 3 notched M03, M04 and M05 all three with an initial crack length of $2a_0 = 96$ and a crack over width ratio of $2a_0/2W = 1/3$. The force-displacements graphs are given in Figure 6-2. The graph shows similar curves as with the small samples. Also here, stepwise force reduction is visible after first failure, indicating several events at which fibers break. Again, a residual strength remains present due to the high elongation properties of the resin.

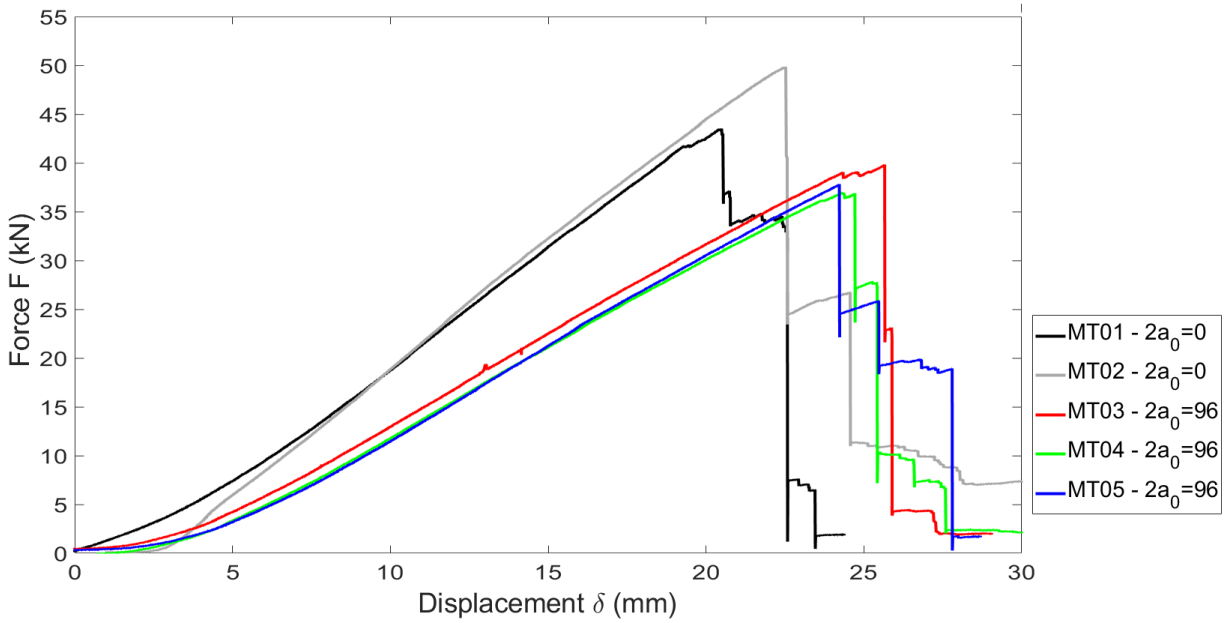


**Figure 6-2:** The force displacement graphs of the medium sized fracture test samples. W=288 mm

The forces at which first failure occurs and the corresponding displacements and stretches are given Table 6-2. The notched failure loads are between the 37 and 39.8 kN, which is the 82% and 88% of the theoretical failure load, which are determined using Eq. (6-1). These values are higher than those of the small sized fracture samples. Elongation at failure is between the 5.2 and 5.6% and similar to those if the small specimens.

**Table 6-2:** Test results of the midsize scale fracture tests

| | | Specimen ID | | | | |
|---|---|---|---|---|---|---|
| Parameter | Unit | M01 | M02 | M03 | M04 | M05 |
| Initial crack length | mm | 0 | 0 | 96 | 96 | 96 |
| Ratio $a/w$ | - | - | - | 1/3 | 1/3 | 1/3 |
| Theoretical failure load | kN | 67.62 | 67.62 | 45.1 | 45.1 | 45.1 |
| Failure load | kN | 43.5 | 49.9 | 39.8 | 37.0 | 37.8 |
| Knock down factor | % | 64.4 | 73.7 | 88.3 | 82.1 | 83.9 |
| Displacement at failure | mm | 20.49 | 22.5 | 25.6 | 24.3 | 24.1 |
| Elongation at failure | % | 4.7 | 5.2 | 5.9 | 5.6 | 5.6 |

Specimens M01 and M02 failed due to slip at the clamp as can be seen in Figure 6-3, a picture is taken after failure. This is caused which is caused by uneven loads in the reinforcement. The edge of the plate is marked with the black line. For an un-notched specimen, it is expected that the line remains straight, due to an expected equal stress distribution throughout the specimen. However, as can be seen in Figure 6-3a, where the two central bolts are present, the line hows a bulb. Due to the location of the bolts, the effective local fiber length within the clamp is reduced to 4 cm. This reduction is enough for the fabric to slip out of it's clamp due to lack of surface traction. The results of the un-notched specimens are therefore invalid. This effect does not occur at notched specimens as shown in Figure 6-3b, in this case sample M03 after failure. Due to different stress distribution around the crack-tip and throughout the rest of the sample, no slip is present at the clamp. The marked line follows in this case what is expected from the strain distribution as will be explained in Section 6.2.

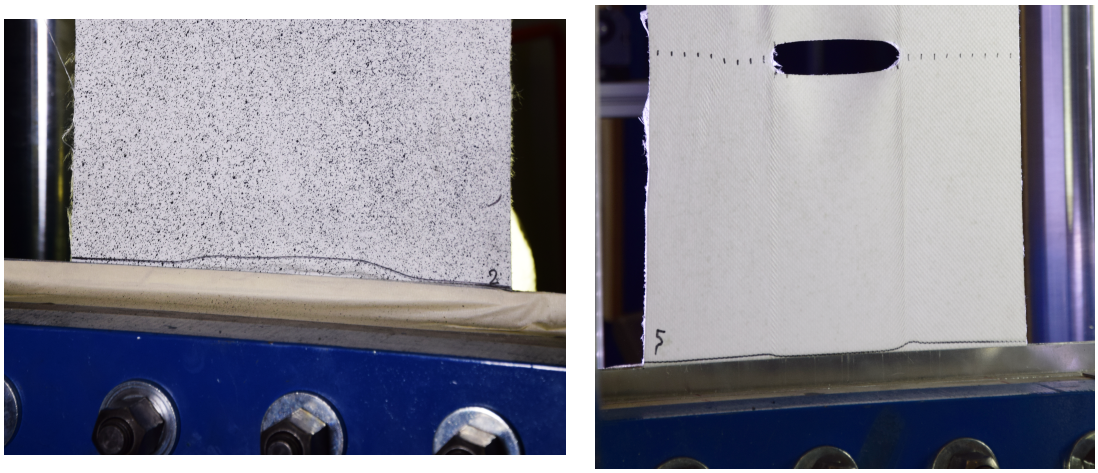

**(a)** Slip of the fabric in the clamp at the location of bolts.

**(b)** Negligible slip occurs when a notch is present

**Figure 6-3:** Failure due to slip within the clamp due to localization of holes for bolts

### 6.1.3 Large scale fracture tests

For the large size specimens, with a width of 900mm, 8 specimens are tested. L01 is the un-notched reference. L02, L03 and L04 contains an initial crack of $2a_0 = 300$ mm. L05, L06, L07 and L08 are used to determine the effect of the initial notch size, and contains initial cracks with lengths of respectively 200, 250, 350 and 400 mm.

The force-displacement graphs of all specimens are shown in Figure 6-4. The graphs show similar force-displacement graphs, but a large scatter of the displacement where first failure occurs. Again, stepwise failure is visible up to the point where all fibers have failed and the residual strength is carried by only the resin.

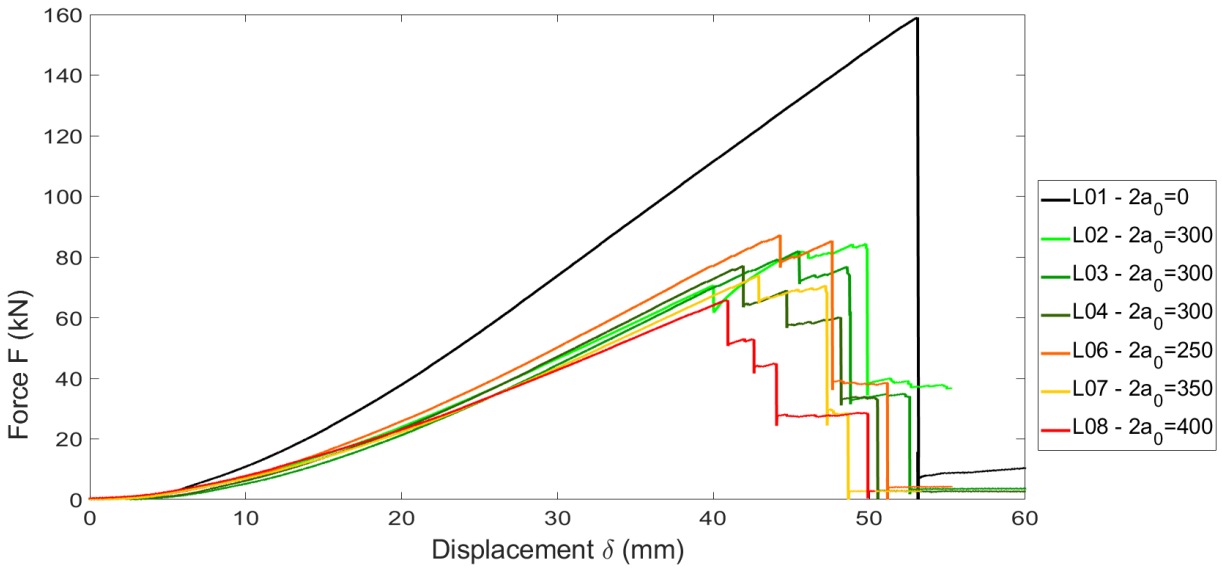


**Figure 6-4:** The force displacement graphs of the large sized fracture test samples. W=900 mm

When the failure loads are examined, the failure loads of the large test samples show a knock-down factor of values between the 55 and 60% with respect to the expected load. Which is 20% lower than the small and medium sized specimens. Also the displacements at failure, between the 40 and

**Table 6-3:** Test results of the large size fracture tests

| | | Specimen ID | | | | | | | |
|---|---|---|---|---|---|---|---|---|---|
| Parameter | Unit | L01 | L02 | L03 | L04 | L05 | L06 | L07 | L08 |
| Initial crack length $2a_0$ | mm | 0 | 300 | 300 | 300 | 200 | 250 | 350 | 400 |
| Ratio $a/w$ | - | - | 1/3 | 1/3 | 1/3 | 0.22 | 0.28 | 0.39 | 0.44 |
| Theoretical failure load | kN | 211.3 | 140.9 | 140.9 | 140.9 | 194.4 | 152.6 | 129.1 | 117.4 |
| Failure load | kN | 159.0 | 84.4 | 82.05 | 77.14 | 91.4 | 87.3 | 74 | 65.8 |
| Knock down factor | % | 75.3 | 59.9 | 58.24 | 54.7 | 55.6 | 57.19 | 57.13 | 56 |
| Displacement at failure | mm | 53.1 | 49.7 | 45.5 | 41.9 | 40.2 | 44.3 | 42.90 | 40.8 |
| Elongation at failure | % | 3.9 | 3.6 | 3.3 | 3.1 | 2.9 | 3.2 | 3.1 | 3.0 |

45 mm or as percentage of elongation between the 2.9% and 3.6% are much lower than those of the small and medium sized specimens. The larger knock-down factor indicates that effects due to the notch have a larger influence at wider specimens.

As like the un-notched sample M02, L01 failed due to slip at the clamp as can be seen in Figure 6-5a, The marked lines how that a bulb is being developed exactly at the location at one of the central bolts. This problems occurs only at un-notched specimens. Once a notch is present, as can be seen in Figure 6-5b where a picture is shown of sample L03 after failure, the effect of slip is not visible. Only the result of specimen L01 is therefore invalid.

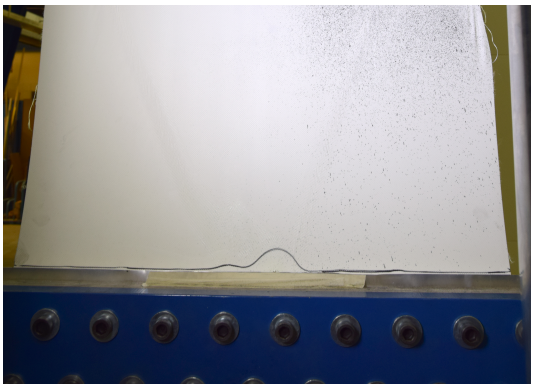

**(a)** Slip of the fabric at the location of bolts

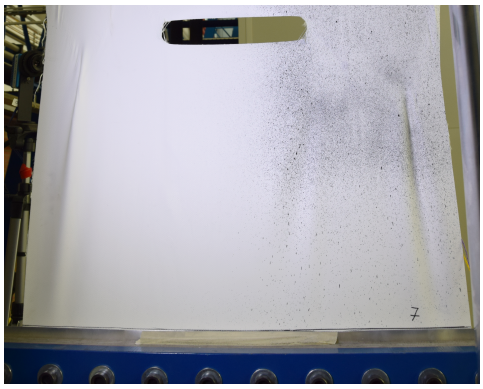

**(b)** Slip of the fabric at the location of bolts

**Figure 6-5:** Failure due to slip within the clamp due to local bolts

## 6.2 DIC analysis

Digital image correlation (DIC) is used to acquire full field strain and displacement data by measuring the relative displacements within the speckle field. In Table A-3 the settings of the DIC correlation are stated. In this section, the results of the correlation for 3 test samples are shown, S02, M03 and L02. This allows a comparison between the different sizes while maintaining the crack/width ratio equal to 1/3. For all other samples, the results of the DIC data are given in App. B.4. The strains and displacements shown, are taken in all cases from the last time-step before failure occurs. For each sample the tensile strain $\epsilon_y$, shear strain $\gamma_{xy}$ and displacement in y-direction $V$ are given, since those are the most relevant parameters for this research.

### 6.2.1 DIC analysis sample S02

Figure 6-6 shows the tensile strain $\epsilon_y$, shear strain $\gamma_{xy}$ and displacement in y-direction $V$ of specimen S02, which has an initial crack of $2a_0 = 40$ mm. The tensile strain $\epsilon_y$ is shown in Figure 6-6a, with a scale between -5 and + 5%. The image shows that the strain field can be divided roughly into 4 sections. Section A, is the area left of the crack, section B and C are the areas above and beneath the crack and section D the area right of the crack. When inspecting the strain field, it shows that the outer areas A and D, are under tensile strain, while the section above and beneath the crack, B and C, experience almost 0 strain. Stress intensities are visible around the crack-tips.

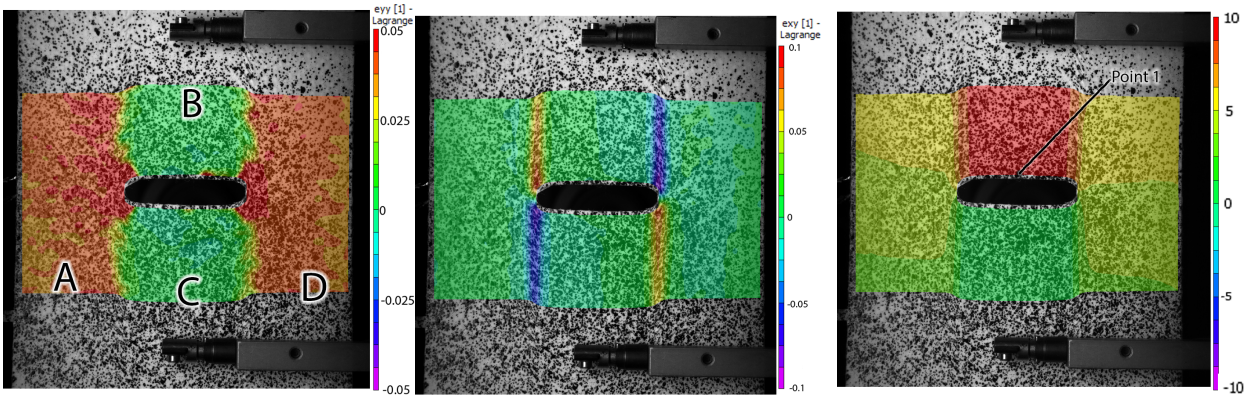


**(a)** Tensile strain in y-direction $\epsilon_y$ **(b)** Shear strain in y-direction $\epsilon_{xy}$ **(c)** Displacement y-direction $V$

**Figure 6-6:** DIC strain and displacement analysis of sample S02. Initial crack length is 40 mm. Images are captured just before failure.

Due to the low shear strength but high shear strain failure of the material, very high shear strains occurs in line of the crack-tips as can be seen in Figure 6-6b. The material is incapable of transferring loads between the outer and inner parts. As a result, the inner and outer areas can move relatively free with respect to each-other. It must also be noted that at the left and right edges, the strains are less than the average in sections A and D. This is a result of individual fibers slip at the clamp. Thus, clamping conditions affected the measured failure load of the specimens.

Figure 6-7a shows the longitudinal strain of the small scale test samples at the line $\theta = 0$, with the origin of the axis-system located at the crack-tip such that the axis are aligned as shown in Figure 2-5. The strain graphs show the singularity at the crack-tip, but after approximate 10 mm from the crack tip, the strain line is flat. The singularity, between $x = 0$ and $x = 5$ $mm$ is well over the limit strain of the fibers. It must therefore be noted that the strains as calculated visualizes the strain of the plastomer resin, which has a strain limit of 1000%. Fiber failure at the crack tip is not observed prior to failure.

In Figure 6-6c, the displacement $V$ in y-direction is plotted. The image shows a high displacement at section B above the crack and near zero displacement at section C. At sections A and D a gradient in the displacement is visible, which is expected since the boundary at the top side is where to displacement actuator is fixed.

When the displacement of Point 1, defined at the top edge of the edge in the middle of the plate, is plotted versus the displacement of the crosshead of the testbench, as shown in Figure 6-7b. It shows that the movement of section B is independent of the remaining of the ply. The displacements are almost equal in magnitude at failure, with less than 0.3 $mm$ difference.

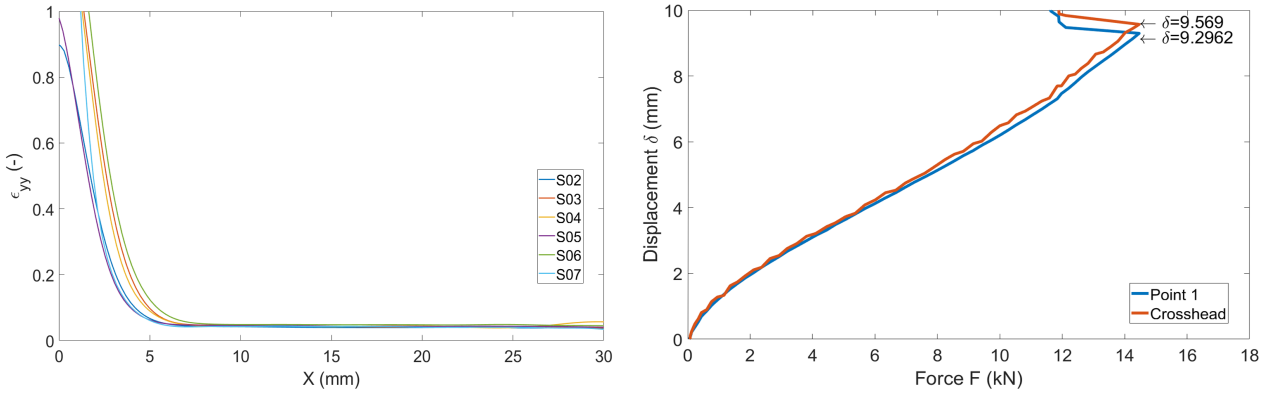


**(a)** Tensile strains $\epsilon_y$ at the line $\theta = 0,\ r = 0..30\ mm$ of the small sized test samples prior to failure.

**(b)** The displacement of Point 1 versus the displacement of the crosshead of the test bench

**Figure 6-7:** DIC strain in tensile direction ($\epsilon_y$) just before failure and the displacement analysis of sample S02 compared to the displacement of the bench crosshead.

### 6.2.2 DIC analysis sample M03

The DIC data generated from the medium size specimen M03 is shown in Figure 6-8 and is identical in behavior as the small scale samples. As can be seen in Figure 6-8a, no longitudinal strain $\epsilon_y$ is visible at the areas above and below the crack. All loads are carried at the outer sections and no load redistribution is present, leading to the high shear strain and deformation shown in Figure 6-8b and the displacements in y-direction in Figure 6-8c.

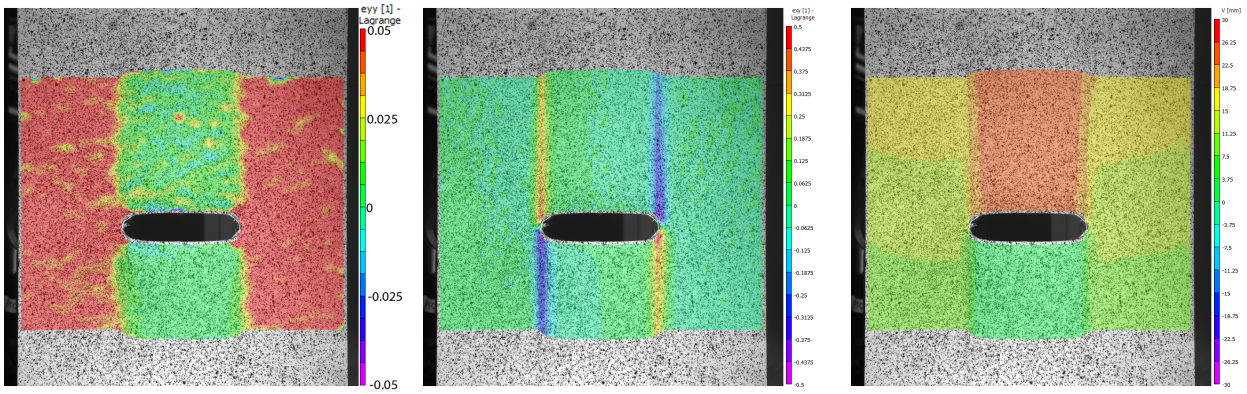

**(a)** Tensile strain in y-direction $\epsilon_y$

**(b)** Shear strain in y-direction $\gamma_{xy}$

**(c)** Displacement y-direction $V$

**Figure 6-8:** DIC strain and displacement analysis of sample M03. Initial crack length is 96 mm. Images are captured just before failure.

The longitudinal strains at the line $\theta = 0,\ r = 0..X$ are shown Figure 6-9. The same strain-curve as with the small scale test is visible. Most of the strain curve is consant up to 12 mm before the crack tip, at which the strain increases rapidly due to the strain in the elstomer resin.

### 6.2.3 DIC analysis sample L02

The results of the DIC analysis of sample L02 are shown in Figure 6-10. Due to the size of the specimens, only the right half of the specimens could be captured, such that the analysis retains a good resolution at the crack tip. The strain pattern is similar to sample S02. As shown in Figure 6-10a, the areas above and beneath the crack are strain free and all loads are carried by

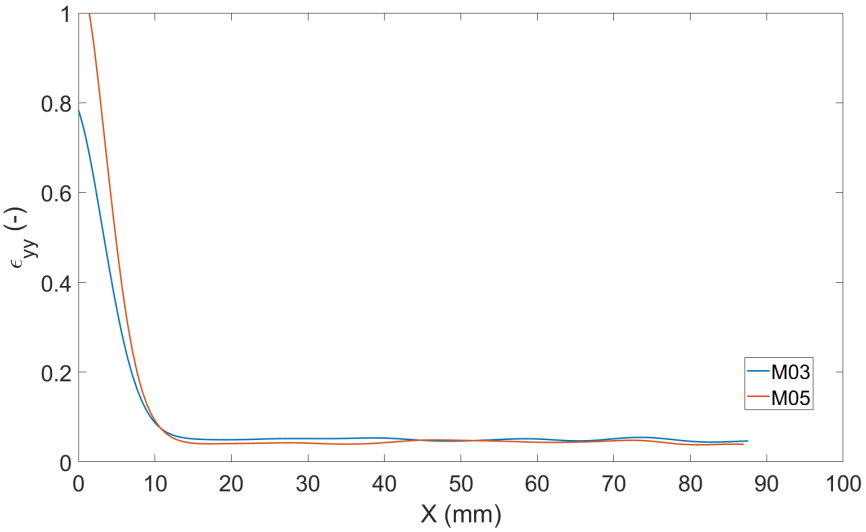


**Figure 6-9:** Longitudinal strain $\epsilon_y$ for samples M03 and M05 according to the DIC, on the line $\theta = 0$, $r = 0..X$

the intact area at the right side of the crack, with a concentration of strain around the crack tip. Again high shear strains bands are visible running from the crack in longitudinal direction.

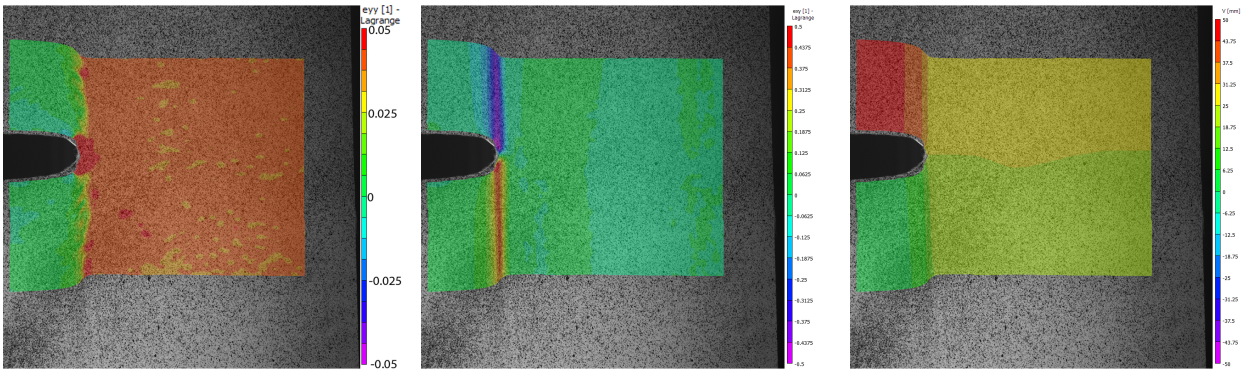


**(a)** Tensile strain in y-direction $\epsilon_y$ **(b)** Shear strain in y-direction $\gamma_{xy}$ **(c)** Displacement y-direction $V$

**Figure 6-10:** DIC strain and displacement analysis of sample L02. Initial crack length is 300 mm. Images are captured just before failure.

This behavior of strain and displacement is similar for all large sized specimens and the DIC images for each individual test can be found in App. B.4. The Longitudinal strain $\epsilon_y$ for samples L02 till L08, on the line $\theta = 0$, $r = 0..X$, are extracted from the DIC data and plotted in Figure 6-11. At the crack tip, singularities are developed and similar to the small and medium sized specimens, the strain graphs are flat from approximately 17 mm from the crack-tip.

## 6.3 Damage mechanism and evolution around the crack tip

### 6.3.1 Crack tip behavior

When the crack-growth behavior of the material is observed, several phenomena are discovered. Figure 6-12 shows the damage evolution of the crack of sample S02 at 4 different time-steps. Figure 6-12a shows the sample just after start where a crack is visible. In Figure 6-12b, the

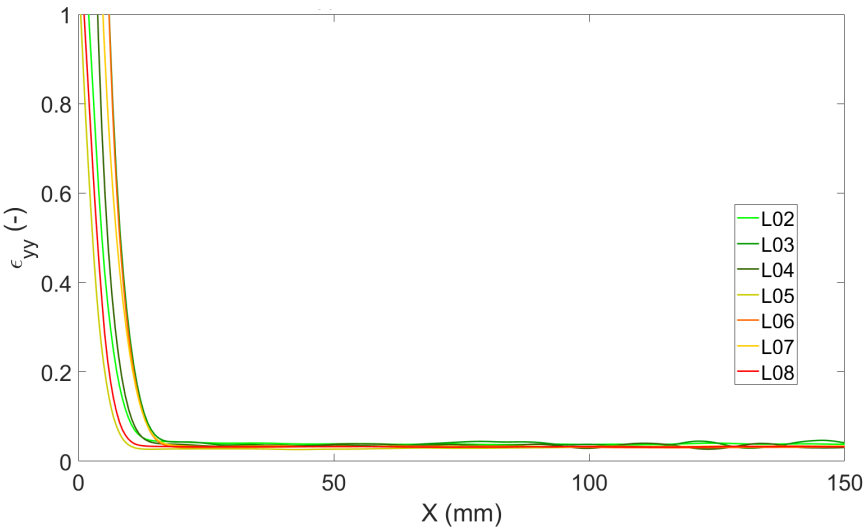


**Figure 6-11:** Longitudinal strain $\epsilon_y$ for samples L02 till L08 according to the DIC, on the line $\theta = 0$, $r = 0..X$

development of shear bands is becoming visible, running from the crack-tip vertically towards the clamps. It is visible that due to the plastic property and low shear strength of the resin, the crack is blunted. At Figure 6-12c fiber shifting at the crack tip occurs. The intensity of light at the crack tip, shows a reduction of material density due to the shifting of the transverse fibers. Fiber failure of the longitudinal fibers is not yet visible. The last figure, Figure 6-12d shows the sample just after first failure. The fibers are pull-out of the matrix resulting in the lighter areas at the crack-tips.

This crack tip behavior is similar with the larger test samples. Figure 6-13 shows the crack tip of sample L02. It shows a clear area at which fiber shifting occurred and the strain bands extending from it. Also visible in this picture is the pull-out of a weft fiber, due to the high displacement of the crack edges.

### 6.3.2 Fracture surface analysis using the scanning electron microscopy (SEM)

To get a further understanding of the damage propagation mechanics involved within the Dyneema® material, the fracture surfaces of several test specimens are investigated under the SEM.

Two images are shown in Figure 6-14. Both images show the bonding surface between the fibers and matrix of sample S03. Figure 6-14a shows the remaining fiber bundle in the 1-direction and the matrix material with the imprint of the fibers embedded in the lower half of the image. The image is magnified 110 times. The fibers show no remainings of the matrix material attached.. This shows that the matrix is released completely from the fibers under the given stress level.

The image in Figure 6-14b shows the fibers at the crack-tip taken in de 22-direction, magnified 30 times. The image shows the inner side of the matrix around the crack tip and the damaged fibers around that area. Although the fibers themselves are tangled and no fiber alignment is present anymore, again the fibers show no remainings of the adhesion with the matrix.

The most important conclusion drawn from those images is that no matrix material remains attached to the fibers after debonding of the fibers and matrix materials. This shows how weak the impregnation of the matrix with the fibers is.

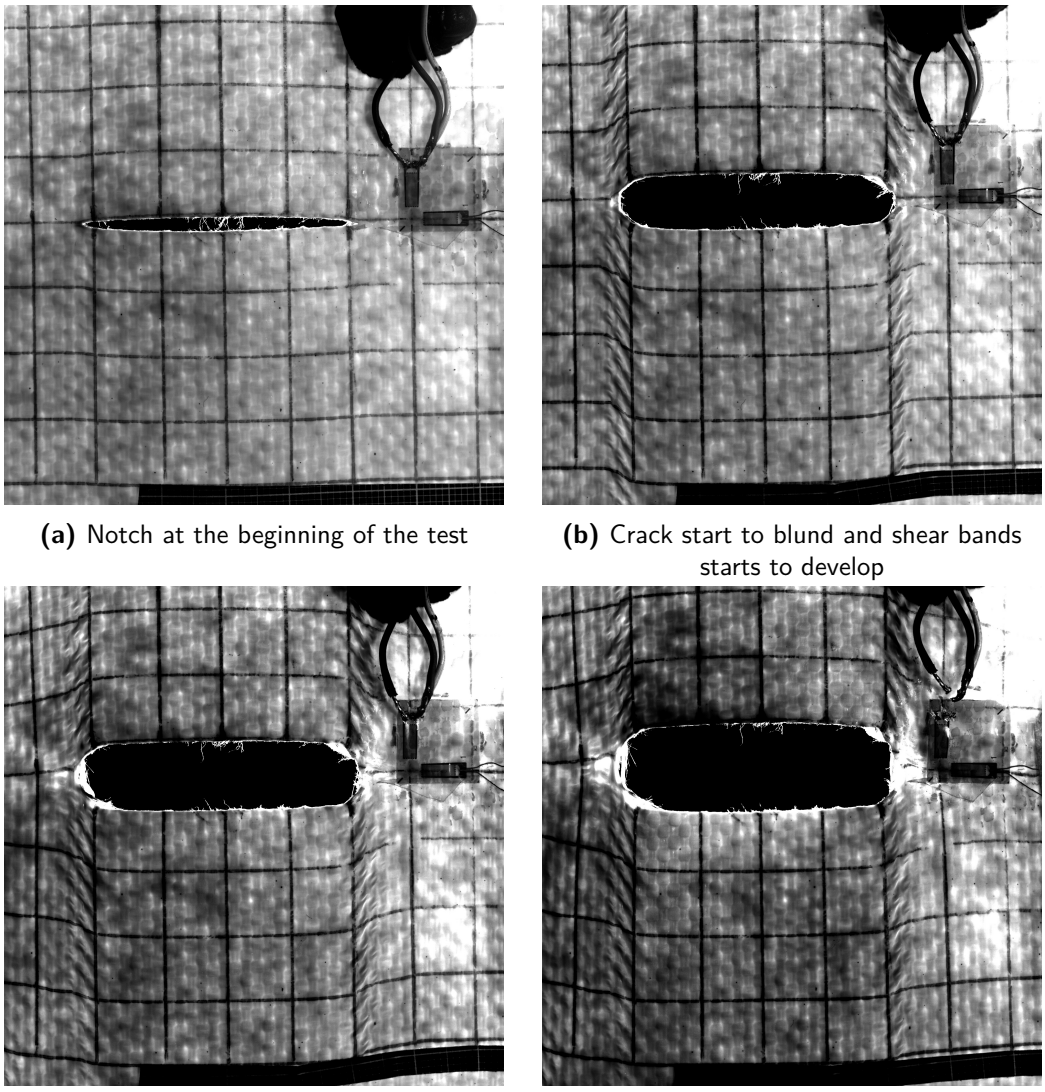

**(a)** Notch at the beginning of the test

**(b)** Crack start to blund and shear bands starts to develop

**(c)** Matrix debonding is visible at the left side of the crack, still no fiber failure is visible

**(d)** Just after failure, the fiber pull-out of both the longitudinal and transverse fibersfrom the matrix is clearly visible

**Figure 6-12:** Crack tip behavior of sample S02

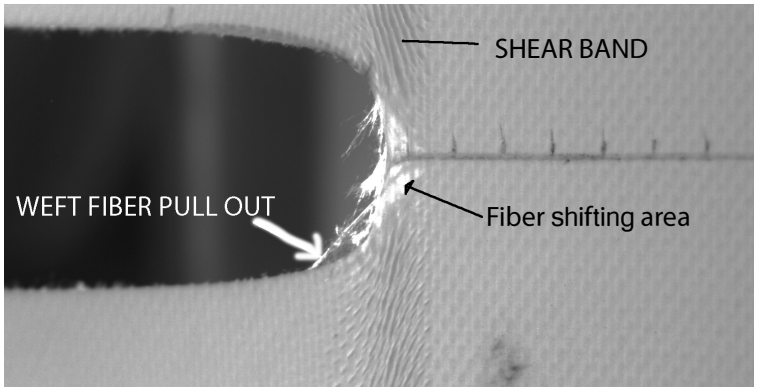


**Figure 6-13:** Crack tip behavior of the L02 sample just before failure.

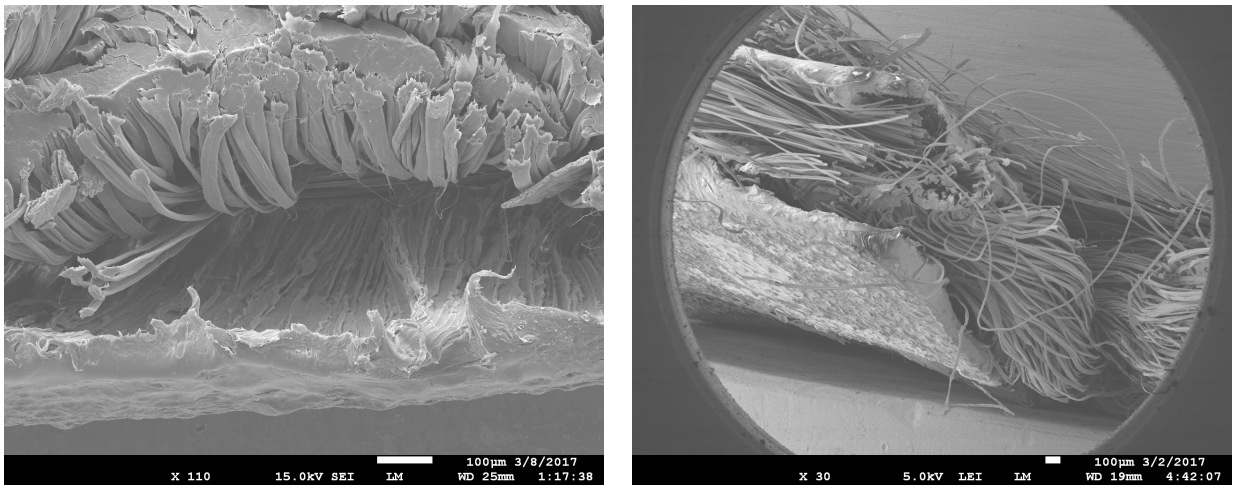


**(a)** Direction 11 **(b)** Direction 22

**Figure 6-14:** Crack surface of sample S03 investigated by the scanning electron microscope

## 6.4 Toughness

The test results showed a high crack opening before failure, with limited crack growth. The total energy absorbed by the lamina up to fracture can be defined as the Toughness. Essentially, the toughness $U$ is the total area underneath a force-displacement graph as function of unit length and area defined as:

$$U = \frac{1}{V}\int PdL = \int_0^L \frac{P}{A_0}\frac{dL}{L_0} \tag{6-2}$$

With P the applied force, $A_0$ the original cross-sectional area of the lamina, $dL$ the change in length under loading and $L_0$ its original length.

The values for $U$ are evaluated using the MatLab CUMTRAPZ command, which calculates the area underneath each force-displacement curve shown in Figure 6-1, Figure 6-2 and Figure 6-4.

As reference cross-section $A_0$, the crackline is removed from the cross-sectional area, such that the toughness is normalized for the actual cross-section.

The graphs resulting from the integration of the force-displacements curves are shown in Figure 6-15, in which the toughness curves of the small specimens(Figure 6-15a), medium specimens (Figure 6-15b) and large specimens (Figure 6-15c ) are plotted as function of the nominal strain, up to the moment of failure. The curves show a similar curvature up to the moment of failure at $F_u$. Since the curvatures are well aligned and show similar gradients,the values obtained for the toughness are mostly depended on the strain at failure. The maximum value obtained equals 9.45 $^{MJ}/_{m^3}$ for the un-notched specimen with a width of 120 mm. This is set as reference value to for comparison. The deviation of the curves grows with increasing specimen size.

The final graph, Figure 6-15d, compares each size an example at which $^{a_0}/_W = {}^1/_3$. It shows that the two small en medium specimens have failed at comparable strain and toughness. The toughness of the large specimen is much lower, due to the lower nominal failure strain and lower failure force.

The values of toughness corresponding with the graphs as shown in Figure 6-15 are given in Table 6-4. For each test, two values are calculated. The first corresponds with the strain at $F_{max}$. The second at final failure. The latter one is chosen to be calculated as well, due to the failure progress of the specimens. Not all fibers fail at once and a large residual strength is present after initial failure. This means that the lamina is capable of taking up more energy after failure.

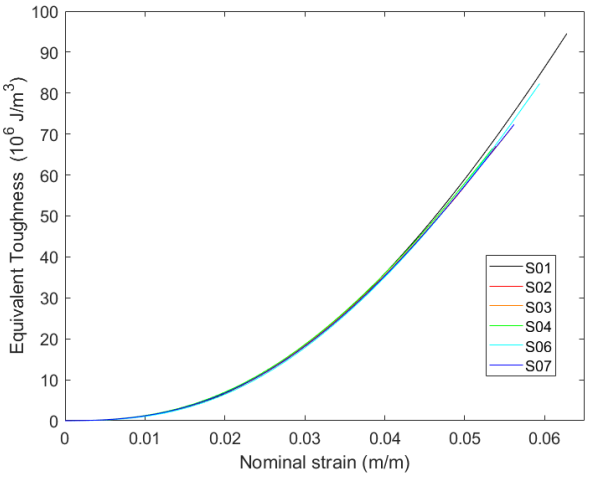


**(a)** Equivalent toughness of the small scale specimens as function of strain

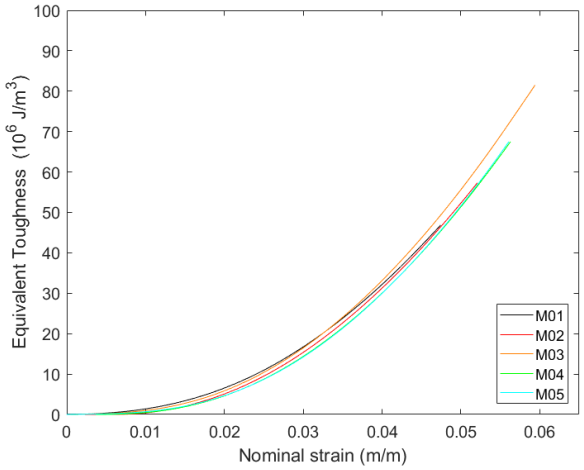


**(b)** Equivalent toughness of the medium scale specimens as function of strain

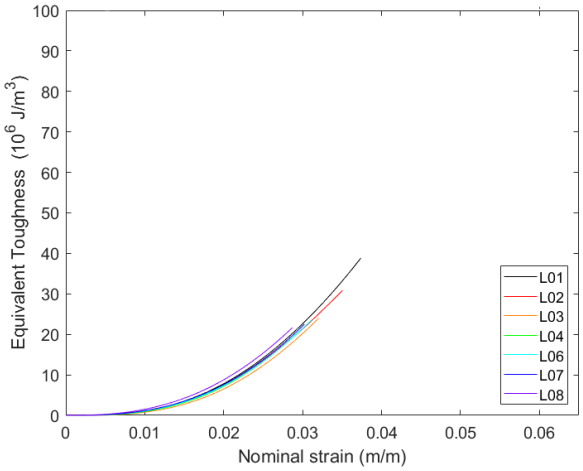


**(c)** Equivalent toughness of the large scale specimens as function of strain

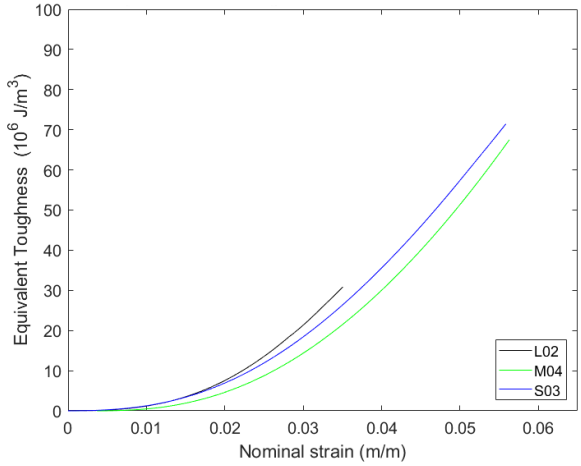


**(d)** Comparison of the 3 different sizes with an initial crack of $2a_0 = {}^1/_3 w$

**Figure 6-15:** Equivalent toughness graphs of the small, medium and large sized specimens

Examining the values in Table 6-4 gives the following results: All CCT test specimens show a decreased toughness value. For the small sized specimens, the toughness at $F_u$ lies between the 13 and 30% percent lower than the reference value. When the toughness at final failure is calculated, the results lie within 82% to 94% of the reference value. For the medium sized specimens, at $F_u$ the values reach 71% percent for sample M04 and M05 and 86% for sample M03. This is within the same margin as the small specimen. However, the difference of 15% between the M03 and M04/M05 at $F_u$ is large. At final failure, the toughness reaches a value between the 78 nd 88%. The largest increase is at specimen M05, with an increase of 14%. While M02 only increases 2%. This indicates that the amount of fibers that fail during the first failure event at $F_u$ is arbitrary. For the large scale specimens the values for toughness values are considerately lower and lie between the 22% and 25% of the reference value. At final failure the values reaches 30 till 36% of the reference toughness.

The calculations of the toughness values shows significant difference between the small and large specimens, while the medium specimens show similar results as the small specimens. Also, the fact that within same sized specimens quite a margin is present, shows that the failure properties are not due to fiber failure and sizing effects only. It is expected that larger specimens do show decreased

**Table 6-4:** Equivalent toughness values at Fmax and compete failure

| Sample | Width (mm) | Initial crack (mm) | Nominal Strain at Fmax (m/m) | Equivalent Toughness $MJ/M^3$ | Index | Nominal strain at complete failure (m/m) | Equivalent Toughness $MJ/M^3$ | Index |
|---|---|---|---|---|---|---|---|---|
| S01 | 120 | 0 | 0,063 | 9,45 | 100% | 0,063 | 9,45 | 100% |
| S02 | 120 | 30 | 0,059 | 8,23 | 87% | 0,062 | 8,76 | 93% |
| S03 | 120 | 40 | 0,054 | 6,70 | 71% | 0,068 | 8,85 | 94% |
| S04 | 120 | 40 | 0,056 | 7,15 | 76% | 0,070 | 8,55 | 90% |
| S06 | 120 | 40 | 0,053 | 6,65 | 70% | 0,061 | 7,78 | 82% |
| S07 | 120 | 50 | 0,056 | 7,23 | 76% | 0,067 | 8,36 | 88% |
| M03 | 288 | 96 | 0,059 | 8,15 | 86% | 0,057 | 8.34 | 88% |
| M04 | 288 | 96 | 0,056 | 6,75 | 71% | 0,059 | 7,33 | 78% |
| M05 | 288 | 96 | 0,056 | 6,75 | 71% | 0,064 | 8,04 | 85% |
| L02 | 900 | 250 | 0,031 | 2,36 | 25% | 0,036 | 2,99 | 32% |
| L03 | 900 | 300 | 0,035 | 3,09 | 33% | 0,039 | 3,44 | 36% |
| L04 | 900 | 300 | 0,032 | 2,40 | 25% | 0,037 | 3,02 | 32% |
| L05 | 900 | 300 | 0,030 | 2,07 | 22% | 0,036 | 2,84 | 30% |
| L06 | 900 | 350 | 0,030 | 2,25 | 24% | 0,034 | 2,86 | 30% |
| L07 | 900 | 400 | 0,029 | 2,17 | 23% | 0,035 | 2,81 | 30% |

toughness values. However, the fact that the large specimens show a toughness of only 30% percent indicates boundary conditions effects. Two mechanism involved may reduce the toughness values. First, the cloth is flexible. It is not unlikely that clamping the cloth using bolts puts an unequal pre-stress between the left and right sides of the cloth. Unequal pre-stress also explains why not all fibers fail at once. Secondly, the cloth requires a very high closing pressure in order to prevent slip from the clamps. For the small test specimens, tested using hydraulic clamps, the closing pressure equals 400 till 450 bar. Although each bolt at the MTS3500kN machine is pre-tensioned with a moment of 750Nm, the actual pressure on the cloth is theoretically just 216 bar at most, as shown in Section 4.3. This difference may be enough for the fibers to slip out of the matrix and clamp, leading to lower values for strain at failure and eventually the lower toughness of the material.

## 6.5 Conclusion

The fracture tests on the CC(T) specimens show quite a different result compared to fracture tests on metals and composite laminates. The membrane cannot reach the expected failure strengths based on the net-cross-sectional are and failure laws. Secondly, there is almost no stress transfer from the outer un-notched parts of the membrane, to the inner parts above and below the crack. As a result, unlike metals or CFRP laminates, there is no constant average stress far away from the crack.

The failure of the membrane consists of several modes, fiber failure, matrix debonding and fiber shifting. Initially a crack growth is visible due to fiber shifting at the crack tip and the fiber pull-put of the transverse fiber, due to the high shear stress perpendicular to the crack tip. The pull-out of transverse fibers is possible due to the weak bonding between the fibers and the matrix material.

The developed strains along the line $\theta = 0$ show a steep increase in strain at crack tip root, however further from the crack tip the strains are constant and no $1/\sqrt{\pi a}$ relation is present.

Toughness calculations on each specimens show a significant difference between the small and large specimen which is not a result of sizing effects only but also of the clamping conditions.

# Chapter 7

# Fracture Mechanics Analysis

The goal of this chapter is to investigate if the linear-elastic fracture mechanics (LEFM) method can by applied to determine the critical stress intensity factor of the cloth if this constant then can bu used determine the failure of the Dyneema® fabric analytically.

The analytical analysis for the determination of a critical stress intensity factor and the strain energy release rate in this chapter is based on the LEFM theory as described in Section 2.4. In this chapter, the anylysis is performed by comparing the analytical stress equations with the stresses obtained by the digital image correlation (DIC) analysis in Section 6.2.

First, in Section 7.1, the stress intensity factor required to determine the stress around the crack tip, will be extracted determined using the failure load and effective crack size. The stress field will be determined in Section 7.2, using the anisotropic stress equation from Lekhnitskii et al.[12]. Followed by the conclusion in Section 7.3

## 7.1 Determination of the critical stress intensity factor

As reviewed in Section 2.4.5, the stress intensity factor for a center cracked tensile specimen (CC(T)) specimen under Mode I loading is given by Lei et al.[22] as:

$$\mathcal{K}_{I_c} = \frac{P\sqrt{\pi a}}{2tW} F\left(a/W\right) \tag{7-1}$$

with $F(a/W)$ defined by Fedderson as:

$$F\left(a/W\right) = \sqrt{\sec\frac{\pi a}{2W}}\left[1 - 0.025\left(a/W\right)^2 + 0.06\left(a/W\right)^4\right] \tag{7-2}$$

For all test specimens, the geometry factor is calculated and given in Table B-2. However, to determine the analytical stress field, the geometry factor must by calculated according to the actual crack size, $a_{eff}$. The length of the crack can be measured from the images captured by the DIC or Optomotive camera system, by using a video analysis and modeling tool called Tracker[48]. This program calculates the length between two points by using a defined reference scale. This reference scale is a grid tape that is placed onto the test specimen as can be seen at the bottom of Figure 7-1. The applied force at moment the image is capture equals $P = 14.6$ kN.

The effective crack length is measured as $2a_0 = 43.01$ mm. Substituting the value into Eq. (7-2) with $2W = 120$ mm gives a geometry correction factor of $F\left(a/W\right) = 1.085$ This value can now be substituted into the stress intensity equation given Eq. (7-1) together with the values for P, t, W and $a_{eff}$. The calculated stress intensity factor (SIF) is:

$$\mathcal{K}_I = 47.8 \text{ MPa}\sqrt{m}$$

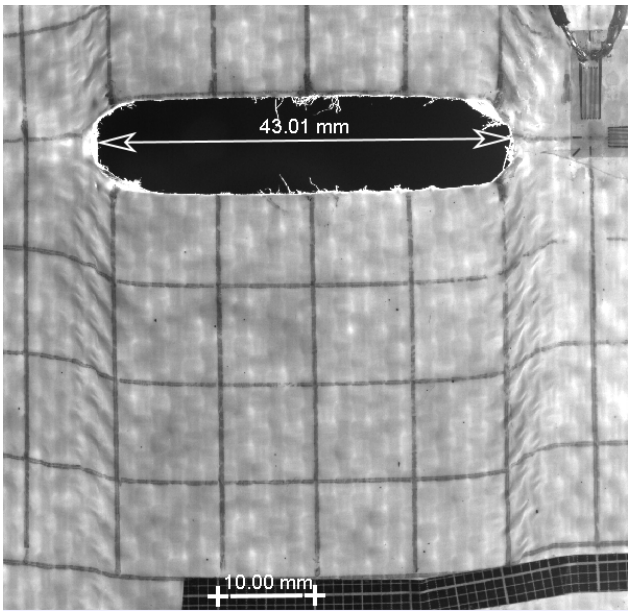


**Figure 7-1:** Effective crack length of the Specimen S02 just before failure with a current loading of P = 14.6 kN, measured with tracker software[48]

## 7.2 Anisotropic stress curve

The stress in y-direction across the line $\theta = 0, r > 0$ is determined by applying the anisotropic stress and displacement equations from Lekhnitskii et al.[12]. The complete set of equations to calculate the 3 stress components and the two displacements are given in Section B.1.

For $\sigma_y$ the equation is derived as:

$$\sigma_y = \frac{\mathcal{K}_I}{\sqrt{2\pi r}} Re\left[\frac{1}{\mu_x - \mu_y}\left(\frac{\mu_x}{\sqrt{\cos\theta + \mu_y \sin\theta}} - \frac{\mu_y}{\sqrt{\cos\theta + \mu_y \sin\theta}}\right)\right] \tag{7-3}$$

The roots $\mu_1, \mu_2$ are obtained by solving the 4th order polynomial equation of Eq. (2-25) and obtained using matlab. The method for solving the polynomials given in App. B.3.1. The results are 4 imaginary numbers:

$$\mu_{x_{1,2}} = 0.00 \pm 2.2240i \tag{7-4}$$

$$\mu_{y_{3,4}} = 0.00 \pm 0.0537i \tag{7-5}$$

By substituting the roots into Eq. (7-3), the theoretical stress in y-direction, $\sigma_y$, at the vicinity of the crack tip can be calculated and compared to the stresses obtained from the DIC measurements. For this, the stress $\sigma_y$ along the line $\theta = 0, r = 0..w$ is calculated using Eq. (7-3) and plotted in Figure 7-2 versus the stress obtained by the DIC system. In addition, the line at ultimate tensile stress in warp direction $X^t$ is shown as reference.

The analytical line shows a clear $1/\sqrt{\pi r}$ curve, which has a small but increasing inclination towards the crack tip, followed by a smooth transition into a infinite stress at the crack tip. The overall stress is well below the maximum tensile stress of the material. Only at the crack tip, where it is expected for the stress to go infinite, the stress grows above the ultimate stress limit. In reality, this stress is relieved by plasticity.

If the analytical graph is compared to the actual stresses measured by the DIC system, we see that in reality the stress along the line $\theta = 0$ remains flat, up to the vicinity of the crack tip, where it

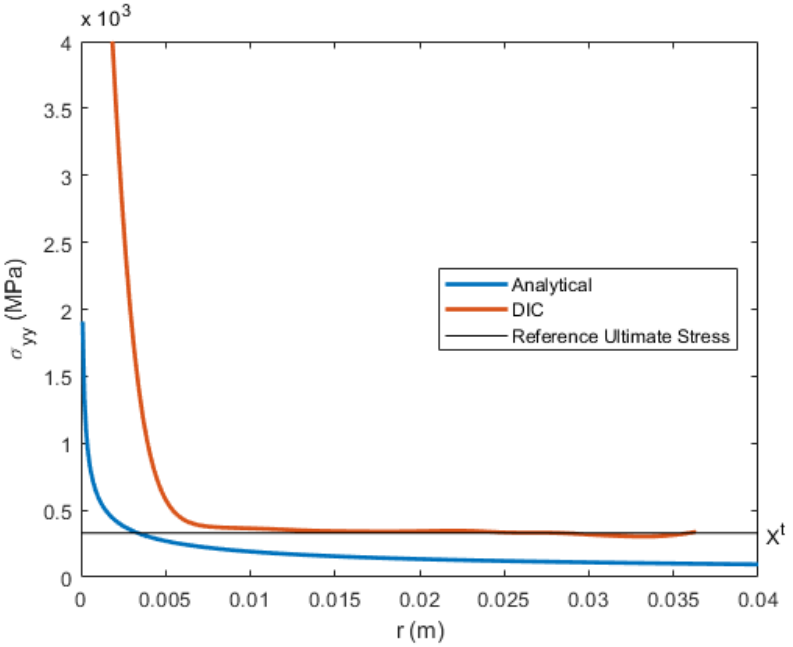


**Figure 7-2:** The stress in y-direction ($\sigma_y$) along the line $\theta = 0, r = 0..0.4$ fro the small sample S02

again goes to infinite. It must be noted that the strains measured by the DIC are the strains of the plastomer matrix. It is not possible for the DIC system to measure the actual stresses in the longitudinal fibers. And due to the fiber shifting behavior of the plain weave at the crack tip, the matrix is strained more then the fibers themselves, leading to the 'infinite' strains at the crack tip.

The nominal stress level equals the ultimate stress $X^t$ for $r > 12$ mm. This is a significant difference with the analytical curve, which follows the $1/\sqrt{\pi r}$ curvature well below the ultimate stress. As explained in Chapter 2, failure of materials can occur in two ways, yield-dominant or fracture-dominant. The correlation between the longitudinal stress obtained from the DIC and the ultimate tensile stress show that the lamina fails at the moment the overall stress reaches the ultimate tensile stress. Although the test results in Chapter 6 show a reduction in the expected failure loads, meaning that the crack or clamping conditions has an effect on the load bearing capability of the cloth and some stress intensity effect is present, the main failure mode of the cloth is not fracture but strength dominant. This invalids the use of the LEFM method as a predictive tool based on the critical stress intensity and strain energy release rate. Although theoretically it is possible to determine the values, there is no correlation between the theory and the actual behavior of the fabric. A second reason why the LEFM theory is invalid, is found in the assumptions on the theory is based on. First, to determine the nominal stress, the LEFM theory assumes that far away from the crack, the stress is nominal distributed over the cross-sectional area of the fabric. In case of the Dyneema fabric, this stress redistribution is not present due to the low shear strength of the matrix material and no ±45 degree layers are present to actively relief the stress around the crack. Secondly, the LEFM stress field equations derived by Westergaard[16] neglect higher order terms, making them valid for small crack opening displacements and values of $r$ only. In case of the Dyneema® fabric the crack opening displacements is almost as large as the nominal strain of the material.This can not be considered as a small opening displacement and therefore this assumption the Westergaard stress equations are based upon, is invalid.

The large sample shows similar results. Following the same procedure as for the small specimen. The the stress in y-direction is plotted against the analytical stress curve and the actual stress from the DIC can be plotted as shown Figure 7-3. In this case, crack length $2a_0 = 302.3$ mm and the failure load 84.4 kN. The theoretical critical stress intensity factor $\mathcal{K}_{I_c} = 97.5\ {}^{MPa}/\sqrt{m}$.

The resulting curves in Figure 7-3 show the same behavior as with small specimen. The stresses obtained by the DIC show a constant line, with a peak stress at the crack tip. The constant line overlaps the ultimate stress failure $X^t$ of 330 MPa.

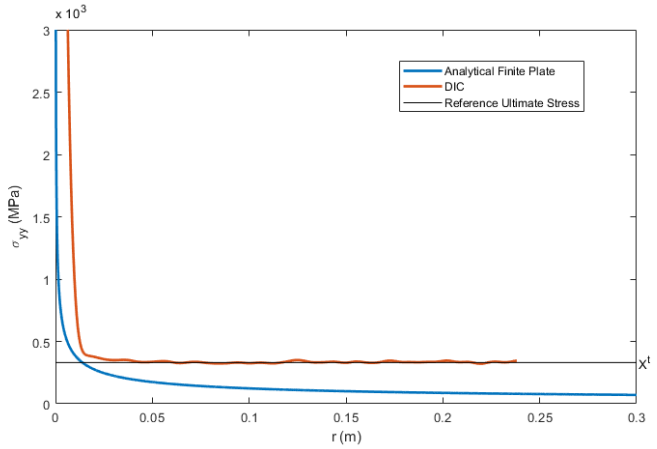


**Figure 7-3:** The stress in y-direction ($\sigma_y$) along the line $\theta = 0, r > 0$ for the large sample L02.

## 7.3 Conclusion

Comparing the results from the fracture mechanics tests with the stress and displacement equations shows that the LEFM is not a valid solution for the fracture toughness problem of the Dyneema® cloth since the failure mode is not fracture-dominant and the assumptions used to develop the LEFM theory do not hold when applied on the fabric. As a result, the stress ahead of the crack tip shows no $1/\sqrt{\pi a}$ curvature but a flat line with a peak at the crack tip due to the elasticity of the plastomer matrix. Failure occurs when the cross-sectional areas reaches the ultimate tensile stress of the material. Since the failure mode is not fracture dominant, it is not possible to determine a critical stress intensity factor $K_{I_c}$ or a critical strain energy release rate $G_{I_c}$ as fracture toughness properties of the Dyneema® cloth.

# Chapter 8

# Peridynamic Simulation

Now that the LEFM based analytical solution proofed invalid for the Dyneema® cloth and can not be used as a predictive tool, the next step is to investigate if a numerical solution is capable of determining the fracture response of the fabric. This chapter contains the results of the fracture toughness simulations using the peridynamic theory, to investigate if this method can be used to determine allowable damage in the tsunami barrier. In the first section, Section 8.1 the peridynamic material constants for the Dyneema® fabric are determined. Followed by the validation in Section 8.2. The validation is based on Hooke's Law for linear stress-strain equations, without failure to determine the optimal grid spacing $\Delta x$. In Section 8.3 the peridynamics (PD) method is used to simulate the fracture toughness problem in correspondence with the fracture toughness tests as presented in Chapter 6. Followed by the conclusion in Section 8.4

## 8.1 Material properties and discretization

Within a peridynamic simulation, the material properties for an UD lamina are defined by two variables, the bond constant in fiber direction $c_f$ and in all other directions $c_m$[36]. The values are determined by Eq. (2-39) and Eq. (2-40), which are a reduced form of the equations in Eq. (8-1a) and Eq. (8-1c) based on the assumption that $\mathcal{Q}_{12} = \mathcal{Q}_{66}$ and $\mathcal{Q}_{22} = 3\mathcal{Q}_{12}$[36]. Under these assumptions the transverse bond-force constant $c_t$ vanishes completely from the model.

$$c_f = \frac{(\mathcal{Q}_{11} - \mathcal{Q}_{12} - 2\mathcal{Q}_{66})}{2\delta \left( \sum_{j=1}^{N} \left| \mathbf{x}_j^n - \mathbf{x}_i^n \right| \mathcal{V}_j^n \right)} \tag{8-1a}$$

$$c_t = \frac{(\mathcal{Q}_{22} - \mathcal{Q}_{12} - 2\mathcal{Q}_{66})}{2\delta \left( \sum_{j=1}^{M} \left| \mathbf{x}_j^m - \mathbf{x}_i^m \right| \mathcal{V}_j^m \right)} \tag{8-1b}$$

$$c_m = \frac{24\mathcal{Q}_{66}}{\pi t \delta^3} \tag{8-1c}$$

In case of the plain weave Dyneema® fabric however, the transverse fiber constant $c_t$ is required to model the properties transverse fibers and their failure. If the entries of the stiffness matrix in Eq. (5-1) are examined, it can be shown that the assumptions that $\mathcal{Q}_{12} = \mathcal{Q}_{66}$ and $\mathcal{Q}_{22} = 3\mathcal{Q}_{12}$ do not hold for this material and therefore $c_t$ does not automatically vanishes. Therefore, the material parameters are determined by the full equations as stated in Eq. (8-1).

That $c_t$ does not vanish has a direct influence on other parts in de model, such as the surface correction factors. The details and the mathematics concerning these factors are in reviewed in Appendix C.

A further implication is the difference in mechanical properties of the fibers between the longitudinal and transverse directions. As shown in Figure 5-1b, the Young's modulus shows non-linear behavior, which is especially large transverse directions, due to the stretching of the fibers. For the longitudinal direction, the effect is relative small and therefore ignored in this model. The transverse Young's Modulus can be seen as bi-linear with a change in stiffness at approximate

$\epsilon_{trans} = 8\%$ strain. This led to the definition of two stiffness matrices $\mathcal{Q}$ , with different entries due to the change in calculated stiffness and corresponding Poisson's ratios. This change in stiffness has to be implemented in the PD code. Based on the two different $\mathcal{Q}$ -matrices, two transverse bond-constants can be determined, $c_{t_1}$,$c_{t_2}$. And an additional law is required that determines the correct bond-force constant based on the actual stretch between two material properties. Although the actual transition is non-linear, in this research the material will be modeled as a bi-linear material with its transition at $\epsilon_{trans} = 0.08$.

$$c_t = \begin{cases} c_{t_1} & \text{for} \quad sc_{22} < \epsilon_{trans} \\ c_{t_2} & \text{for} \quad sc_{22} \geq \epsilon_{trans} \end{cases} \tag{8-2}$$

### Failure properties

Within PD, failure is introduced into the simulation by defining a critical stretch for each individual force-bond vector, based on the directional properties of the Dyneema® fabric. The set of equations to determine the critical stretch values where given in Section 2.5.3 Eq. (2-43). By substituting the Young's moduli and failure stresses from Table 5-2 and Table 5-3 the critical stretches are calculated as:

$$\begin{cases} s_0^{ftl} = \frac{\mathbf{X}^t}{E_{11}} = 0.038 \\ s_0^{fcl} = \frac{\mathbf{X}^c}{E_{11}} = 1 \\ s_0^{ftt} = \frac{\mathbf{Y}^t}{E_{22}} = 0.040 \\ s_0^{fct} = \frac{\mathbf{Y}^c}{E_{22}} = 1 \\ s_0^{mt} = \frac{\mathbf{S}^t}{G_{12}} = 0.45 \\ s_0^{mc} = \frac{\mathbf{S}^c}{G_{12}} = 1 \end{cases} \tag{8-3}$$

The compressive failure stress is very low for the Dyneema® fabric and the failure mode is micro buckling. In the simulations, the compressive failure is ignored and therefore set to 1, meaning that within the calculation failure can not occur under compression. It is not expected that the induced transverse compressive stress is of any influence in determining the tensile failure in longitudinal direction.

### Correction for nonlinear behavior

A drawback in using this linear failure model, is that the non-linear behavior at the beginning of the stress-strain curves are not included, effectively reducing the values for $s_0$ compared to the failure strains in Table 5-3. Especially in the 22-direction, where first 8% strain is developed before the fibers start carrying loads, the failure stretch is only a 1/3rd of the actual failure strain.

The differences are given in Table 8-1. For the failure in direction 11, the difference is 44%. The biggest difference is the critical stretch in the transverse direction, which is increased by 217%. The matrix failure stretch become 20% smaller.

**Table 8-1:** Difference in calculated failure stretch and test strain

| Parameter | Calculated critical stretch | Failure strain from test | Difference |
|---|---|---|---|
| $s_0^{ftl}$ | 0.038 | 0.055 | 44 % |
| $s_0^{ftt}$ | 0.041 | 0.13 | 217 % |
| $s_0^{mt}$ | 0.45 | 0.36 | -20 % |

The failure parameters are therefore corrected in the code to suit the actual failure strains from the coupon tests.

### Bond-Forces after fiber failure

The second alteration to the failure properties, is that the test results showed that once the fibers fail, the matrix material keeps up taking load. This is added in the simulation by defining an post fiber fail region. Doing so, each force-stretch function, will consist of several parts defined as:

$$c_f = \begin{cases} c_f + c_m & \text{for} \quad sc_{11} < s_0^{ftl} \\ c_m & \text{for} \quad s_0^{ftl} \geq sc_{11} < s_0^{mt} \\ 0 & \text{for} \quad sc_{11} \geq s_0^{mt} \end{cases} \tag{8-4a}$$

$$c_t = \begin{cases} c_{t_1} + c_m & \text{for} \quad sc_{22} < \epsilon_{trans} \\ c_{t_2} + c_m & \text{for} \quad \epsilon_{trans} < sc_{22} < s_0^{ftl} \\ c_m & \text{for} \quad s_0^{ftl} < sc_{22} < s_0^{mt} \\ 0 & \text{for} \quad sc_{22} > s_0^{mt} \end{cases} \tag{8-4b}$$

$$c_{ft} = \begin{cases} c_m & \text{for} \quad sc_{12} < s_0^{mt} \\ 0 & \text{for} \quad sc_{12} \geq s_0^{mt} \end{cases} \tag{8-4c}$$

Schematically, the graphs of the bond forces as function of the stretch are as shown in Figure 8-1.

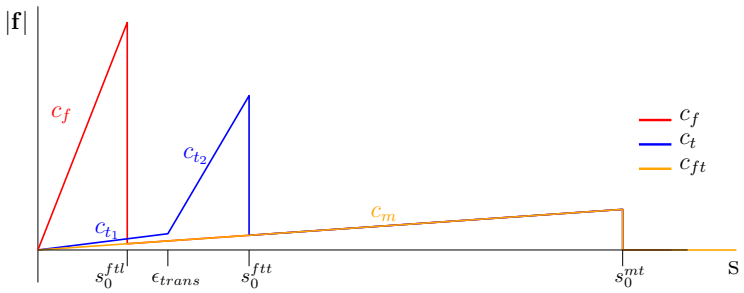


**Figure 8-1:** Material bond-force graphs

With these bond-force functions, the change in stiffness as function of strain is accounted for, as is the behavior of the material after initial failure. These are considered as the most important parameters. Several other effects seen during testing can not be included.

First, the tests show severe fiber-shift and fiber pull-out from the matrix at the vicinity of the crack tips. Since this model is based on the macroscopic failure properties, the microscopic effect are not defined. Especially since only 1 layer of material points will be defined in the z-direction, the forces in longitudinal, transverse and arbitrary directions act on the same material point. This means that the fibers, in reality running op and over each other, cannot shift with respect to each other since no such mechanism is included. It is possible within the PD framework to model fibers individually with contact algorithms, see for example Silling et al.[49], but in this research the macroscopic failure is examined, and therefore modeling on that micro-scale is out of scope. This holds for the failure mode concerning matrix debonding as well. No shifting between fibers and matrix at the same location is possible.

In reality, these effects cause a reduction in stress levels, since materials tend to deform such that

the energy within the material is minimum. Since that is not possible within this model, it might be expected that failure occurs at lower strains.

## 8.2 Validation

The peridynamic simulation is verified using the un-notched test specimen case with dimension of 120 by 180 mm. The purpose of the validation is to determine the optimal grid spacing $\Delta x$ and the number of required time steps to reach convergence.

During the validation, the displacements of the material points on the x and y axis are determined and compared with the displacements of an analytical solution, based on Hooke's Law as described in Section 2.3.1 and a net stress applied in the longitudinal direction. The results of the validation will not be compared with the results from the tests in Chapter 5, since the boundary conditions applied are significantly different.

### 8.2.1 Analytical displacement

The analytical displacements for validation are determined by applying Hooke's law under a net stress of $\sigma_{11} = 163.4$MPa

The strain in x and y direction under an unidirectional strain is determined by applying Hooke's Law in compliance form as given in Eq. (2-6). Since the applied stress in direction 22 is zero, the stress-strain equation can be reduced to:

$$\begin{cases} \epsilon_{11} = & S_{11} \cdot \sigma_{11} \\ \epsilon_{22} = & S_{12} \cdot \sigma_{11} \\ \tau_{12} = & 0 \end{cases} \tag{8-5}$$

With $S_{11} = \frac{1}{E_{11}}$ and $S_{12} = -\frac{\nu_{21}}{E_{11}}$. Once the strains are known, the elongation of the fabric at location (x,y) can than be determined by the following set of equations:

$$\begin{cases} u_x(x, y = 0) = & \frac{\sigma_{11}}{E_{11}} y, & \text{for} -0.9 < x < 0.9 \\ u_y(x = 0, y) = & -\nu_{12} \frac{\sigma_{11}}{E_{11}} x, & \text{for} -0.6 < y < 0.6 \end{cases} \tag{8-6}$$

### 8.2.2 Discretization

For the validation, several runs are performed with increasing number of material point. The peridyamic material parameters are depended on $\Delta x$. The first two columns in Table 8-2 show the number of material points in x- and y-direction $(nX, nY)$. Followed by the total number of material points and grid spacing $\Delta x$. The number of material points in x-direction are increased from 90 tot 240 points, allowing the displacements to be measured and compared for a wide range. The last 4 columns shows the peridynamic material constants in the longitudinal ($c_f$) and transverse ($c_{t_1}$,$c_{t_2}$) and all other directions.

### 8.2.3 Boundary conditions and time step

The boundary condition is set to an arbitrary applied stress of $\sigma_1 = 163.4$MPa. This stress is divided over the material points in the boundary region as an incremental force which is calculated by Eq. (4-5). The number of time steps is set to 10000 with the time step size set to $dt = 1$.

**Table 8-2:** Parameters of the peridynamic simulation which are depended on the grid size.

| Number of divisions | | Total number of | $\Delta x$ | $c_f$ | $c_{t_1}$ | $c_{t_2}$ | $c_{ft}$ |
|---|---|---|---|---|---|---|---|
| nX | nY | Material points | mm | - | - | - | - |
| 60 | 40 | 2400 | 3 | 7.53e+19 | 5.03e+17 | 3.16e+19 | 1.80e+17 |
| 90 | 60 | 5400 | 2 | 2.54e+20 | 1.70e+18 | 1.06e+20 | 6.09e+17 |
| 120 | 80 | 9600 | 1.5 | 6.02e+20 | 4.03e+18 | 2.52e+20 | 1.44e+18 |
| 150 | 100 | 15000 | 1.2 | 1.18e+21 | 7.87e+18 | 4.93e+20 | 2.82e+18 |
| 180 | 120 | 21600 | 1 | 2.03e+21 | 1.36e+19 | 8.52e+20 | 4.87e+18 |
| 210 | 150 | 29400 | 0.86 | 3.23e+21 | 2.16e+19 | 1.35e+21 | 7.73e+18 |
| 240 | 180 | 38400 | 0.75 | 4.82e+21 | 3.22e+19 | 2.02e+21 | 1.15e+19 |

The simulations are run on a 64 bit, Windows 10 computer, with 24 GB of memory. Further details of the hardware are given in Table 8-3

**Table 8-3:** Properties of the hardware used to perform the calcualtions

| | |
|---|---|
| Operating system | Windows 10 Education, 64x |
| Processor | Intel® Core™i7-7600HQ CPU @ 2.60Ghz |
| Memory | 24 GB DDR4 |
| Graphics card | Nvidia Quadro M1000M with 4GB GDDR5 memory |
| Program | MatLab® R2017b 64x |

### 8.2.4 Validation Results

For each run, the displacements of the nodes along the x-and axis are measured and plotted against the analytical displacements determined by Eq. (8-6). The resulting graph is shown in Figure 8-2. The lines representing displacement U in x-direction show good correlation between the peridynamic calculation and the analytical displacement for all $\Delta X$. The error between the displacement is given in Table 8-4 and stays within a 1% margin, and decreases with increasing number of nodes. For nX=240, the error is just 0.08%. The biggest error is caused by the bulb visible at the edges of the lamina.

**Table 8-4:** Parameters of the peridynamic validation

| Nx | Displacement U (mm) | Error U % | Computational time (s) |
|---|---|---|---|
| 60 | -1.662 | 99.09 | 186,57 |
| 90 | -1,678 | 99.46 | 437,15 |
| 120 | -1,686 | 99.65 | 725,10 |
| 150 | -1,690 | 99.76 | 1121,28 |
| 180 | -1,693 | 99.83 | 1638,82 |
| 210 | -1,696 | 99.89 | 2407,28 |
| 240 | -1,697 | 99.92 | 3361,55 |

The last column in Table 8-4 shows the computational time for the calculation. It is clear that the larger the number of material points, the more time the computation requires. For $nX = 60$, with a total of 2400 material points, the computation took just above 3 minutes. While for the

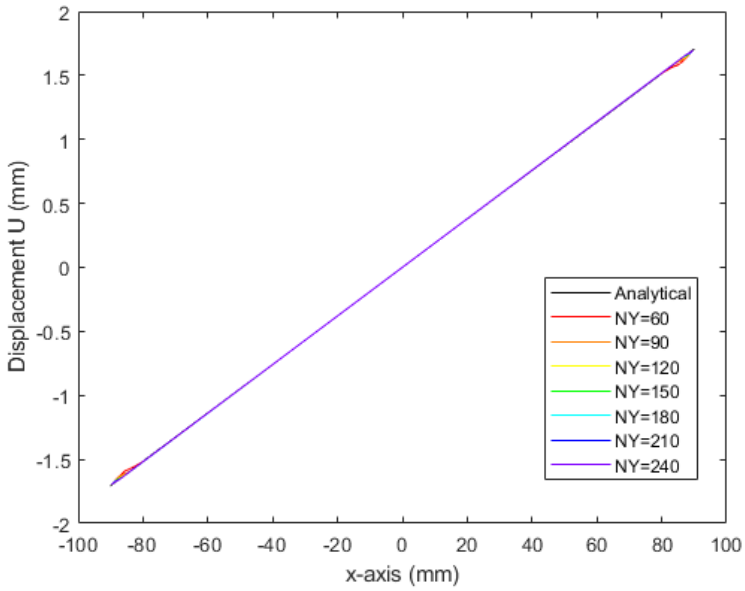


**Figure 8-2:** Displacements along the x-axis of the peridynamic simulation compared to the analytical solution

last computation, for $nX = 240$ with a total of 38400 material points, the computation required almost an hour.

The required time steps to reach convergence is examined for the grids with $nX = 60, 150, 240$. For this, the displacements of the material point located at the top right corner is plotted over time in Figure 8-3. The figure shows 6 graphs. The 3 on the top are the displacement in x-direction. In all 3 cases, the displacement converges within 2000 time steps.

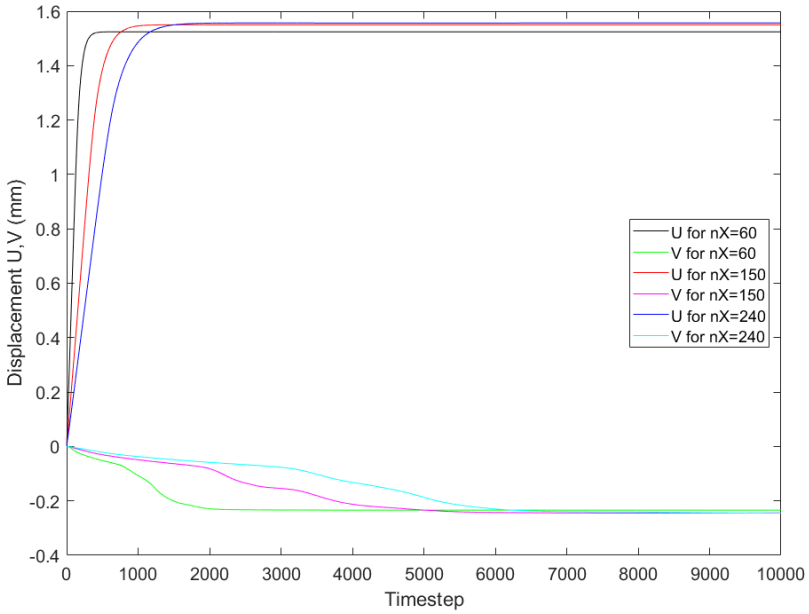


**Figure 8-3:** Displacements (u,v) of node with original coordinates $(x, y) = (70.2, 40.2)$ plotted against the timestep

The displacement $v$ in y-direction requires more time steps to reach converges. Since the displacement in y-direction is a pure reaction on the loading in x-direction, and the transverse bond force constant is initially weak, it takes more timesteps for the material point to accelerate. Again, the

fastest convergence is reached for nX=60 with 2500 timesteps. For nX = 150, 6000 time steps are required and for nX = 240, at least 7000 timesteps. The model requires thus more than triple the amount of timesteps to reach convergence in y-direction, compared to the x-direction.

Based on the results of the validation and the given errors, the grid spacing for the first fracture simulation will be set to $nX = 150$ as a good balance between the error and the computational time required.

## 8.3 Fracture simulations

In this section, the fracture simulation is performed on the specimen of width by height = 120x180 mm with an initial crack of 40 mm. The model is discretized in the same way as at the validation model. Velocity boundary conditions applied, a no fail zone of $3\Delta x$ width is placed at the boundaries of the lamina. Furthermore, failure is introduced by applying the material failure parameters given in Eq. (8-4).

### 8.3.1 Discretization, boundary conditions and the initial crack

The initial crack is modeled by deleting the force bond constants running through the crack line as shown in Figure 4-9. When the damage parameter is introduced into the model, the crackline becomes visible. The result of the discretization process is shown in Figure 8-4. In the figure, no fail zones at the left and right boundary are marked red. The inner part shows the local damage at each material point, as defined by Eq. (2-44). Values run between 0 meaning no damage at the material point, to 1 meaning all bonds at the material point are broken. Practically a value of 0.5 means a failed material particle.

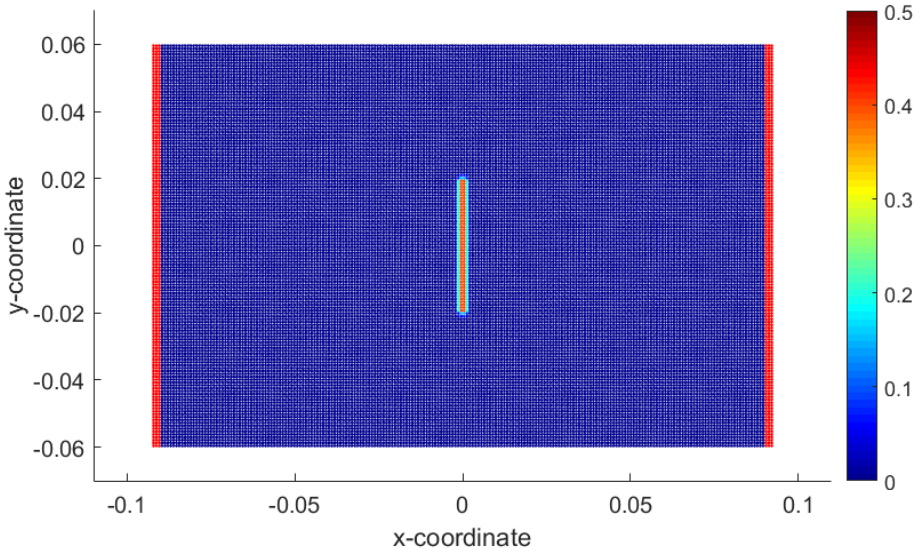


**Figure 8-4:** Discretization of the lamina with 150 nodes in x-direction. The outer boundaries are no-fail zones and marked red. The initial crack is shown according to the damage parameter

#### Boundary conditions and time step

#### Critical time step

The critical time step size is derived by Oterkus et al.[36] as:

$$\Delta t_{crit} = 0.8 \cdot \sqrt{\frac{2\rho}{\pi \delta^2 c_f}} \tag{8-7}$$

### Boundary condition

Due to the weak shear strength of the material, it is not possible to apply force boundary conditions. Since that will cause the center of the fabric simply to be pulled out at very low forces. This effect is shown in Figure 8-5. The left image, Figure 8-5a shows, the displacements when the force is 1000 N. A large crack opening is already present but no indication of crack growth or any other types of failure. If the force is increased 500 N, the crack completely zipped open as shown in Figure 8-5b. At the fracture toughness test, the actual failure load was 14 kN so only 10% of the failure load is reached, meaning this approach is invalid.

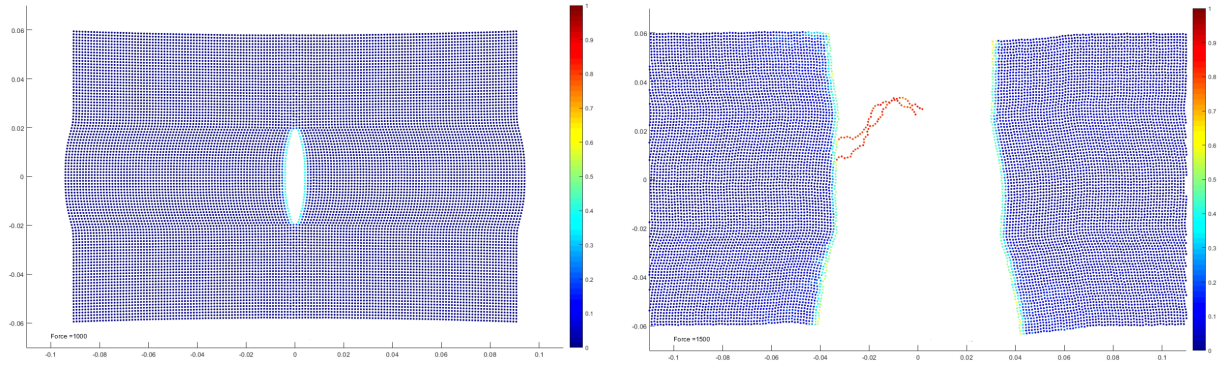

**(a)** F = 1000 N **(b)** F=1500 N

**Figure 8-5:** Fracture of the model when a force boundary condition is applied while a crack is present at a very low applied force due to pull out of the center sections of the lamina.

Therefore, only a velocity boundary condition can be applied. The thickness of te boundary layer is 3 material points. The speed set is 2 $^{mm}/_{sec}$ in x-direction. For the boundary regions, the displacement in transverse direction is constraint. In this way the boundary conditions are equal to the boundary conditions of the tests in Chapter 6 and is defined as:

$$\begin{cases} \dot{u}_{bnd_x} & = \pm 2^{mm}/_{sec} \\ \dot{u}_{bnd_y} & = 0 \end{cases} \tag{8-8}$$

## 8.3.2 No crack reference sample

The first fracture simulation is performed on a un-notched specimen with a width of w = 120 mm to determine if the failure is initiated at the correct strain. The parameters for the simulation are given in Table 8-5. As failure strain in longitudinal direction, the nominal failure strains of the small notched test samples is taken.

**Table 8-5:** Parameters for the un-notched fracture simulation

| Parameter | Value | Parameter | Value |
|---|---|---|---|
| nX | 150 | $s_0^{ftl}$ | 0.055 |
| nY | 100 | $s_0^{ftt}$ | 0.13 |
| dt (s) | $1.5 \cdot 10^{-07}$ | $s_0^{mt}$ | 0.45 |

The fracture behavior is shown in Figure 8-6. The left figure, Figure 8-6a shows the damage at timestep 16190, at which the lamina experiences a nominal strain of 5.48%. Figure 8-6b shows the lamina when completely failed at a nominal strain of 5,5%

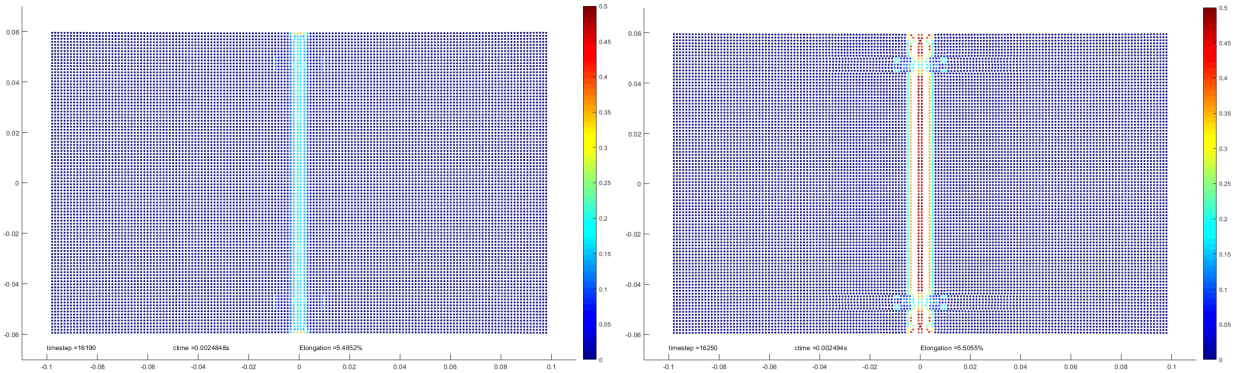

**(a)** Initiation of damage at time-step 16190, and a nominal strain of 5.48%

**(b)** Complete failure of the lamina at timestep 14250 and a nominal strain of 5,5%

**Figure 8-6:** Fracture of the un-notched reference sample at a nominal strain of 5.5%

Failure of the material points starts become visible once the nominal strain, with a value of 5.4% is just below the defined stretch limit in longitudinal direction $s_0^{ftl}$ which has a value of 0.055. The model therefore shows good agreement with the failure strain of the material.

### 8.3.3 Fracture toughness simulation

Next step is the damage progression of the notched specimen. Again, the dimensions pf the lamina are 120 by 180 mm and the initial crack length is 40 mm. Failure parameters are given in Table 8-5. Figure 8-7 shows the damage development within the lamina over time. The left images show the damage parameter. The right images the displacement in longitudinal direction $U$. Figure 8-7a is the start position in which the crack line is already visible. If the crack growth and damage is examined, it can be seen that up to a time step of 6000, the crack opens but does not grow. Also small shear bands start to develop at the crack tip, similar to what has been seen at the tests in Chapter 6.

If the crack grows, the damage in the lamina increases at the outer regions, but in the center regions no damage is visible. Also, the shear bands increase in thickness, and propagate wavelike through the material. No damage growth is visible in the center regions of the lamina.

The crack growth during the simulation is plotted in Figure 8-8a and the crack opening at the x-axis in Figure 8-8b. The crack growth graph shows that once the critical stretch is reached at the crack tip at timestep 6200, the opening of the crack equals 5 mm. Far below the test value of 9 mm.

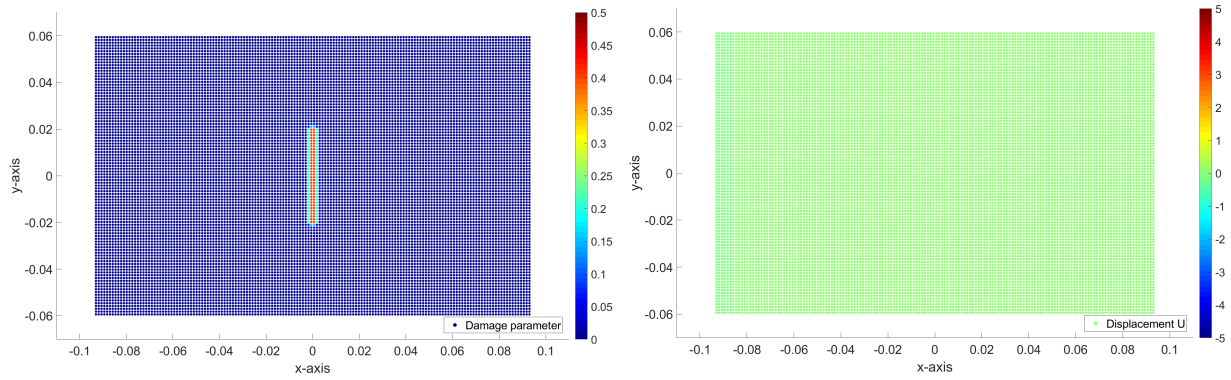


**(a)** Damage parameter, Timestep 1

**(b)** Displacement U, Timestep 1000

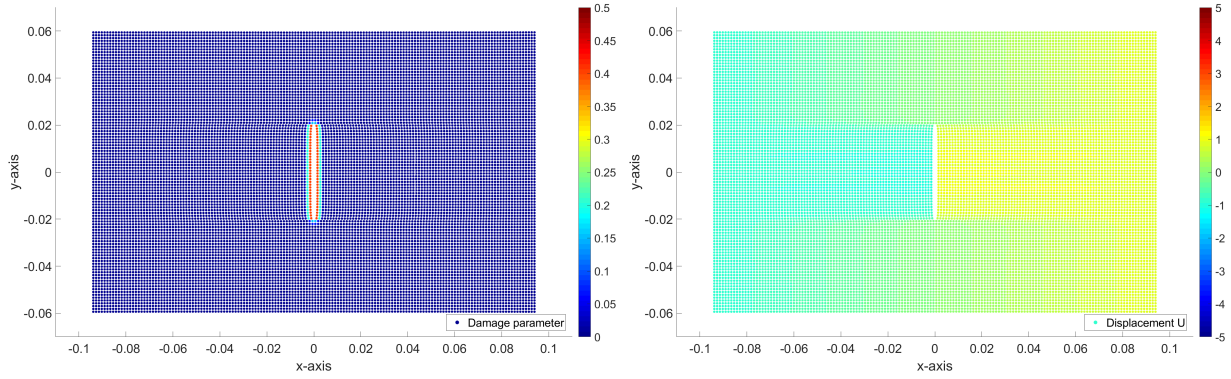


**(c)** Damage parameter, Timestep 3000

**(d)** Displacement U, Timestep 3000

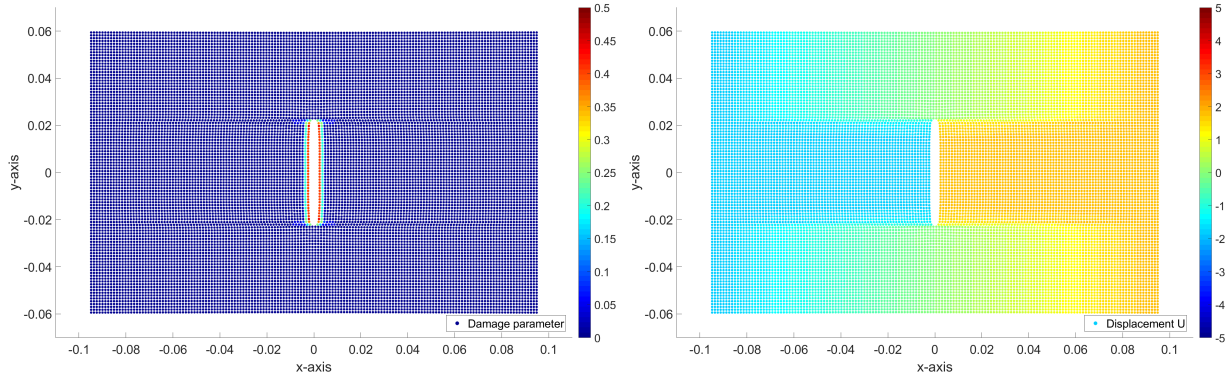


**(e)** Damage parameter, Timestep 6000

**(f)** Displacement U, Timestep 6000

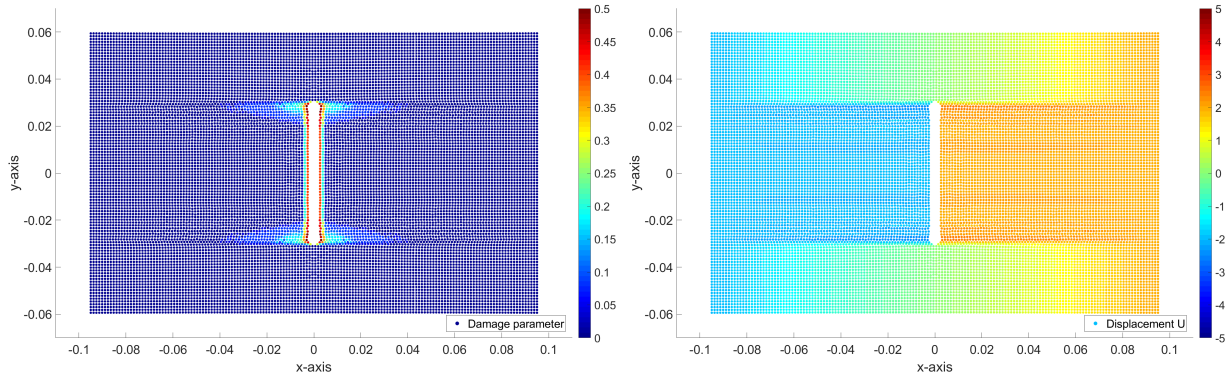


**(g)** Damage parameter, Timestep 6500

**(h)** Displacement U, Timestep 6500

**Figure 8-7:** Displacement in x-direction, damage initiation and crack growth sequence at increasing time steps

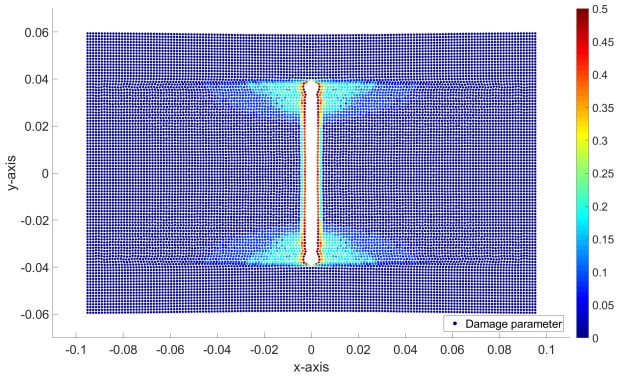


**(i)** Damage parameter, Timestep 7000

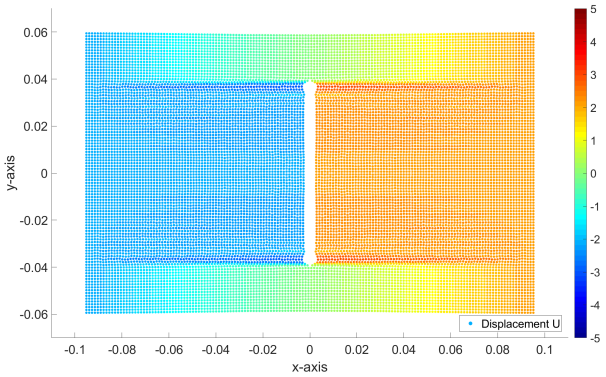


**(j)** Displacement U, Timestep 7000

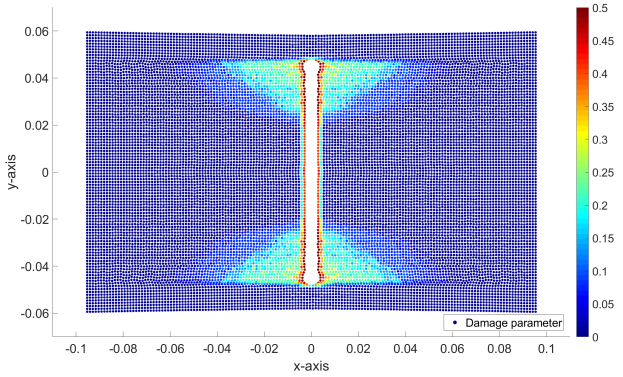


**(k)** Damage parameter, Timestep 7500

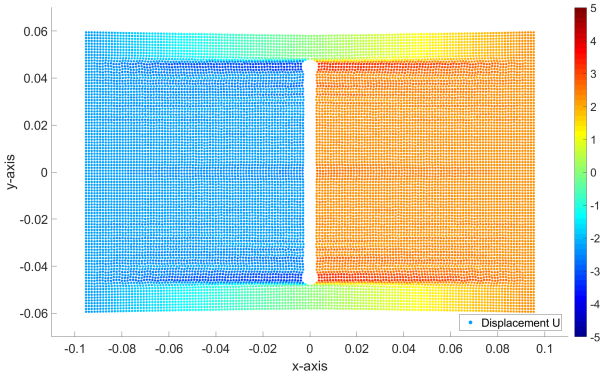


**(l)** Displacement U, Timestep 7500

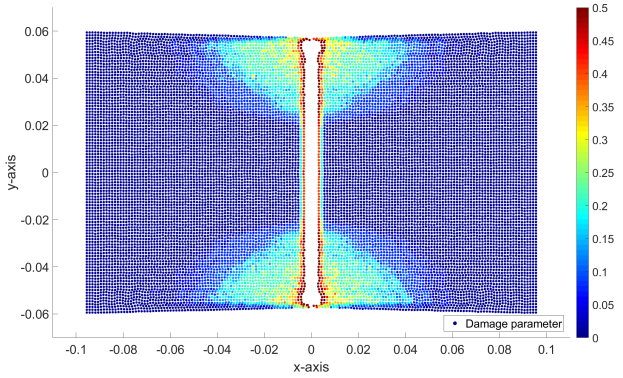


**(m)** Damage parameter, Timestep 8000

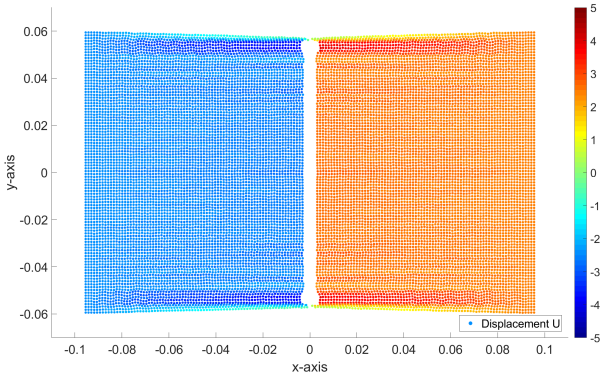


**(n)** Displacement U, Timestep 8000

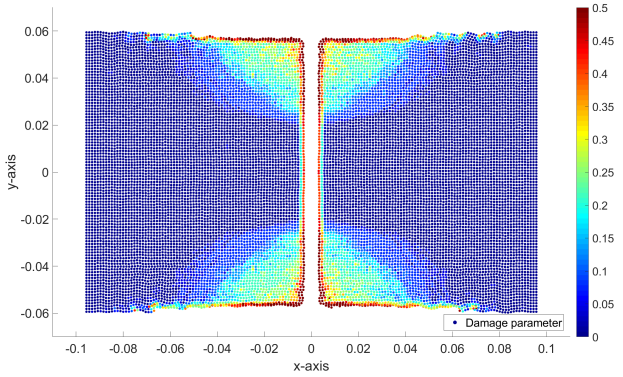


**(o)** Damage parameter, Timestep 8500

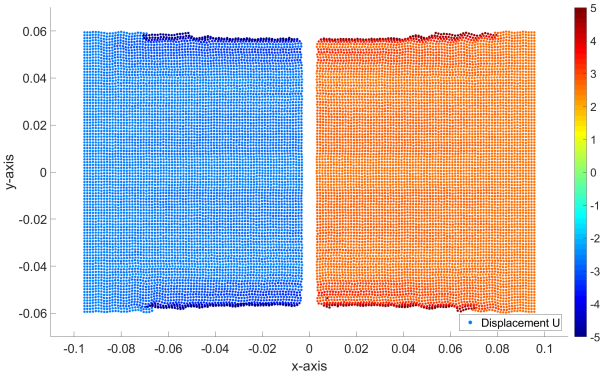


**(p)** Displacement U, Timestep 8500

**Figure 8-7:** Displacement in x-direction, damage initiation and crack growth sequence at increasing time steps

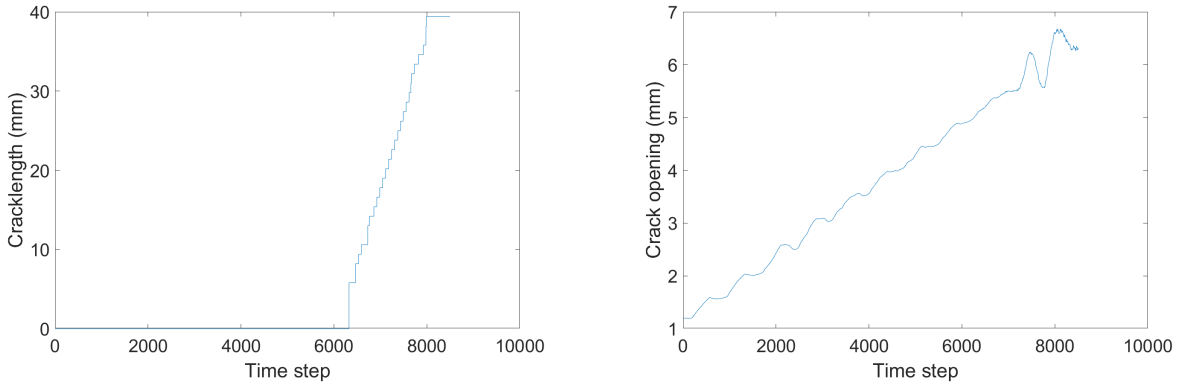


**(a)** Crack growth over time

**(b)** Crack opening displacement over time

**Figure 8-8:** The crack growth and crack opening versus the time step

The crack growth is initiated at lower displacement than seen during the actual tests. As already mentioned, the nonlinear properties, especially fiber shifting, is not included in failure prediction of this model. At the real test, the fiber-shifting of the transverse fiber, does not lead to a induced strain in the longitudinal fibers, since they simply slide over each other. At the model however, this sliding is not possible since the forces acting on the same material point and this material point can not be broken into multiple material points.

As a consequence, once the material points above and below the crack have a displacement in loading direction, the transverse bond-force vector induce a resulting force component in x- and y-direction. The resulting force vector in x-direction, induces a larger stretch between material point i and j located at the crack tip. This situation is sketched in Figure 8-9 for material point i. The same effect occurs for point j, where a resultant force will be present downwards.

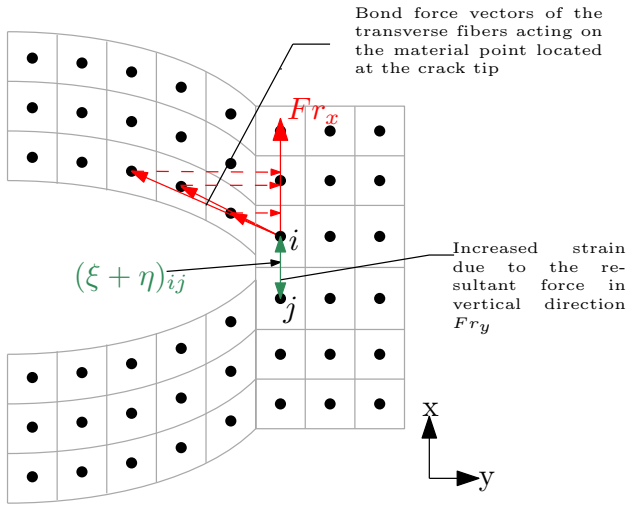


**Figure 8-9:** The resultant vertical force component of the bond-force vectors in transverse direction, increases the local stretch between material point i and j at the crack tip. This resultant force is not present at the test specimens, die due the free movement of the fibers relative to eachother.

Due to the larger stretch inflicted by the resultant force from the transverse fibers, the failure condition between the two material points is reached on an earlier stage than at the fracture tests itself. And once the first bond-forced fail, the rest of the bond-forces will follow, leading to the zipping effect as shown in Figure 8-7

## 8.4 Conclusion

In this chapter a numerical solution, based on the peridynamic framework, is proposed as a solution method for determination of the failure of the tsunami barrier. The method has been extended from a UD lamina model, to a bi-axial material model, such that the transverse fibers are taken into account in the simulation. Validation of the method showed good agreement between the displacements in loading direction determined by peridynamic simulation and compared to the analytical displacements using Hooke's law.

For the fracture simulation, the un-notched specimen failed under the exact defined failure strain. At the notched specimen, the crack induced a extra strain on the material points located at the crack tip, due the force component the transverse fibers induces on the longitudinal fibers. In reality, this force component is not present due to the fiber-shifting of the transverse fibers. Those non-linearities are not included in the model, resulting in conservative values for the nominal failure strain.

# Chapter 9

# Discussion

In this research, the Mode I fracture toughness of the cloth with Dyneema® fibers has been investigated in which the case of the tsunami barrier is translated to center cracked tensile specimen (CC(T)) specimens under quasi-static loading condition. The material consists of a single ply plain weave fabric, impregnated with a plastomer resin. The translation to a CC(T) specimen, has several implications on the actual design and load-case of the barrier and the materials used. In this chapter, the results of the fracture toughness tests are discussed and related to the tsunami barrier. The discussion concerning the fracture toughness of the Dyneema® cloth in relation to an aluminum reference panel is given in Section 9.1. Followed by an hypothesis for the tsunami barrier in Section 9.1.

## 9.1 Fracture toughness of the Dyneema® cloth

The fracture toughness tests on the Dyneema® cloth show a very different failure phenomena than seen at rigid carbon fiber reinforced polymers (CFRP) or aluminum. For a quantitative analysis of the fracture toughness, the failure loads of the Dyneema® fabric are compared to those of thin aluminum sheets under plane stress conditions. As reference, the fracture toughness test on large CC(T) specimens performed by Wang[50] made of aluminum grade AL7075-T6. Wang tested two widths with this grade, 76 and 121 mm and a thickness of 1.5 mm. These sheets are thus in de same order of magnitude as the Dyneema® sheets tested in this research. The strength properties and determined critical stress intensity factor $\mathcal{K}_{I_c}$ under plane stress for AL-7075-T6 is given in Table 9-1.

**Table 9-1:** Properties of AL7075-T6, source:Wang[50]

| Parameter | Unit | Value |
|---|---|---|
| $E$ | GPa | 71.7 |
| $\sigma_u$ | MPa | 532.3 |
| $\sigma_y$ | MPa | 468.154 |
| $\mathcal{K}_{I_c}$ | MPa·m$^{1/2}$ | 67 |

The properties from Table 9-1 are used to the determine the failure loads for panels with equal dimensions as used for the fracture toughness tests of the Dyneema® cloth. The failure loads are determined by rewriting Eq. (7-1) and substituting the values from Table 9-1 into the equation. The geometry factor ($a/W$), is determined using the Fedderson's equation as given in Eq. (7-2). The resulting failure loads for 3 specimens, with widths of 120, 288 en 900 mm and an initial notch of $a/w = 1/3$ are given in Table 9-2.

In Table 9-2 the first three columns give the width, crack length and crack over width ratio. The fourth column, gives the failure force in kN of an un-notched cross-sectional area. The fifth column gives the failure loads, based on net-section yielding of the cross-sectional area without taking into effect any stress intensity factors. Columns 6 and 7 give the nominal failure stress and corresponding

**Table 9-2:** Failure loads of the aluminum reference panels

| 2W | $2a_0$ | $a/w$ | $F_{fail}$ Unnotched | $F_{fail}$ Notched, nom | $\sigma_{fail}$ notched | $F_{fail}$ notched |
|---|---|---|---|---|---|---|
| (mm) | (mm) | (-) | (kN) | (kN) | (MPa) | (kN) |
| 120 | 40 | 1/3 | 45.4 | 30.2 | 249 | 21.24 |
| 288 | 96 | 1/3 | 108.8 | 72.6 | 161 | 32.9 |
| 900 | 300 | 1/3 | 340.1 | 226.8 | 91 | 58.15 |

load calculated using Eq. (7-1), at which the value for $\mathcal{K}_{I_c}$ from Table 9-1 is substituted into the equation.

The failure loads and strength reduction of aluminum panels is compared to the values of the Dyneema® fabric, which where determined in Chapter 6. The values are given in Table 9-3

**Table 9-3:** Comparison of the strength reduction of the Dyneema® cloth compared with aluminum when a crack is present

| | | | **Aluminum** | | **Dyneema** | |
|---|---|---|---|---|---|---|
| $W$ | $2a_0$ | $\frac{2a_0}{W}$ | $F_{fail}$ | Strength | $F_{fail}$ | Strength |
| (mm) | (mm) | $\frac{1}{3}$ | (kN) | Reduction | (kN) | Reduction |
| 120 | 40 | $\frac{1}{3}$ | 30.2 | -30 % | 14.62 | -22.1 % |
| 288 | 96 | $\frac{1}{3}$ | 72.6 | -55 % | 39.8 | -18 % |
| 900 | 300 | $\frac{1}{3}$ | 226.8 | -74 % | 84.4 | -40.1 % |

Both the aluminum and the Dyneema® fabric show a large reduction in failure strength with increasing specimen size. Compared to the aluminum sheets, where the reduction for the 120, 288 and 900 mm width specimens are 30%, 55% and 74% respectively, the Dyneema® cloth shows reductions of 22%, 18% and 40%. The difference between the small and medium specimens is relative small, with the medium specimens showing a bit better results. This difference is due to some fiber slip at the edges of the small specimens, as explained in Section 6.2.1, reducing the failure load of the small specimen. If the difference between the two sheets with a width of 900mm is examined, the aluminum fails at a loading that is only 25% of the nominal failure load while the Dyneema® sheet failed at 60%. The nonlinear crack-tip behavior of te Dyneema® cloth and the strength-dominant failure mode is therefore beneficial for the fracture toughness of the Dyneema® cloth.

## 9.2 Fracture toughness of the tsunami barrier

Now that the intrinsic material properties of the cloth and its fracture toughness has been characterized, a hypothesis can be made for the tsunami barrier.

As mentioned in Chapter 2, the Dyneema® cloth will form a tsunami barrier of hundreds of meters along a coastline, with a contour length of approximately 40 meters high. Due to the fabrication process, the maximum width of each sheet is limited to 3.2 meters. Therefore, to protect a coastline for several kilometers, sheets have to be connected in order to make a watertight barrier. Although there is no detailed design of those connections available, it can be assumed that the sheets will be stitched together. The tensile force is induced in the cloth by the water pressure, which follows the distribution as shown in Figure 2-1.

Considering the load-case of the barrier, all tests in this research are performed under quasi-static conditions. A constant velocity was applied at te edge of the sheet, which was fully constrained. This leads in essence to an equal load distribution throughout the material. In case of a tsunami event however, the loading of the barrier is dynamic and irregular. Not only the loading rates will be increased, the loading will not equally be distributed over the surface of the cloth. The literature survey showed that increasing loading rates is beneficial for the stiffness and fracture toughness of Dyneema® [29].

When a crack is present, the test results showed that no stress redistribution takes place from the damaged parts of the cloth towards the outer areas. It might be that due to the height of the cloth, eventually stress redistribution takes place. No signs during testing indicated that this might be the case since the shear band run to the clamps as is shown by the marker line in Figure 6-3b. It is also not expected that the crack will grow substantially over de length of the cloth.

When the freedom om movement of the cloth is examined, the water pressure will try to force the cloth in an out-of-plane displacement, defined as the z-direction. The force will in first instance be carried by the longitudinal fibers. But when a crack is present, the longitudinal fibers will not be capable of withstanding the load. It is not expected however, that a crack lead to complete failure of the damaged section. In Figure 9-1, a schematic cross-section is given viewed from the top. It is expected that as soon as a crack is initiated, the crack flanges will be pushed away by the water in z-direction. Once the cloth displaces in z-direction, it is expected that the transverse fibers, running above and below the crack, will become loaded under tensile. This will relieve the stress on the damaged area of the cloth by creating a new load balance, on the assumption that the connections between sheets is capable of transferring te loads.

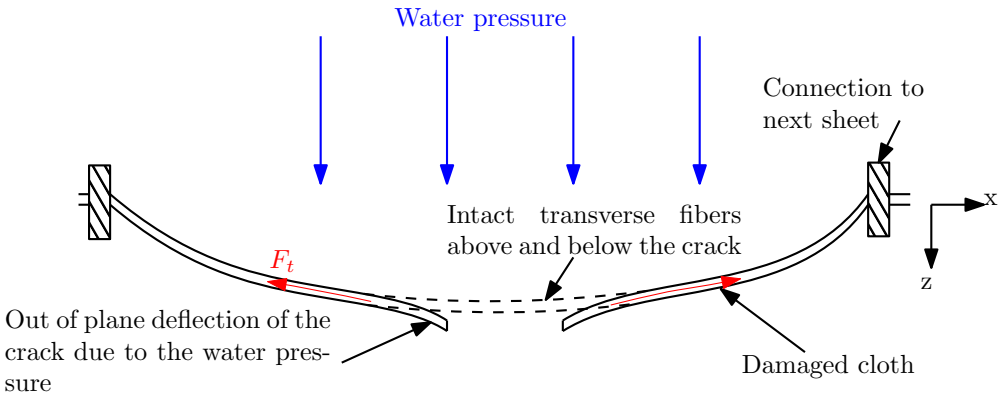


**Figure 9-1:** Schematic representation of the out-of-plane deflection of the crack flanges, counteracted by the intact transverse fibers above and below the crack, seen from a top view.

This can be expected from the change of boundary condition at the sides of the specimen. At the fracture mechanics tests, the sides of the sheets where free, leaving a certain degree of freedom on the transverse fibers. As a result, no tension was developed transversely, allowing the transverse fibers to follow the large crack opening. At the barrier however, the sides of the barrier are stitched together, enforcing a constraint on the transverse fibers. This will lead to biaxial loading of the cloth.

# Chapter 10

# Conclusion & Recommendations

## 10.1 Conclusion

The work and methods used in this research aimed to provide an answer to the main research question, defined in Chapter 1 as:

*"What are the intra-laminar fracture toughness characteristics of a notched cloth with Dyneema® fibers quasi-static loading and can a tool be developed to determine the critical damage of the flood barrier?"*

To answer the main research question, first the additional research questions from Chapter 3 are answered.

- *"Can the intra-laminar fracture toughness parameters of the cloth with Dyneema® fibers be determined using a center cracked tensile specimen (CC(T)) specimen?"*

  The behavior of the Dyneema® fabric and its failure phenomena are different compared to metals ans rigid composites. The fracture toughness tests on the CC(T) specimens, show that no stress redistribution takes place far away from the crack preventing a constant nominal stress. The maximum toughness af the cracked specimen equals 8.85 $^{MJ}/_{m^3}$ for the specimens with a width of 120 mm and an initial crack of 40 mm. Failure modes encountered during testing are fiber-shifting, fiber pull out, matrix release and eventually fiber breakage. Macroscopically the crack tip blunted into an elliptical form due to crack opening displacement which is as large as the elongation of the material. Although all tests show a reduction in the expected failure load due to the presence of the crack. Failure is not preceded by stable crack extension, but sudden and "explosive" and occurs when the net cross section reaches the ultimate stress level. Therefore the material failure is strength and not fracture mechanics dominant.

- *"Is the linear-elastic fracture mechanics (LEFM) theory applicable to determine a critical stress intensity factor and strain energy release rate for the fabric based on CC(T) specimen, such that failure of the tsunami barrier can be described using these constants analytically?"*

  The analytical solution based on the LEFM theory is not valid for the Dyneema® fabric. The analytical stress along the line $\theta = 0$ based on the anisotropic stress equations show a clear $^1/\sqrt{\pi a}$ and with overall stress levels below the ultimate stress level, except at the root, where the stress goes, as expected, to infinite. However, the actual stresses along that line obtained from the DIC system shows that the stress is in reality near constant, except at the crack tip, where due to the large strain in the plastomer resin, the stress increases. The peak stress at the crack tip shown by the DIC is mainly due to the release of the matrix material from the longitudinal fibers due to the fiber shifting of the transverse fibers, which are forced to follow the elliptical contour of te crack due to the high crack opening displacements. Due to this behavior of the cloth, it is impossible to determine the critical stress intensity factors as a single material property. Therefore, linear-elastic fracture mechanics (LEFM) is not suitable as failure prediction method for the tsunami barrier.

- *Can the crack growth of the Dyneema® fabric be modeled with peridynamics and can the model be used to determine critical crack sizes in the tsunami barrier?*

  The Peridynamic simulation is well capable of modeling fracture and crack growth of the material, taking into account the differences in Young's modulus and failure strain with respect to the longitudinal and transverse directions. Crack initiation of the un-notched reference model, started at around the defined failure stretch. For the notched specimens, the failure strains were conservative compared to the actual tests. This is due to the fact that this PD simulation does not account for the non-linear behavior of the material, especially fiber-shifting around the crack tip. As a result, the longitudinal component of the induced force from the transverse fibers, acting on the material points around the crack tip, increase the local strain. Therefore, crack growth is visible in a earlier stage than during the tests, leading to a conservative result of the nominal failure strain.

By finding the answers on the sub-questions we can now answer the main research question:

- *"What are the intra-laminar fracture toughness characteristics of a notched cloth with Dyneema® fibers under quasi-static loading?"*

  The intra-laminar fracture toughness characteristics of the Dyneema® cloth are very different compared to carbon fiber reinforced polymers (CFRP) or metals, due to the flexible and non-linear characteristics of the material. Fiber-shifting, matrix release, fiber pull-out and fiber breakage are present as failure modes. Very limited crack growth is visible, while the crack opening itself is almost as large as the nominal strain of the material. Failure occurs Due to the nature of the material, it is not possible to determine stress intensity factors as a single material property. However, compared to aluminum reference panels, the relative remaining strength of the material in large sheets with large crack sizes is much higher, showing taht the material is better in cooping with large cracks.

- *Can a tool be developed to determine the critical damage of the flood barrier?"* Two method for failure prediction are investigated. Analytically based on the LEFM and numerically based on the peridynamics (PD) theory. From the results of the analytical it can be concluded that the LEFM approach is invalid. The PD simulation is capable of dealing with crack growth in anisotropic materials, but has to be extended for the non-linearities of the material.

For the tsunami barrier, the Dyneema® cloth proved to be a good material to use. Since the failure remain strength-dominant, the wide sheets retains high failure strengths when large notches are present. The regions around the crack are limited effected by the redistribution of the stress. When the sides of the sheets are connected, it is expected that the transverse fiber will start taking up load due to the out of plane deflection if the material when a crack is present, increasing the fracture toughness of the cloth.

## 10.2 Recommendations

In this section, based on the conclusion, recommendations for further testing and analysis of the Dyneema® fabric with the purpose to the tsunami barrier are stated.

- **Improvements for fracture toughness testing:**
  - Clamping conditions:
    The fracture tests showed how difficult it was to obtain proper fixation within in the clamps, especially when the MTS3500kN machine was used with bolts that went through the material. For further testing, it is recommended that clamps are used, which do not penetrate the material within the clamps, reducing the effective clamping area of the fibers. Additionally, it can be investigated when laminates are tested, how the load distribution between the layers will be.
  - Different loading rates:
    In this research, the Dyneema® cloth is tested under quasi static uni-axial tensile loading. In reality during a flood event, the barrier will experience dynamic bidirectional loading at which the stress distribution in the fabric is likely to be unequal along the width. It is therefore recommended to test the fabric under different load-cases and loading rates to see what the effect of bi-axial and rate of loading is on fracture toughness of the material.
  - Testing for inter-laminar fracture toughness:
    This research focuses on the t intra-laminar fracture characteristics of a single ply material. The tsunami barrier itself will consists multiple layers, depending on the safety factor used. Multiple layer material introduces additional failure modes, like delamination. Also, the out-of plane bending due to the water pressure on the barrier, may lead to combined Mode I, Mode II Mode III fracture modes. It is therefore recommended for further research to take these additional failure modes into account.
- **Improvements for the PD simulation** The peridynamic simulations proved to be conservative in calculating failure strains when a notch is present due to the non-linear behavior of the material which is not implemented in the code. The simulation can be improved the following ways:
  - Extend the material model with a non-linear law, such that the initial non-linearities at the stress-strain curves an be taken into account.
  - Add multiple material points per ply in the thickness direction, such that the longitudinal and transverse fibers layers are capable of shifting.
  - Model the matrix material as a separate layers, with additional matrix release parameters.

  Additionally, the PD simulation can further be extended for modeling laminates with multiple plies and having fiber orientations in different directions. Additional material properties can be implemented into the code, based on the inter-laminar fracture toughness parameters of a laminate. This way, delamination can be added to the simulation.

# Bibliography


[1] Wikipedia. *List of floods*, 2017. https://en.wikipedia.org/wiki/List_of_floods.

[2] F. van der Ziel. *Symposium Afsluitbaar Open Rijnmond*. In -, pages –. TU Delft and Royal Haskoning, 2010. http://www.slideshare.net/Floris_van_der_Ziel/parachutekering-en-duurzaamheid-aor-symposium-janfeb2010-fvd-ziel.

[3] R. Marissen and D. Wienke. *Barrier System*, 2012. https://register.epo.org/application?number=EP12712677&lng=en&tab=main.

[4] R. Marissen, J. Mulder, D. Wienke, and O. Bergsma. *Design Considerations on a Flexible Membrane Tsunami Flood Barrier. Materials Sciences and Applications*, 4(December):846–855, 2013. doi: 10.4236/msa.2013.412108. http://dx.doi.org/10.4236/msa.2013.412108.

[5] B. Hofland, R. Marissen, and O. Bergsma. *Tsunami Structures*. In *Coastal Structures and Solutions to Coastal Disasters 2015*, number September, pages 235–245, Reston, VA, jul 2017. American Society of Civil Engineers. ISBN 9780784480311. doi: 10.1061/9780784480311.024. http://ascelibrary.org/doi/10.1061/9780784480311.024.

[6] B. Horsten. *Design Study of a Flexible-Membrane Tsunami Barrier Concept*. PhD thesis, Delft University of Technology, 2016.

[7] D. Demco, C. Melian, J. Simmelink, V. Litvinov, and M. Möller. *Structure and dynamics of drawn gel-spun ultrahigh-molecular-weight polyethylene fibers by 1H, 13C and 129Xe NMR. Macromolecular Chemistry and Physics*, 211(24):2611–2623, 2010. doi: 10.1002/macp.201000455.

[8] Granta Design. *CES EduPack 2016*, 2016. http://www.grantadesign.com/education/edupack/.

[9] R. Marissen. *Design with Ultra Strong Polyethylene Fibers. Materials Sciences and Applications*, 02(05):319–330, 2011. doi: 10.4236/msa.2011.25042. http://www.scirp.org/journal/PaperDownload.aspx?DOI=10.4236/msa.2011.25042.

[10] M. C. Sobieraj and C. M. Rimnac. *Ulta High Molecular Weight Polyethylene: Mechanics, Morphology, and Clincial Behavior. J Mech Behav Bomed Mater*, 2(5):433–443, 2009. doi: 10.1016/j.jmbbm.2008.12.006.

[11] Borealis. *Queo 8210*, 2016. http://www.borealisgroup.com/en/polyolefins/products/Queo/Queo-8210/.

[12] S. Lekhnitskii, S. Tsai, and T. Cheron. *Anisotropic Plates*. Gordon and Breach Science Publishers, Moscow, 1st edition, 1968. ISBN 0-677-20670-4.

[13] I. Daniel. *Engineering Mechanics of Composite Materials*. Oxford University Press, Inc., 2nd edition, 2006. ISBN 978-0-19-515097-1.

[14] C. Kassapoglou. *Design and Analysis of Composite Structures with Applications to Aerospace Structures*. John Wiley & Sons, Ltd, 2nd edition, 2013. ISBN 9781118401606.

[15] A. Griffith and G. Taylor. *VI. The Phenomena of Rupture and Flow in Solids*. pages 193–198, 1920.

[16] H. Westergaard. *Bearing pressures and cracks. Journal of Applied Mechanics*, 6:A49–A53, 1939.

[17] M. Janssen, J. Zuidema, and R. Wanhill. *Fracture Mechanics*. Delft Academic Press, Delft, first edition, 2002. ISBN 9789040722219. `http://www.delftacademicpress.nl/m004.php`.

[18] T. Anderson. *Fracture Mechanics, Fundamentals and Applications*. CrC Press, 2nd edition, 1996. ISBN 0849342600.

[19] G. Irwin. *Analysis of stresses and strains near the end of a crack traversing a plate. Journal of Applied Mechanics*, 24:361–364, 1957.

[20] H. Tada, P. Paris, and G. Irwin. *The Stress Analysis of Cracks Handbook*. Professional Engineering Publisher, 3rd edition, 2000. ISBN 1-86058-304-0.

[21] G. Irwin. *Onset of Fast Crack Propagation in High Strength Steel and Aluminum Alloys. Sagamore Research Conference Proceedings*, (May 1956):289–305, 1956.

[22] Y. Lei and B. Neale. *The Fracture Behaviour of a Centre Cracked Tensile Specimen. Fatique Frac. Engng. Mater. Struct.*, 20(2):201–216, 1997. doi: 8756-758X/97.

[23] G. Sih, P. Paris, and G. Irwin. *On cracks in rectilinearly anisotropic bodies. International Journal of Fracture Mechanics*, 1(3):189–203, 1965. doi: 10.1007/BF00186854.

[24] E. Wu. *Application of fracture mechanics to anisotropic plates. Journal of Applied Mechanics*, 34(4):967–974, 1967. doi: 10.1115/1.3607864. `http://appliedmechanics.asmedigitalcollection.asme.org/article.aspx?articleid=1398422`.

[25] S. Parhizgar, L. Zachary, and C. Sun. *Application of the principles of linear fracture mechanics to the composite materials. International Journal of Fracture*, 20(1):3–15, 1982. doi: 10.1007/BF00942161.

[26] R. Marissen, T. Westphal, and J. Sterk. *Fracture of quasi-isotropic composite sheets with sharp notches. Composites Science and Technology*, 66:1803–1812, 2006. doi: 10.1016/j.compscitech.2005.10.020.

[27] A. Porras and J. Tellez. *Delamination toughness of ultra high molecular weight polyethylene ( UHMWPE ) composites*. 02016:2–5, 2012. doi: 10.1051/epjconf/20122602016.

[28] T. Lässig, F. Nolte, W. Riedel, and M. May. *An Assessment of Experimental Techniques for Measuring the Mode I Fracture Toughness of Uhmw-Pe Composites*. (June):26–30, 2016.

[29] M. May, T. Lässig, and S. Hiermaier. *an Investigation on the Influence of Loading Rate on the Fracture Toughness of Uhmw-Pe Composites*. In *ECCM17*, number June, pages 26–30, 2016.

[30] S. Mohammadi. *XFEM Fracture Analysis of Composites*. John Wiley & Sons, Ltd, 1st edition, 2012. ISBN 9781118443316. `http://ebookcentral.proquest.com.tudelft.idm.oclc.org/lib/delft/detail.action?docID=1013404`.

[31] S. Silling. *Reformulation of elasticity theory for discontinuities and long-range forces. Journal of the Mechanics and Physics of Solids*, 48(1):175–209, jan 2000. doi: 10.1016/S0022-5096(99)00029-0. http://linkinghub.elsevier.com/retrieve/pii/S0022509699000290.

[32] B. Kilic, A. Agwai, and E. Madenci. *Peridynamic theory for progressive damage prediction in center-cracked composite laminates. Composite Structures*, 90(2):141–151, 2009. doi: 10.1016/j.compstruct.2009.02.015. http://dx.doi.org/10.1016/j.compstruct.2009.02.015.

[33] S. Silling and E. Askari. *A meshfree method based on the peridynamic model of solid mechanics. Computers and Structures*, 83(17-18):1526–1535, 2005. doi: 10.1016/j.compstruc.2004.11.026.

[34] E. Madenci and E. Oterkus. *Peridynamic Theory and Its Applications*. Springer New York, New York, NY, 2014. ISBN 978-1-4614-8464-6. doi: 10.1007/978-1-4614-8465-3. http://link.springer.com/10.1007/978-1-4614-8465-3.

[35] E. Oterkus, A. Barut, and E. Madenci. *Peridynamics Based on Principle of Virtual Work. 53rd AIAA/ASME/ASCE/AHS/ASC Structures, Structural Dynamics and Materials Conference*, (April):1–25, 2012. doi: 10.2514/6.2012-1540.

[36] E. Oterkus and E. Madenci. *Peridynamic analysis of fiber-reinforced composite materials. Journal of Mechanics of Materials and Structures*, 7(1):45–84, mar 2012. doi: 10.2140/jomms.2012.7.45. http://msp.org/jomms/2012/7-1/p03.xhtml.

[37] Y. Hu, Y. Yu, and H. Wang. *Peridynamic analytical method for progressive damage in notched composite laminates. Composite Structures*, 108(1):801–810, 2014. doi: 10.1016/j.compstruct.2013.10.018.

[38] ASTM. *D3039/D3039M-14 - Standard Test Method for Tensile Properties of Polymer Matrix Composite Materials*. pages 1–13, 2016. doi: 10.1520/D3039.

[39] ASTM. *E132-04 - Standard Test Method for Poisson's Ratio at Room Temperature. ASTM Book of Standards*, 04(Reapproved 2010):2010–2012, 2010. doi: 10.1520/E0132-04R10. https://compass.astm.org/download/E132.31277.pdf.

[40] ASTM. *D3518 - Standard Test Method for In-Plane Shear Response of Polymer Matrix Composite Materials by Tensile Test of a ± 45* deg *Laminate*. 94(Reapproved):1–7, 2007.

[41] ASTM. *D792-13 - Standard Test Methods for Density and Specific Gravity (Relative Density) of Plastics by Displacement*. page 6, 2008. doi: 10.1520/D0792-08.2. https://doi.org/10.1520/D0792.

[42] ISO. *NEN-ISO 13586 (en) -Kunststoffen - Bepaling van de breuktaaiheid ($G_{Ic}$ en ĐŽ$_{Ic}$) - Benadering met lineair elastische breukmechanica (LEFM)*, 2000.

[43] ASTM. *E561-15 - Standard Test Method for $K_R$ Curve Determination*, 2015.

[44] Gerber Technology. *Gerbercutter DSC2500*. http://www.gerbertechnology.com/aerospace/ply-cutting/gerbercutter-dcs-2500/.

[45] X.-K. Zhu and J. Joyce. *Review of fracture toughness (G, K, J, CTOD, CTOA) testing and standardization. Engineering Fracture Mechanics*, 85:1–46, may 2012. doi: 10.1016/j.engfracmech.2012.02.001. http://www.sciencedirect.com/science/article/pii/S001379441200063X.

[46] Correlated Solutions. *VIC 3Dv7 Reference Manual*, 2017. http://www.correlatedsolutions.com/supportcontent/Vic-3D-v7-Manual.pdf.

[47] M. Sutton, J.-J. Orteu Schreier, and A. Hubert. *Image Correlation for Shape, Motion and Deformation Measurements*, volume 53. 2009. ISBN 9788578110796. doi: 10.1017/CBO9781107415324.004.

[48] D. Brown. *Tracker Video Analysis and Modeling tool*, 2018. `https://physlets.org/tracker/`.

[49] S. Silling and F. Bobaru. *Peridynamic modeling of membranes and fibers. International Journal of Non-Linear Mechanics*, 40(2-3):395–409, mar 2005. doi: 10.1016/j.ijnonlinmec.2004.08.004. `http://linkinghub.elsevier.com/retrieve/pii/S0020746204001027`.

[50] D. Wang. *Plane-stress fracture toughness and fatigue crack propagation of aluminum alloy wide panels. Progress in Flaw Growth and Fracture Toughness Testing (ASTM STP 536)*, pages 334–349, 1973.

[51] E. Oterkus and E. Madenci. *Peridynamic Theory for Damage Initiation and Growth in Composite Laminate. Key Engineering Materials*, 488-489(1):355–358, 2011. doi: 10.4028/www.scientific.net/KEM.488-489.355. `http://www.scientific.net/KEM.488-489.355`.

[52] M. Ghajari, L. Iannucci, and P. Curtis. *A peridynamic material model for the analysis of dynamic crack propagation in orthotropic media. Computer Methods in Applied Mechanics and Engineering*, 276:431–452, jul 2014. doi: 10.1016/j.cma.2014.04.002. `http://dx.doi.org/10.1016/j.cma.2014.04.002http://linkinghub.elsevier.com/retrieve/pii/S004578251400111X`.

# Appendices

# Appendix A

# Material Properties

This appendix contains the test report to determine the physical properties and anisotropic engineering constants of the Dyneema® fabric. These properties are unknown but required to construct the stiffness and compliance matrices and to determine the strength values. and for the application of the fracture mechanics or numerical modeling methods. The appendix contains three sections. In Section A.1 the properties of the test benches and other hardware, like strain gages, used during testing are given. In the second section, Section A.2, the test results are given for the determination of physical properties. In Section A.3.1

## A.1 Test bench set-up

### A.1.1 Strain Gages

The strain gages used for the experiments are of the type "KFEL-5-120-D34" Biaxial High Strain Failure, manufactured by Kyowa Electronic Instruments Co.,LTD. The properties are given in Table A-1. The strain gages are attached to a Peekel Picas multichannel amplifier system, using a 1/4-Bridge configuration at 120 Ω. The settings of the amplifier are given in Table A-2. The sensitivity of measurement is set to 50 $^{mV}/_{V}$, which indicates that an increase of 1 $V$ indicates an increase in strain of 1%.

**Table A-1:** Properties of KFEL-5-120-D34 Biaxial strain gage, 120Ω Biaxial, 0°/90°

| **Property** | **Value** | **Property** | **Value** |
|---|---|---|---|
| Base length | 13 mm | Gage factor (24°C, 50%RH) | (1) 2.08, (2) 2.08 ± 1.0% |
| Base width | 13 mm | Gage length | 5 mm |
| Grid length | 5 mm | Gage resistance (24°C, 50%RH) | 120.0 ± 0.8 Ω |
| Grid width | 2.1 mm | Strain limit | 15 % |
| **Layout:** | 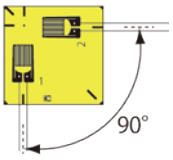  | Adoptable thermal expansion | - PPM/ °C |
| | | Temperature coefficient of gage factor | +0.015 % / °C |
| | | Lot no. / Batch | Y317 / 049A W07 |
| | | Applied adhesive | CC-36 |

### A.1.2 Digital image correlation (DIC) Set-up

Digital image correlation (DIC) is used to acquire full field strain and displacement data by calculating the relative displacements of a speckle field. In Table A-3 the settings of the DIC correlation

**Table A-2:** Settings Peekel Picas Multichannel Amplifier

| Setting | Value | Setting | Value |
|---|---|---|---|
| Sensitivity | 50 mV/V | Signal Mode | normal |
| Bridge Volt | 5.5 | Signal Polarity | normal |
| Bridge Configuration | 1/4 Bridge | Bridge Load | 120 Ω |
| Bridge Factor | 1 | $\kappa$-factor | 2.08 |

are stated. In this section, the results of the correlation for each separate test sample is shown, Section B.4 for the specimens with a width of 120 mm, Section B.4 for the specimens with a width of 288 mm and Section B.4 fo the specimens with a width of 900 mm. The strains and displacements shown, are taken in all cases from the last timestep before failure occurs. For each the tensile strain $\epsilon_y$, shear strain $\gamma_{12}$ and displacement in y-direction $V$ are given, since those are the most relevant parameters for this research.

**Table A-3:** Settings DIC correlation

| Setting | Value |
|---|---|
| Subset size | 27 - 31 |
| Stepsize | 4 |
| Subset weights | Gaussian weights |
| Interpolation | Optimized 8-trap |
| Criterion | Zero-normalized squared differences |
| Low-pass filter image: | off |
| Incremental correlation: | on |
| Exhaustive search: | on |
| Filter size for strain cal. | 15 |

## A.2 Testing of physical properties

### A.2.1 Statistical law

The mean value of the density is determined using the statistics law from ASTM-D3039[38] defined by the following set of equations:

$$\bar{x} = \frac{\sum_{i=1}^{n} x_i}{n}, \qquad s_{n-1} = \sqrt{\frac{\sum_{i=1}^{n} x_i^2 - n\bar{x}^2}{n-1}}, \qquad CV = \frac{100 * s_{n-1}}{\bar{x}} \tag{A-1}$$

Where: $\bar{x}$ denoted the sample mean value, $s_{n-1}$ the standard deviation, $CV$, the coefficient of variation, $n$ the number of specimens and $x_i$ the measured value.

### A.2.2 Physical properties

#### Density

The density of the Dyneema® cloth is measured using ASTM-D792[41] standard, in which a specimen is weighted both in air and in an auxiliary liquid. The density is calculated using the following

relationship:

$$\rho = \frac{m_{dry}}{m_{dry} - m_{wet}} (\rho_0 - \rho_l) + \rho_l \tag{A-2}$$

In which $\rho$ is the material density, $\rho_0$ the density of the auxiliary liquid, $\rho_l$ the density of air, $m_{dry}$ weight if the sample in air and $m_{wet}$ the weight of the sample when placed in the auxiliary liquid.

The auxiliary liquid used is water. The temperature of the liquid measured during the test is 22.6 $°C$, the corresponding density is 0.99766 $g/cm^3$. The density of air equals 0.0012 $g/cm^3$. The results of the measurements are given in Table A-4. The last column in the table shows the relative density calculated using Eq. (A-2).

**Table A-4:** Density measurement

| Specimen ID | Weight in air | Weight in liquid | Density |
|---|---|---|---|
| | $g$ | $g$ | $g/cm^3$ |
| Specimen 1 | 0,3741 | -0,0423 | 0,90 |
| Specimen 2 | 0,3770 | -0,0519 | 0,88 |
| Specimen 3 | 0,3715 | -0,0433 | 0,89 |
| Specimen 4 | 0,4724 | -0,0639 | 0,88 |
| Specimen 5 | 0,5359 | -0,067 | 0,89 |
| Specimen 6 | 0,4648 | -0,0495 | 0,90 |

From the measurement data, the average density is determined by substituting the results from Table A-4 into the statistical law given in App. A.2.1. The average value, standard deviation and relative error are given in Table A-5.

**Table A-5:** Statistics density measurements

| Mean value | Standard deviation | Relative error |
|---|---|---|
| $\bar{x}$ $g/cm^3$ | $s_{n-1}$ $g/cm^3$ | $CV$ % |
| 0.89 | 0.0099 | 1.1 |

### Thickness

The thickness of the Dyneema® cloth is measured using a standard micrometer applied to 4 specimens. The average values and statistics are determined using the statistical equations given in Eq. (A-1)

**Table A-6:** Statistics density measurements

| Measurement: | 1 | 2 | 3 | 4 |
|---|---|---|---|---|
| Measured thickness $mm$ | 0.7 | 0.71 | 0.72 | 0.71 |
| Mean value | Standard deviation | | Relative error | |
| $\bar{x}$ $mm$ | $s_{n-1}$ $mm$ | | $CV$ % | |
| 0.71 | 0.0082 | | 1.15 | |

## A.3 Engineering constants

The engineering constants are determined from the stress-strain curves as given in Figure 5-1. The Young's modulus in each direction is calculated according to ASTM-D3039[38] using the relationship:

$$E^{chord} = \frac{\Delta\sigma}{\Delta\epsilon} \tag{A-3}$$

The Poissons ratio $\nu_{12}$ is determined according ASTM-E132[39] using the relationship:

$$\nu_{12} = \left(\frac{d\epsilon_t}{dP}\right)\left(\frac{d\epsilon_l}{dP}\right)^{-1} \tag{A-4}$$

In analogue way, according to ASTM-D3518[40] the shear chord modulus is determined as:

$$G_{12}^{chord} = \frac{\Delta\tau_{12}}{\Delta_{\gamma_{12}}} \tag{A-5}$$

Here, $\tau_{12}$ is defined as the in-plane shear stress: $\tau_{12} = {}^{P}/_{A}$, with $P$ the applied load and $A$ the cross-sectional area.

The results of the tensile tests in warp, weft and shear direction is summarized in Table A-7.

The transverse Poisson's ratio is determined using Eq. (2-8). Since the transverse Young's modulus consists of two phases, with the intersection at about 8%, two transverse Poissons's ratio are determined. The curvature of the transverse stress-strain graph at about 8% is ignored. The two values of the transverse Poisson's ratio are determined by the relationship $\nu_{21} = \nu_{12}\frac{E_2}{E_1}$ and are given in Table A-8.

### A.3.1 Classical laminate theorem (CLT)

#### Entries of the stiffness and compliance matrices

With the engineering constants known, the stiffness matrix $\mathcal{Q}$ and the compliance matrix $\boldsymbol{\mathcal{S}}$ can be constructed by substituting the values into Eq. (2-5) and Eq. (2-7) respectively. Since the Young's modulus of the transverse fiber direction changes at $\epsilon_{trans} = 0.08$, two matrices have to be constructed.

#### Values of the reduced stiffness matrix $\mathcal{Q}$

$$\mathcal{Q}_{1,2} = \begin{cases} \begin{bmatrix} 8.64 & 0.046 & 0 \\ 0.046 & 0.123 & 0 \\ 0 & 0 & 0.0248 \end{bmatrix} (GPa) & \text{for} \quad \epsilon_{trans} < 0.08 \\ \begin{bmatrix} 9.37 & 2.04 & 0 \\ 2.04 & 5.5 & 0 \\ 0 & 0 & 0.0248 \end{bmatrix} (GPa) & \text{for} \quad \epsilon_{trans} >= 0.08 \end{cases} \tag{A-6}$$

**Table A-7:** Dyneema cloth engineering constants

**Direction1 - Warp**

| Constant | Symbol | Unit | Average value | Standard deviation | Error (%) |
|---|---|---|---|---|---|
| Young's Modulus | $E_1$ | GPa | 8.62 | 0.18 | 2.1 |
| Poisson's ratio | $\nu_{12}$ | - | 0.37 | | |
| Failure force | $F_1^u$ | $^{kN}/_m$ | 234.8 | 2.9 | 1.27 |
| Failure stress | $X^t$ | MPa | 331 | 4.1 | 1.27 |
| Failure strain | $\epsilon_{1u}^t$ | % | 4.2 | 0.10 | 2.6 |

**Direction 2 - Weft**

| Constant | Symbol | Unit | Average value | Standard deviation | Error (%) |
|---|---|---|---|---|---|
| Young's Modulus slope 1 | $E_2$ | GPa | 0.123 | 8.1E-3 | 6.6 |
| Youngs Modulus slope 2 | $E_2$ | GPa | 5.07 | 0.24 | 4.8 |
| Failure force | $F_2^u$ | $^{kN}/_m$ | 163.2 | 3.01 | 1.8 |
| Failure stress | $Y^t$ | MPa | 229 | 4.2 | 1.8 |
| Failure strain | $\epsilon_{2_u}^t$ | % | 13 | 0.22 | 1.7 |

**Direction 12 - Shear**

| Constant | Symbol | Unit | Average value | Standard deviation | Error (%) |
|---|---|---|---|---|---|
| Shear Modulus | $G_{12}$ | GPa | 0.0248 | 0.40E-3 | 3.2 |
| Failure strength | $F_s^u$ | $^{kN}/_m$ | 7.92 | 0.45 | 5.7 |
| Failure strain | $\gamma_{12_u}$ | % | 36 | 1.6 | 4.5 |
| Failure Stress | $S$ | MPa | 5.6 | 0.63 | 5.7 |

**Table A-8:** Values of $\nu_{21}$

| | |
|---|---|
| $\nu_{21} = 0.0053$ | For $\epsilon_{22} < 8\%$ |
| $\nu_{21} = 0.22$ | For $\epsilon_{22} \geq 8\%$ |

**Values of compliance matrix S**

$$\boldsymbol{\mathcal{S}}_{1,2} = \begin{cases} \begin{bmatrix} 0.116 & -0.043 & 0 \\ -0.043 & 8.1 & 0 \\ 0 & 0 & 40.3 \end{bmatrix} (GPa^{-1}) & \text{for } \epsilon_{trans} < 0.08 \\ \begin{bmatrix} 0.116 & -0.43 & 0 \\ -0.43 & 0.197 & 0 \\ 0 & 0 & 40.3 \end{bmatrix} (GPa^{-1}) & \text{for } \epsilon_{trans} >= 0.08 \end{cases} \tag{A-7}$$

### A.3.2 Stiffness matrix transformation

The general stiffness matrix transformation of the properties of the ply from coordinate system x-y to coordinate system 1-2, as shown in Figure A-1 are written as Eq. (A-8a) till Eq. (A-8f), in which $\cos\theta = m$ and $\sin\theta = n$. These equations can be found in any book about composites like Daniel[13] and Kassapoglou[14].

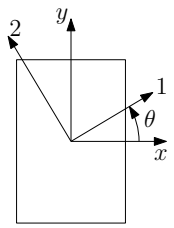


**Figure A-1:** Coordinate system rotation by angle $\theta$

$$Q_{xx}^{(\theta)} = m^4 Q_{11} + n^4 Q_{22} + 2m^2 n^2 Q_{12} + 4m^2 n^2 Q_{66} \tag{A-8a}$$
$$Q_{yy}^{(\theta)} = n^4 Q_{11} + m^4 Q_{22} + 2m^2 n^2 Q_{12} + 4m^2 n^2 Q_{66} \tag{A-8b}$$
$$Q_{xy}^{(\theta)} = m^2 n^2 Q_{11} + m^2 n^2 Q_{22} + (m^4 + n^4) Q_{12} - 4m^2 n^2 Q_{66} \tag{A-8c}$$
$$Q_{ss}^{(\theta)} = m^2 n^2 Q_{11} + m^2 n^2 Q_{22} - 2m^2 n^2 Q_{12} + (m^2 - n^2)^2 Q_{66} \tag{A-8d}$$
$$Q_{xs}^{(\theta)} = m^3 n Q_{11} - m n^3 Q_{22} - (m n^3 - m^3 n)(Q_{12} + 2Q_{66}) \tag{A-8e}$$
$$Q_{ys}^{(\theta)} = m n^3 Q_{11} - m^3 n Q_{22} - (m^3 n - m n^3)(Q_{12} + 2Q_{66}) \tag{A-8f}$$

The stresses and strains can be transformed by the following matrix transformation:

$$\begin{Bmatrix} \sigma_x \\ \sigma_y \\ \tau_{xy} \end{Bmatrix} = \begin{bmatrix} m^2 & n^2 & -2mn \\ n^2 & m^2 & 2mn \\ mn & -mn & m^2 - n^2 \end{bmatrix} \begin{Bmatrix} \sigma_1 \\ \sigma_2 \\ \tau_{12} \end{Bmatrix} \tag{A-9}$$

$$\begin{Bmatrix} \epsilon_x \\ \epsilon_y \\ \gamma_{xy} \end{Bmatrix} = \begin{bmatrix} m^2 & n^2 & -2mn \\ n^2 & m^2 & 2mn \\ mn & -mn & m^2 - n^2 \end{bmatrix} \begin{Bmatrix} \epsilon_1 \\ \epsilon_2 \\ \gamma_{12} \end{Bmatrix} \tag{A-10}$$

In this research, the directional properties of the Dyneema® fabric the warp direction, 1, is aligned with the x-y axis system as shown in Figure 2-5 are aligned with an angle of 90 degrees such that $E_y = E_1$.

# Appendix B

# Fracture Mechanics

In this appendix the fracture mechanics theory linear-elastic fracture mechanics (LEFM) theory is elaborated and applied onto the Dyneema® fabric. Starting with the application of anisotropic stress field equations as derived by Lekhnitskii et al.[12] for a notch in a infinite body in Section B.1 for the Mode I critical stress intensity factor (CSIF) $K_{I_c}$ is determined. Last section, Section B.4 provides the results of the digital image correlation (DIC) analysis for each test sample.

## B.1 Stress and displacement field, ahead of the crack tip for a linear elastic, anisotropic material under mode I loading

Figure B-1 shows the 3 components of stress, $\sigma_x$, $\sigma_y$ and shear stress $\tau_{xy}$ in an arbitrary two-dimensional body in the direct vicinity of the crack at coordinates $(r, \theta)$.

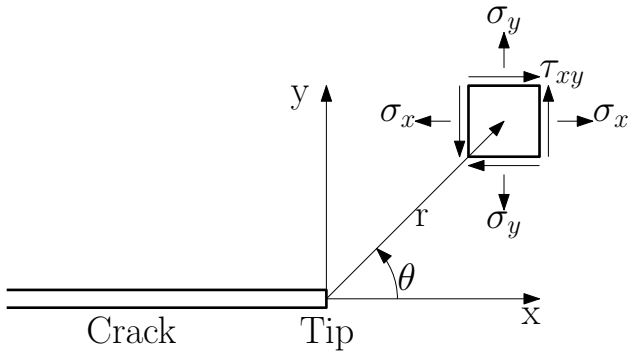


**Figure B-1:** Stress Components around the crack tip

The first equations for the stress and displacement field around the tip of crack in a two-dimensional infinite anisotropic body, under plane stress conditions was derived by Lekhnitskii et al.[12] and the equations are shown in Section B.1.1.

### B.1.1 Mode I

**Stress Field equations:**

$$\sigma_x = \frac{\mathcal{K}_I}{\sqrt{2\pi r}} Re\left[\frac{\mu_1\mu_2}{\mu_1 - \mu_2}\left(\frac{\mu_2}{\sqrt{\cos\theta + \mu_2 \sin\theta}} - \frac{\mu_1}{\sqrt{\cos\theta + \mu_2 \sin\theta}}\right)\right] \tag{B-1}$$

$$\sigma_y = \frac{\mathcal{K}_I}{\sqrt{2\pi r}} Re\left[\frac{1}{\mu_1 - \mu_2}\left(\frac{\mu_1}{\sqrt{\cos\theta + \mu_2 \sin\theta}} - \frac{\mu_2}{\sqrt{\cos\theta + \mu_2 \sin\theta}}\right)\right] \tag{B-2}$$

$$\tau_{xy} = \frac{\mathcal{K}_I}{\sqrt{2\pi r}} Re\left[\frac{\mu_1\mu_2}{\mu_1 - \mu_2}\left(\frac{1}{\sqrt{\cos\theta + \mu_2 \sin\theta}} - \frac{1}{\sqrt{\cos\theta + \mu_2 \sin\theta}}\right)\right] \tag{B-3}$$

In which $\mathcal{K}_I$ is the stress intensity factor and $\mu_1$ and $\mu_2$ material parameters determined by solving the following 4th order polynomial:

$$S_{11}\mu^4 - 2S_{16}\mu^3 + (2S_{12} + S_{66})\mu^2 - 2S_{26}\mu + S_{22} = 0 \tag{B-4}$$

The displacement field equations are by Lekhnitskii et al.[12] derived as:

$$u = \frac{\mathcal{K}_I}{\sqrt{2\pi r}} Re\left[\frac{1}{\mu_1 - \mu_2}\left(\mu_1 P_2 \sqrt{\cos\theta + \mu_2 \sin\theta} - \mu_2 P_1 \sqrt{\cos\theta + \mu_1 \sin\theta}\right)\right] \tag{B-5}$$

$$v = \frac{\mathcal{K}_I}{\sqrt{2\pi r}} Re\left[\frac{1}{\mu_1 - \mu_2}\left(\mu_1 q_2 \sqrt{\cos\theta + \mu_2 \sin\theta} - \mu_2 q_2 \sqrt{\cos\theta + \mu_1 \sin\theta}\right)\right] \tag{B-6}$$

The Parameters $P_1$, $P_2$, $q_1$ and $q_2$ are derived as:

$$\begin{aligned} P_1 &= S_{11}\mu_1^2 + S_{12} - S_{16}\mu_1 \quad & P_2 &= S_{11}\mu_2^2 + S_{12} - S_{16}\mu_1 \\ q_1 &= S_{12}\mu_1 + \frac{S_{22}}{\mu_1} - S_{26} \quad & q_2 &= S_{12}\mu_2 + \frac{S_{22}}{\mu_2} - S_{26} \end{aligned} \tag{B-7}$$

## B.2 Relationship between stress intensity factor (SIF) $\mathcal{K}_I$ and the strain energy release rate $\mathcal{G}$

The relationship between the SIF and strain energy release rate (SERR) is given by Tada et al.[20] as:

$$\mathcal{G} = \mathcal{C}\mathcal{K}^2 \tag{B-8}$$

The values of parameter $\mathcal{C}$ is material, stress state and crack opening mode depended. The equations to determine $\mathcal{C}$ in case of plane stress are given in Table B-1.

**Table B-1:** Values of C for isotropic, orthotropic and anisotropic materials under Mode I, II and III loading(Tada et al.[20])

| Mode i | Isotropic | Orthotropic $S_{16} = S_{26} = S_{45} = 0$ | Anisotropic |
|---|---|---|---|
| I | $1/E$ | $\sqrt{\frac{S_{11}S_{22}}{2}}\left[\sqrt{\frac{S_{22}}{S_{11}}} + \frac{2S_{12}+S_{66}}{2S_{11}}\right]^{1/2}$ | $-\frac{S_{11}}{2} Im\left(\frac{\mu_1+\mu_2}{\mu_1\mu_2}\right)$ |
| II | $1/E$ | $\frac{S_{11}}{\sqrt{2}}\left[\sqrt{\frac{S_{22}}{S_{11}}} + \frac{2S_{12}+S_{66}}{2S_{11}}\right]^{1/2}$ | $\frac{S_{11}}{2} Im\left(\mu_1+\mu_2\right)$ |
| III | $(1+\nu)/E$ | $\frac{1}{2}\sqrt{S_{44}S_{55}}$ | $\frac{1}{2}\frac{\left(S_{44}S_{55} - S_{45}^2\right)^{3/2}}{S_{44}S_{55}}$ |

## B.3 Analytical stress field for the Dyneema® fabric

In this section, the analytical stress field for the Dyneema® fabric with an initial notch, according to the above presented equations from Tada et al.[20]. For the calculation, the longitudinal material axis is aligned with the y-axis.

### B.3.1 Material parameters for $\epsilon_{trans} < 0.08$

#### Values for $\mu_1$ and $\mu_2$

The values for $\mu_1$ and $\mu_2$ are determined by solving Eq. (B-4). Substituting the values of $\boldsymbol{\mathcal{S}}$ as given in Eq. (A-7), gives the following equation:

$$S_{11}\mu^4 - 2S_{16}\mu^3 + (2S_{12} + S_{66})\mu^2 - 2S_{26} + S_{22} = 0 \tag{B-9}$$
$$8.12 \cdot 10^{-9}\mu^4 - 0 + (2 \cdot -4.29 \cdot 10^{-11} + 4.03 \cdot 10^{-8})\mu^2 - 0 + 1.16 \cdot 10^{-10} = 0 \tag{B-10}$$
$$8.12 \cdot 10^{-9}\mu^4 + 4.02 \cdot 10^{-08}\mu^2 + 1/16 \cdot 10^{-10} = 0 \tag{B-11}$$

The fourth order polynomial is solved numerically using MatLab. The resulting values for $\mu_1$ and $\mu_2$ are:

$$\mu_1, \mu_3 = 0 \pm 2.22i \tag{B-12}$$
$$\mu_2, \mu_4 = 0 \pm 0.054i \tag{B-13}$$

#### Values for $P_1$, $P_2$, $q_1$ and $q_2$

$P_1$, $P_2$, $q_1$ and $q_2$ are determined by substituting the values for $\mu$ in Eq. (B-13) into the equations given in Eq. (B-7).

$$P_1 = -4.03 \cdot 10^{-08} - 9.03 \cdot 10^{-24}i \quad q_1 = 4.86 \cdot 10^{-27} - 1.48 \cdot 10^{-10}i \tag{B-14}$$
$$P_2 = -6.64 \cdot 10^{-11} + 1.89 \cdot 10^{-28}i \quad q_2 = 8.71 \cdot 10^{-27} - 2.16 \cdot 10^{-09}i \tag{B-15}$$

### B.3.2 Material parameters for $\epsilon_{trans} \geq 0.08$

Since two compliance matrices are constructed, the anisotropic material parameters change when $\epsilon_{trans} > 0.08$. Following the same procedure, but changing the values of the compliance matrix gives the following results:

#### Values for $\mu_1$ and $\mu_2$

The fourth order polynomial is solved numerically using MatLab. The resulting values for $\mu_1$ and $\mu_2$ are:

$$\mu_1, \mu_3 = 0 \pm 14.3i \tag{B-16}$$
$$\mu_2, \mu_4 = 0 \pm 0.054i \tag{B-17}$$

#### Values for $P_1$, $P_2$, $q_1$ and $q_2$

$P_1$, $P_2$, $q_1$ and $q_2$ are determined by substituting the values for $\mu$ in Eq. (B-13) into the equations given in Eq. (B-7).

$$P_1 = -4.03 \cdot 10^{-08} - 5.62 \cdot 10^{-24}i \quad q_1 = 4.23 \cdot 10^{-26} - 6.21 \cdot 10^{-10}i \tag{B-18}$$
$$P_2 = -4.34 \cdot 10^{-11} + 8.61 \cdot 10^{-30}i \quad q_2 = 1.63 \cdot 10^{-26} - 2.16 \cdot 10^{-09}i \tag{B-19}$$

### B.3.3 Analytical procedure to determine the stress intensity factor

For the center cracked tensile specimen (CC(T)) specimen, the equation to determine the mode I SIF under loading P is given by equation:

$$\mathcal{K}_I = \frac{P\sqrt{\pi a}}{2tW} F\left(a/W\right) \tag{B-20}$$

With

$$F\left(\frac{a}{W}\right) = \sqrt{\sec\left(\frac{\pi a}{2W}\right)}\left[1 - 0.025\left(\frac{a}{W}\right)^2 + 0.06\left(\frac{a}{W}\right)^4\right] \tag{B-21}$$

Equation Eq. (B-21) can be plotted as function of the crack length over width ratio which is given in Figure B-2. Since the geometry factor is plotted versus the crack over width ratio, this graph is identical for all W.

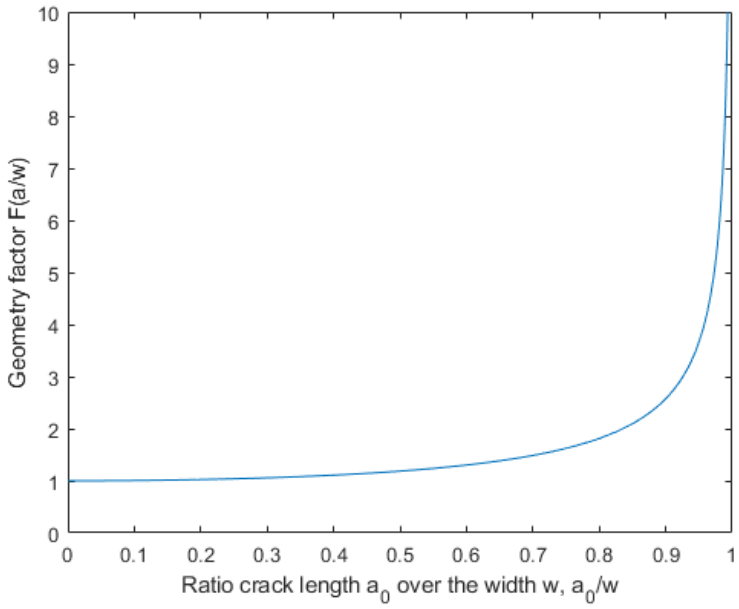


**Figure B-2:** Geometry factor $F(\frac{a}{W})$ as function of the crack over width $(a/W)$

The geometry factors for the specimen used in this research are given in Table B-2.

**Table B-2:** Geometry corrections factor for CCT specimens and the dimensions used for testing as defined in Chapter 4

| Width $(2W)$ | Crack length $(2a_0)$ | Ratio $a/W$ | $F(a/W)$ |
|---|---|---|---|
| 120 | 30 | 0.25 | 1.039 |
| 120 | 40 | 0.33 | 1.072 |
| 120 | 50 | 0.42 | 1.12 |
| 288 | 96 | 0.33 | 1.072 |
| 900 | 200 | 0.22 | 1.031 |
| 900 | 250 | 0.28 | 1.049 |
| 900 | 300 | 0.33 | 1.072 |
| 900 | 350 | 0.39 | 1.10 |
| 900 | 400 | 0.44 | 1.14 |

## B.4 Fracture mechanics test results

In the following subsections, the results from the DIC analysis for each test sample is shown.

### Results small scale fracture tests

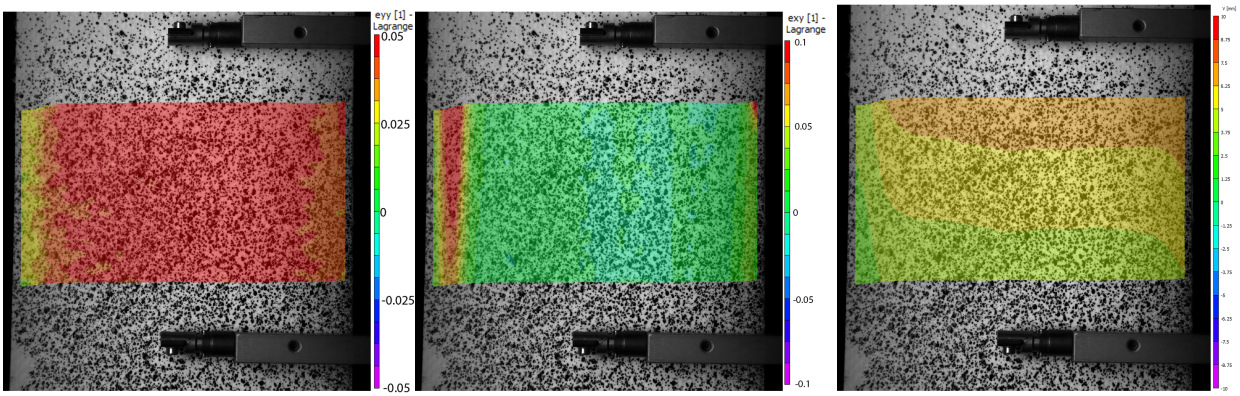


**(a)** Tensile strain in y-direction $\epsilon_y$ **(b)** Shear strain in y-direction $\epsilon_{xy}$ **(c)** Displacement y-direction $V$

**Figure B-3:** DIC strain and displacement analysis of sample Small T01. No initial crack is present. Images are captured just before failure.

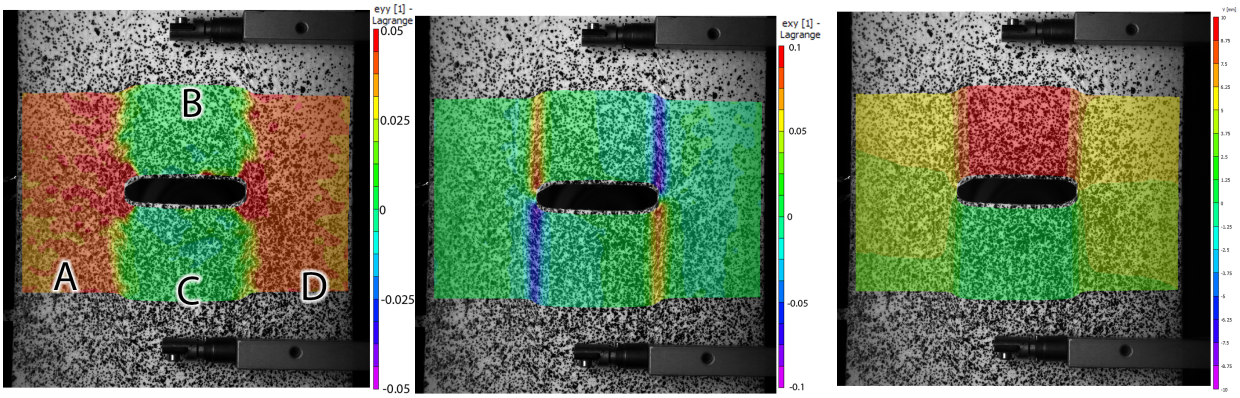


**(a)** Tensile strain in y-direction $\epsilon_y$ **(b)** Shear strain in y-direction $\epsilon_{xy}$ **(c)** Displacement y-direction $V$

**Figure B-4:** DIC strain and displacement analysis of sample S01. Initial crack length is 40 mm. Images are captured just before failure.

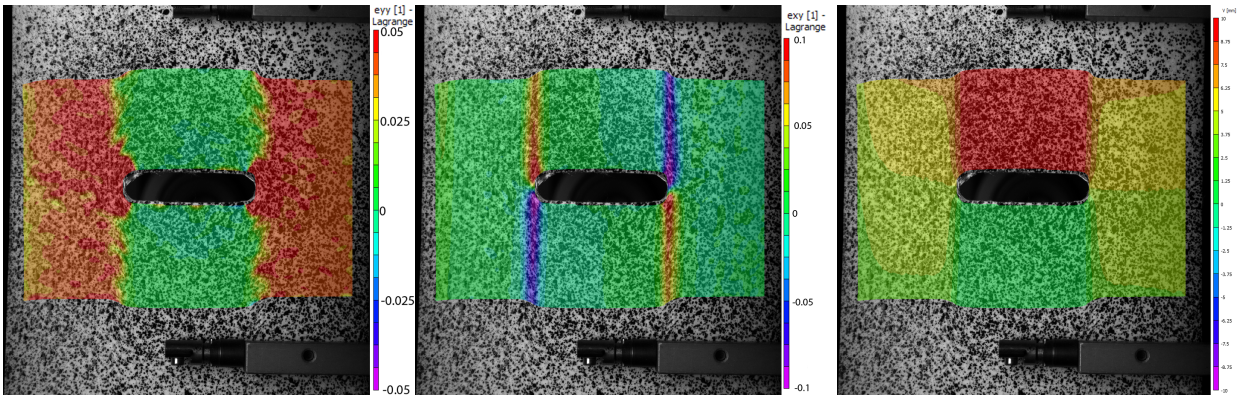


**(a)** Tensile strain in y-direction $\epsilon_y$ **(b)** Shear strain in y-direction $\epsilon_{xy}$ **(c)** Displacement y-direction $V$

**Figure B-5:** DIC strain and displacement analysis of sample S03. Initial crack length is 40 mm. Images are captured just before failure.

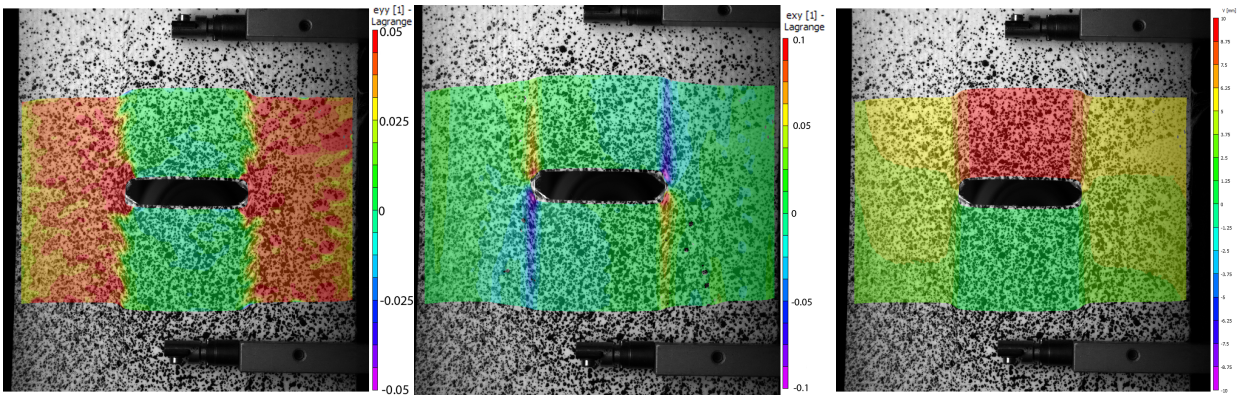


**(a)** Tensile strain in y-direction $\epsilon_y$ **(b)** Shear strain in y-direction $\epsilon_{xy}$ **(c)** Displacement y-direction $V$

**Figure B-6:** DIC strain and displacement analysis of sample S04. Initial crack length is 40 mm. Images are captured just before failure.

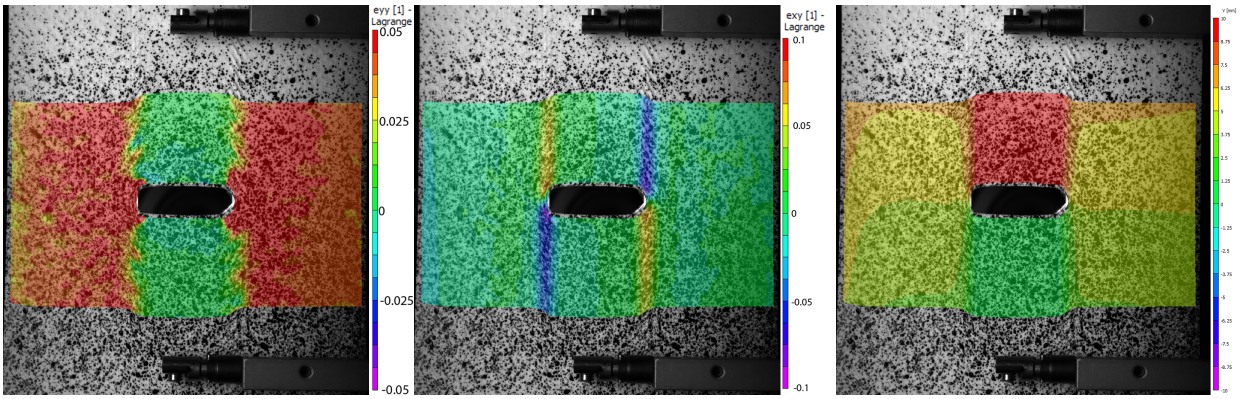


**(a)** Tensile strain in y-direction $\epsilon_y$ **(b)** Shear strain in y-direction $\epsilon_{xy}$ **(c)** Displacement y-direction $V$

**Figure B-7:** DIC strain and displacement analysis of sample S05. Initial crack length is 30 mm. Images are captured just before failure.

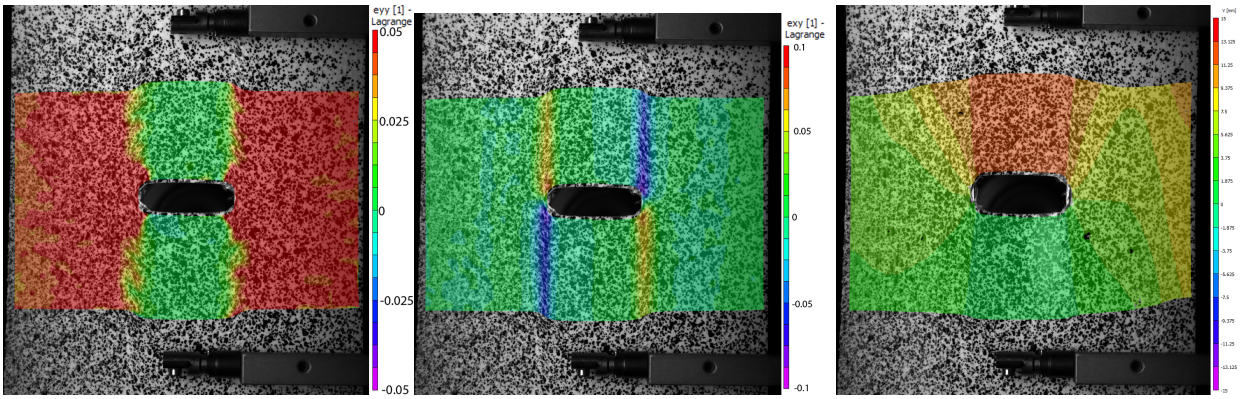


**(a)** Tensile strain in y-direction $\epsilon_y$ **(b)** Shear strain in y-direction $\epsilon_{xy}$ **(c)** Displacement y-direction $V$

**Figure B-8:** DIC strain and displacement analysis of sample S06. Initial crack length is 30 mm. Images are captured just before failure.

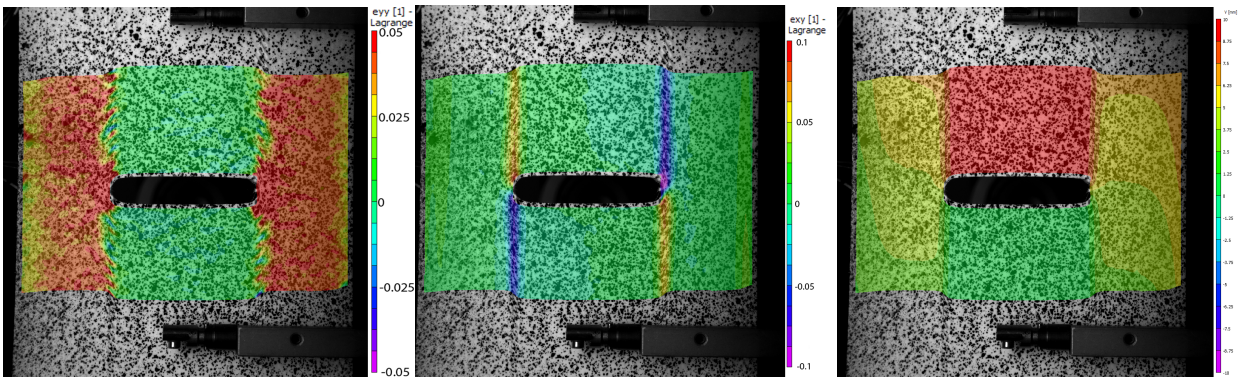


**(a)** Tensile strain in y-direction $\epsilon_y$ **(b)** Shear strain in y-direction $\epsilon_{xy}$ **(c)** Displacement y-direction $V$

**Figure B-9:** DIC strain and displacement analysis of sample S07. Initial crack length is 30 mm. Images are captured just before failure.

### Results medium scale fracture tests

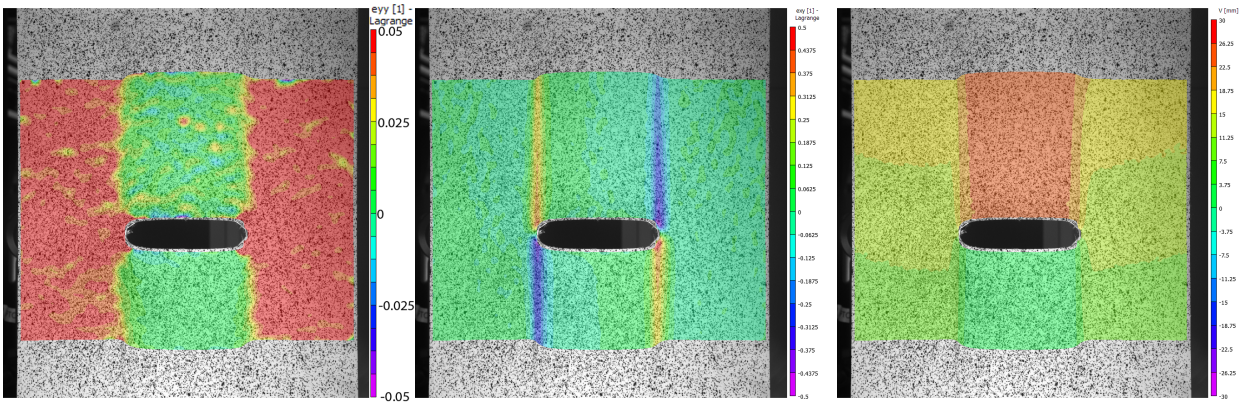


**(a)** Tensile strain in y-direction $\epsilon_y$ **(b)** Shear strain in y-direction $\epsilon_{xy}$ **(c)** Displacement y-direction $V$

**Figure B-10:** DIC strain and displacement analysis of sample M03. Initial crack length is 96 mm. Images are captured just before failure.

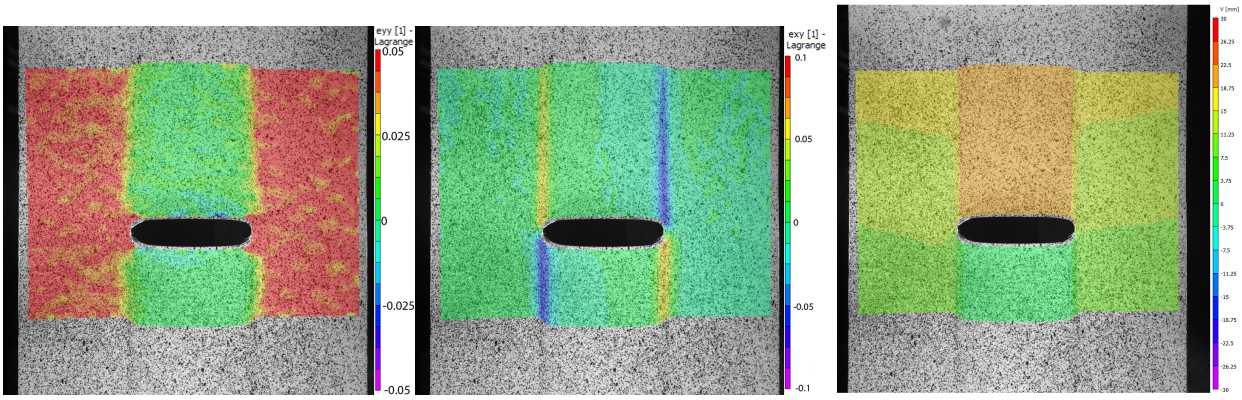


**(a)** Tensile strain in y-direction $\epsilon_y$ **(b)** Shear strain in y-direction $\epsilon_{xy}$ **(c)** Displacement y-direction $V$

**Figure B-11:** DIC strain and displacement analysis of sample M05. Initial crack length is 96 mm. Images are captured just before failure.

### Results large scale fracture tests

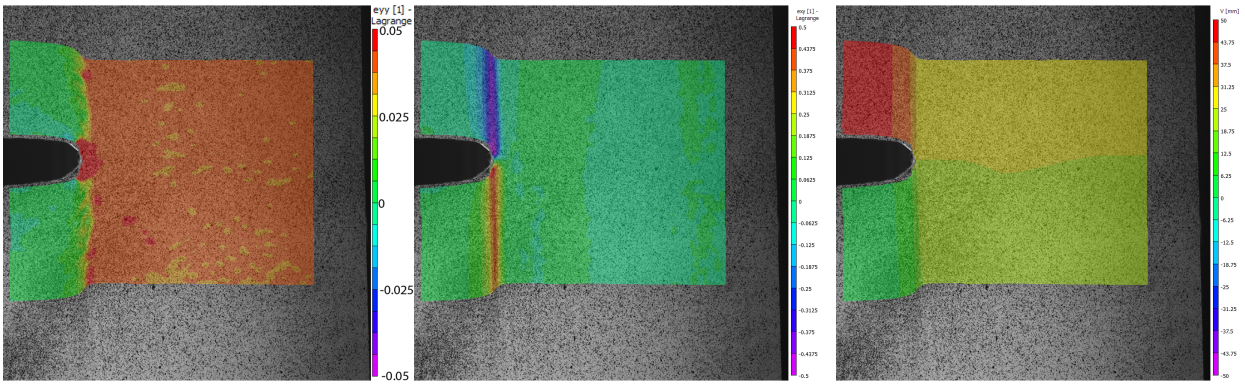


**(a)** Tensile strain in y-direction $\epsilon_y$ **(b)** Shear strain in y-direction $\epsilon_{xy}$ **(c)** Displacement y-direction $V$

**Figure B-12:** DIC strain and displacement analysis of sample L02. Initial crack length is 300 mm. Images are captured just before failure.

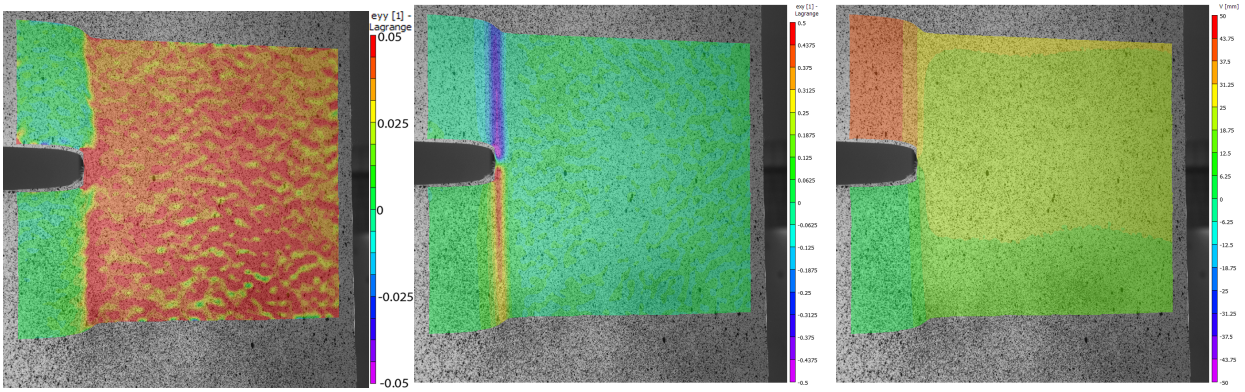


**(a)** Tensile strain in y-direction $\epsilon_y$ **(b)** Shear strain in y-direction $\epsilon_{xy}$ **(c)** Displacement y-direction $V$

**Figure B-13:** DIC strain and displacement analysis of sample L03. Initial crack length is 300 mm. Images are captured just before failure.

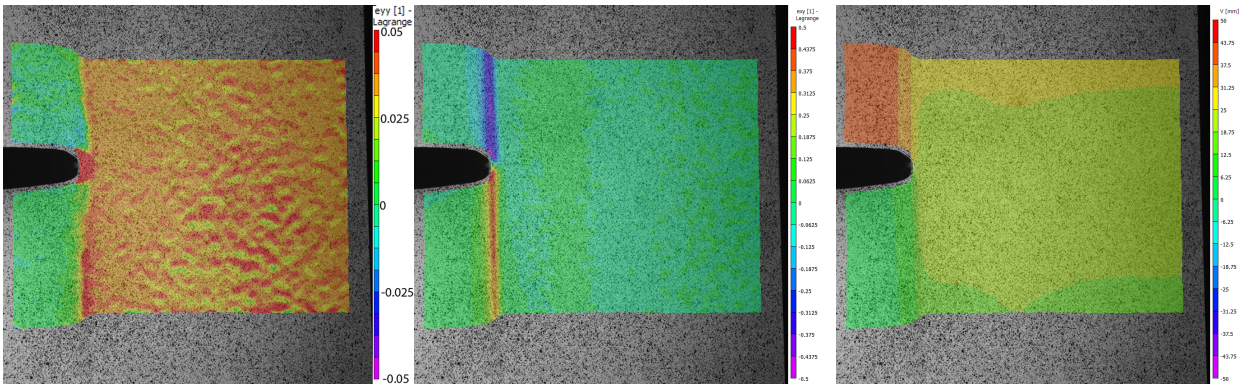


**(a)** Tensile strain in y-direction $\epsilon_y$ **(b)** Shear strain in y-direction $\epsilon_{xy}$ **(c)** Displacement y-direction $V$

**Figure B-14:** DIC strain and displacement analysis of sample L04. Initial crack length is 300 mm. Images are captured just before failure.

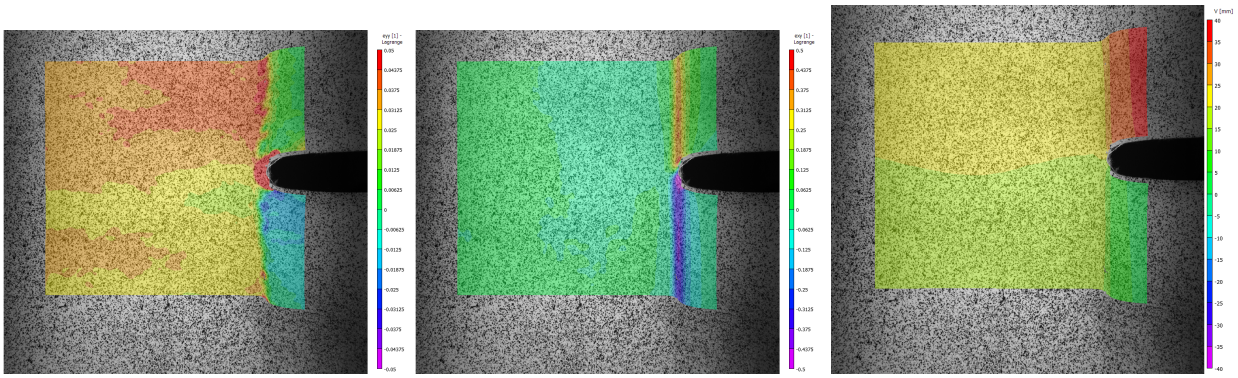

**(a)** Tensile strain in y-direction $\epsilon_y$ **(b)** Shear strain in y-direction $\epsilon_{xy}$ **(c)** Displacement y-direction $V$

**Figure B-15:** DIC strain and displacement analysis of sample L05. Initial crack length is 200 mm. Images are captured just before failure.

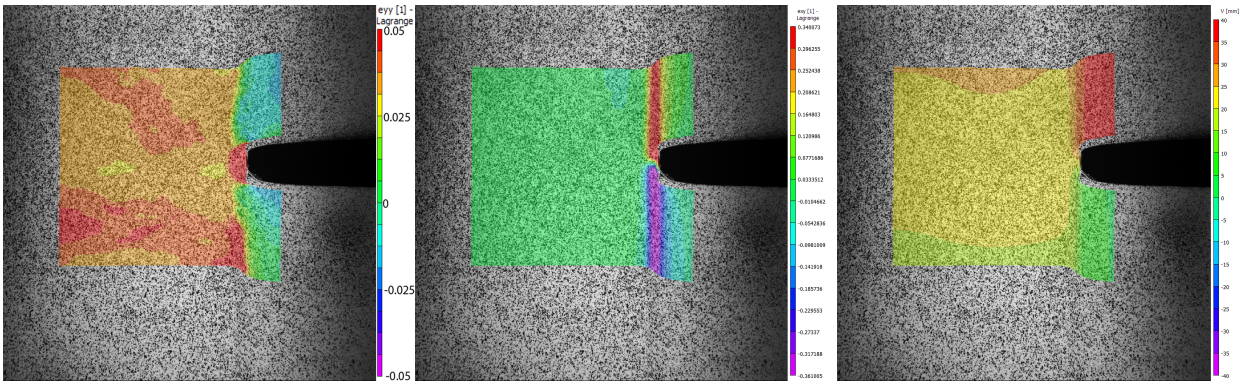


**(a)** Tensile strain in y-direction $\epsilon_y$ **(b)** Shear strain in y-direction $\epsilon_{xy}$ **(c)** Displacement y-direction $V$

**Figure B-16:** DIC strain and displacement analysis of sample L06. Initial crack length is 250 mm. Images are captured just before failure.

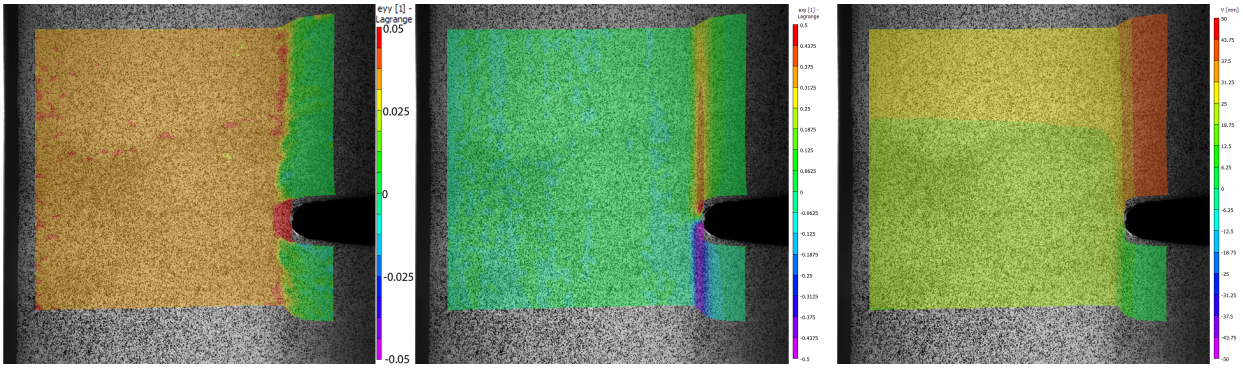


**(a)** Tensile strain in y-direction $\epsilon_y$ **(b)** Shear strain in y-direction $\epsilon_{xy}$ **(c)** Displacement y-direction $V$

**Figure B-17:** DIC strain and displacement analysis of sample L01. Initial crack length is 350 mm. Images are captured just before failure.

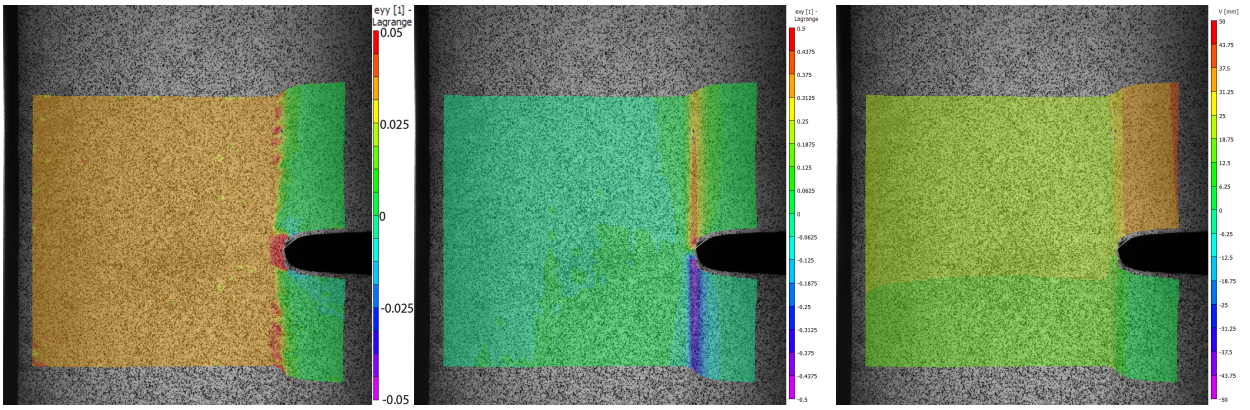


**(a)** Tensile strain in y-direction $\epsilon_y$ **(b)** Shear strain in y-direction $\epsilon_{xy}$ **(c)** Displacement y-direction $V$

**Figure B-18:** DIC strain and displacement analysis of sample L01. Initial crack length is 400 mm. Images are captured just before failure.

# Appendix C

# Peridynamics

Since peridynamics is a relative new method first introduced by Silling[31], the theory and mathematical foundation is summarized in this Appendix. For the complete overview of derivations and laws within the peridynamics (PD) theory, see Madenci et al.[34]. Furthermore Several papers have been published in which the PD theory is applied to model both the static and dynamic fracture of composite laminates (Kilic et al., Oterkus et al., Ghajari et al.[32, 51, 52]). Theoretical background of the PD theory is given in Section C.1 Section C.2 contains an example matlab code used in this research to model the damage progression of the Dyneema® fibers.

## C.1 PD theory

### C.1.1 Peridynamics Equation of motion en kinematics of a material point

The main equation of motion for a material point in the bond-based peridynamics theory is written as:

$$\rho(\mathbf{x})\ddot{\mathbf{u}}(\mathbf{x},t) = \int_{\mathcal{H}_\mathbf{x}} \mathbf{f}\left(\mathbf{u}'-\mathbf{u},\mathbf{x}'-\mathbf{x},t\right) d\mathcal{H}_\mathbf{x} + \mathbf{b}(\mathbf{x},t) \tag{C-1}$$

In which, $\rho(\mathbf{x})$ is the density of the material point at position $\mathbf{x}$ and $\ddot{\mathbf{u}}(\mathbf{x},t)$ it's acceleration at time $t$. $\mathbf{f}\left(\mathbf{u}'-\mathbf{u},\mathbf{x}'-\mathbf{x},t\right)$ is the interaction force of material point $\mathbf{x}$, which is integrated over all material points of $\mathbf{x}$ within its domain $\mathcal{H}_\mathbf{x}$. $\mathbf{b}(\mathbf{x},t)$ is the external body force vector.

Figure C-1 show a body $\mathcal{R}$ in original and deformed configuration, in which two material points are marked. Each material interacts with all material points within its neighborhood $\mathcal{H}_\mathbf{x}$defined by the horizon $\delta$. The original locations of the material point are defined by position vector $\xi$ and $\xi'$. The relative position vector between the two material points is defined by $\boldsymbol{\xi} = |\mathbf{x}'-\mathbf{x}|$. When the body deforms, the material points will deform into the situation at the right side of Figure C-1. Material points $\mathbf{x}$ and $\mathbf{x}'$ will be translated by displacements $\mathbf{u}$ and $\mathbf{u}'$ into the new position given by vectors $\mathbf{y}$ and $\mathbf{y}'$. The relative displacement vector is denoted by $\boldsymbol{\eta} = \mathbf{u}'-\mathbf{u}$. The new relative position vector between the material points is denoted as $\boldsymbol{\xi}+\boldsymbol{\eta} = \mathbf{y}'-\mathbf{y} = (\mathbf{x}'+\mathbf{u}')-(\mathbf{x}+\mathbf{u})$.

For an elastic isotropic body, interaction force $\mathbf{f}$ is defined as a function of the relative position vector $\boldsymbol{\xi}$ and relative displacement vector $\boldsymbol{\eta}$ contained within the total stretch function $\bar{s}$ and is written as:

$$\mathbf{f} = c \cdot \bar{s} \cdot \frac{\mathbf{y}'-\mathbf{y}}{|\mathbf{y}'-\mathbf{y}|} \tag{C-2}$$

In which $c$ is the PD material parameter and $\bar{s}$ the total stretch defined as the sum of the mechanical stretch $s$ and thermal stretch $s*$: $\bar{s} = s + s*$. Thermal effects are ignored in this research, and therefore the total stretch is a function of the mechanical stretch only and defined as:

$$s = \frac{|\boldsymbol{\xi}+\boldsymbol{\eta}|-|\boldsymbol{\eta}|}{|\boldsymbol{\eta}|} = \frac{|\mathbf{y}'-\mathbf{y}|-|\mathbf{x}'-\mathbf{x}|}{|\mathbf{x}'-\mathbf{x}|} \tag{C-3}$$

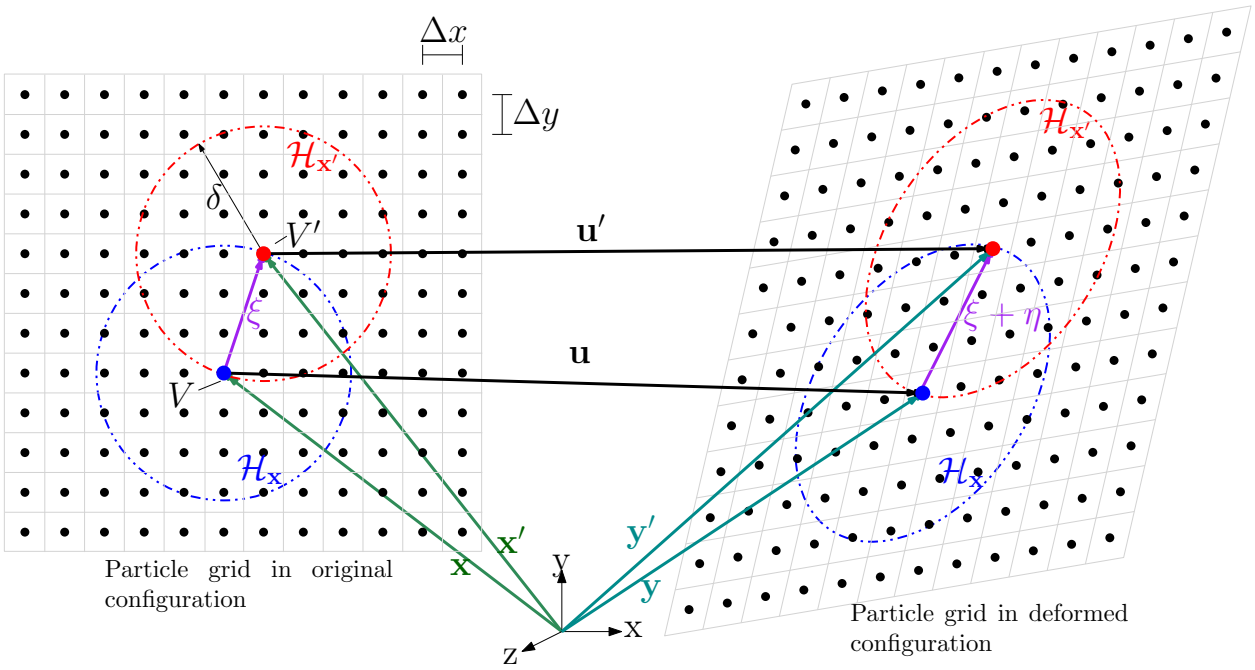


**Figure C-1:** Kinematics between material points

### C.1.2 Strain energy density

Let $\mathbf{x}_k$ and $\mathbf{x}_j$ denote two material points within body $\mathcal{R}$ . A scalar valued micro-potential develops due to the interaction between material point, denoted by $w_{kj}$. $w_{kj}$ depends on the material properties and the stretch of $\mathbf{x}_k$ with all other material points within $\mathcal{H}_{x_k}$. The strain energy density $W_k$ of point k, is written as

$$U_{PD_k} = \frac{1}{2}\int_{\mathcal{H}_{x_k}} w_{kj}\, d\mathcal{H}_{x_k} \tag{C-4}$$

and the micro-potential is defined as:

$$w_{kj} = \frac{1}{2} c s^2 \boldsymbol{\xi}_{kj} \tag{C-5}$$

Strain energy density equation is used by Madenci et al.[34] to derive material properties and surface correction factors. The equation is:

$$W = \frac{1}{2}\sigma_{11}\epsilon_{11} + \frac{1}{2}\sigma_{22}\epsilon_2 + \frac{1}{2}\sigma_{12}\gamma_{11} \tag{C-6}$$

$$= \frac{1}{2}(\mathcal{Q}_{11}\epsilon_{11}^2 + 2\mathcal{Q}_{12}\epsilon_{11}\epsilon_{22} + \mathcal{Q}_{66}\gamma_{12}^2 + \mathcal{Q}_{22}\epsilon_{22}^2) \tag{C-7}$$

### C.1.3 Material parameters

$$b_F = \frac{(\mathcal{Q}_{11} - \mathcal{Q}_{12} - 2\mathcal{Q}_{66})}{2\delta\left(\sum_{j=1}^{N}\left|\mathbf{x}_j^n - \mathbf{x}_i^n\right|\mathcal{V}_j^n\right)} \tag{C-8a}$$

$$b_T = \frac{(\mathcal{Q}_{22} - \mathcal{Q}_{12} - 2\mathcal{Q}_{66})}{2\delta\left(\sum_{j=1}^{N}\left|\mathbf{x}_j^n - \mathbf{x}_i^n\right|\mathcal{V}_j^n\right)} \tag{C-8b}$$

$$b_{FT} = \frac{6\mathcal{Q}_{66}}{\pi t \delta^3} \tag{C-8c}$$

Within bond based peridynamics, the dilation term $a$ and the transverse bond force $b_T$ disappear when the UD ply is modeled, due to the assumptions that $\mathcal{Q}_{12} = \mathcal{Q}_{16}$ and $\mathcal{Q}_{22} = 3\mathcal{Q}_{12}$[36]. However, letting $b_T$ disappear will let the simulation loose the transverse fiber direction properties, which is in this research required to simulate the fibers in weft direction.

### C.1.4 Surface correction factors

Surface correction factors are required to compensate for the loss of stiffness at boundary particles due the decrease in amount of bond-force vectors near edges Madenci et al.[34]. The difference is shown in Figure C-2. This decrease in stiffness Surface correction factors are determined by comparing the strain energy density of the classical continuum mechanics at particle $i$, $W_\alpha^{CM}(\mathbf{x}_i^n)$, with the strain energy density of the peridynamic bond $W_\alpha^{PD}(\mathbf{x}_i^n)$.

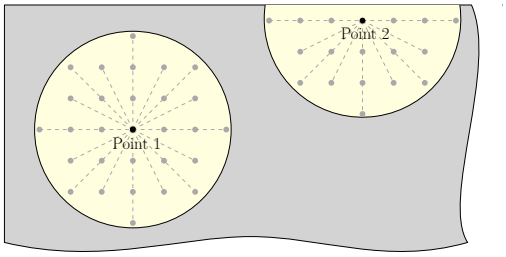


**Figure C-2:** Surface effects. Source: Madenci et al.[34]

The set of equations to determine the surface correction factors are given in longitudinal direction are given in Eq. (C-9a) till Eq. (C-9a)

Set of equation to determine the surface correction factors in longitudinal direction:

$$S_{1F_i} = \frac{W_{1F}^{CM}(\mathbf{x}_i^n)}{W_{1F}^{PD}(\mathbf{x}_i^n)} = \frac{\frac{1}{2}\left(\mathcal{Q}_{11} - \mathcal{Q}_{12} - 2\mathcal{Q}_{66}\right)\zeta^2}{b_F\delta\sum_{j=1}^{M}\frac{1}{\left|\mathbf{x}_j^n - \mathbf{x}_i^n\right|}\left(\left|\mathbf{y}_j^n - \mathbf{y}_i^n\right| - \left|\mathbf{x}_j^n - \mathbf{x}_i^n\right|\right)^2\mathcal{V}_j^n} \tag{C-9a}$$

$$S_{1T_i} = 1 \tag{C-9b}$$

$$S_{1FT_i} = \frac{W_{1FT}^{CM}(\mathbf{x}_i^n)}{W_{1FT}^{PD}(\mathbf{x}_i^n)} = \frac{\frac{3}{2}\mathcal{Q}_{66}\zeta^2}{b_{FT}\delta\sum_{j=1}^{P}\frac{1}{\left|\mathbf{x}_j^n - \mathbf{x}_i^n\right|}\left(\left|\mathbf{y}_j^n - \mathbf{y}_i^n\right| - \left|\mathbf{x}_j^n - \mathbf{x}_i^n\right|\right)^2\mathcal{V}_j^n} \tag{C-9c}$$

Set of equations to determine the surface correction factors in transverse direction:

$$S_{2F_i} = 1 \tag{C-10a}$$

$$S_{2T_i} = \frac{W_{2T}^{CM}(\mathbf{x}_i^n)}{W_{2T}^{PD}(\mathbf{x}_i^n)} = \frac{\frac{1}{2}\left(\mathcal{Q}_{11} - \mathcal{Q}_{12} - 2\mathcal{Q}_{66}\right)\zeta^2}{b_T\delta\sum_{j=1}^{M}\frac{1}{\left|\mathbf{x}_j^n - \mathbf{x}_i^n\right|}\left(\left|\mathbf{y}_j^n - \mathbf{y}_i^n\right| - \left|\mathbf{x}_j^n - \mathbf{x}_i^n\right|\right)^2\mathcal{V}_j^n} \tag{C-10b}$$

$$S_{2FT_i} = \frac{W_{2FT}^{CM}(\mathbf{x}_i^n)}{W_{2FT}^{PD}(\mathbf{x}_i^n)} = \frac{\frac{3}{2}\mathcal{Q}_{66}\zeta^2}{b_{FT}\delta\sum_{j=1}^{P}\frac{1}{\left|\mathbf{x}_j^n - \mathbf{x}_i^n\right|}\left(\left|\mathbf{y}_j^n - \mathbf{y}_i^n\right| - \left|\mathbf{x}_j^n - \mathbf{x}_i^n\right|\right)^2\mathcal{V}_j^n} \tag{C-10c}$$

### C.1.5 Volume correction procedure

The entire volume of each material point $\mathbf{x}'$ is considered while integrating over horizon $\mathcal{H}_{\mathbf{x}}$ of material point $\mathbf{x}$. As shown in Figure C-3, when cubic subdomains are used and a horizon of $\delta = 3\Delta$, $r = {}^{\Delta}/_{2}$, the calculation can be improved by multiplying the integral equation with the volume correction factor $v_c$. This factor is applied to the collocation points that lie within the region $\delta - r < \eta_{ij} < \delta$, as can be seen in Figure C-3

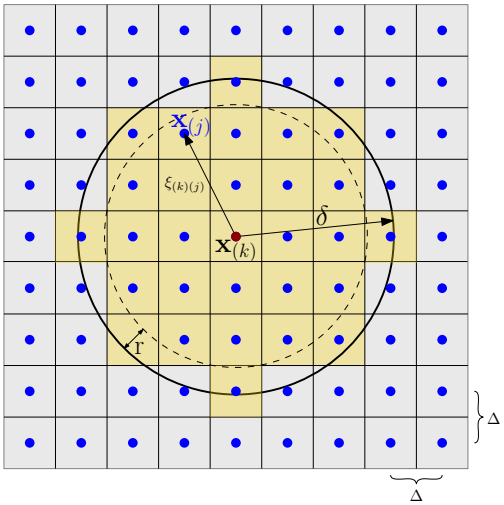


**Figure C-3:** Volume correction. Source: Madenci et al.[34]

$$\begin{cases} v_c = \dfrac{(\delta + r - \boldsymbol{\xi})}{2r} & \text{for } \delta - r < \boldsymbol{\xi} < \delta \\ v_c = 1 & \text{for } \boldsymbol{\xi} < \delta - r \\ v_c = 0 & \text{otherwise} \end{cases} \tag{C-11}$$

With $v_c$ denoting the volume correction factor.

The discretized form of the equation of motion than becomes:

$$\rho(\mathbf{x}_i)\ddot{\mathbf{x}}(\mathbf{x}_i, t) = \sum_{e=1}^{N}[\mathbf{t}(\mathbf{u}(\mathbf{x}_j, t) - \mathbf{u}(\mathbf{x}_i, t), \mathbf{x}_j - \mathbf{x}_i) - \mathbf{t}(\mathbf{u}(\mathbf{x}_i, t) - \mathbf{u}(\mathbf{x}_j, t), \mathbf{x}_i - \mathbf{x}_j)](v_{c_i} V_i) + \mathbf{b}(\mathbf{x}_i, t) \tag{C-12}$$

## C.2 Peridynamic Matlab Code

```
1  %%%  MSC THESIS - FACULTY OF AEROSPACE ENGINEERING
2  %    Fracture thougness of a Dyneema cloth
3  %
4  %    BJE van Rodijnen
5  %
6  %    Code based on the example codes of Madenci, Oterkus
7  %    "Peridynamic Theory and its Applications"
8  %
9  %    Conditions:
10 %    Boundary conditions:    Displacement Controlled, velocity applied in x-
       direction
11 %    Material properties:    Bt, Bf, Bft
```

```
12 % Failure included
13 %
14 %% Input
15 % Number of particles in the x-direction
16 clc;
17 clear all;
18 close all;
19 tic
20
21 %%% Geometry & physical properties
22 w   = 0.180;                % [m]       Lamina width
23 h   = 0.120;                % [m]       Lamina height
24 t   = 0.71E-3;              % [m]       Lamina thickness
25 hw  = w/h;                  % [-]       Ration width over height
26 Acr = t*h;                  % [m^2]     Cross-sectional area
27 rho = 890;                  % [kg/m^2]  Density of the plie
28
29 % Initial crack length
30 crack = 0.04;               % [m]       Initial crack length
31
32 % Material properties
33 E11  = 8.62E9;              % [Pa]      Young's modulus direction 11
34 E22  = 0.123E9;             % [Pa]      Young's modulus direction 22
35 E222 = 5.07E9;
36 G12  = 0.0124E9;            % [Pa]      Shear modulus direction 12
37 nu12 = 1/3;                 % [-]       Possions ratio direction 12
38 nu211 = nu12 * E22/E11 ;    % [-]       Poissons ration direction 21
39 nu212 = nu12 * E222/E11 ; % [-]       Poissons ration direction 21
40 epstrans = 0.08;      % [-]     Transition strain in weft direction
41
42 % Material Failure properties
43 Xt = 330E6;                 % [Pa]       Ultimate tensile stress in warp dir.
44 Yt = 229E6;                 % [Pa]       Ultimate tensile stress in weft dir.
45 S  = 5.6E6;                 % [Pa]       Ultimate shear stress
46
47 % Stiffness Matrix
48 Q11  = E11 / (1 - nu12*nu211);
49 Q22  = E22 / (1 - nu12*nu211);
50 Q12  = (nu12*E22) / (1- nu12 * nu211);
51 Q66  = G12;
52 Q112 = E11 / (1 - nu12*nu212);
53 Q222 = E222 / (1 - nu12*nu212);
54 Q122 = (nu12*E222) / (1- nu12 * nu212);
55
56 % Aligning stiffness properties with correct axis
57 theta = 0.0*pi/180;
58 m = cos(theta);
59 n = sin(theta);
60
61 Qxx  = Q11*m^4     + Q22*n^4     + 2*Q12*m^2*n^2 + 4*Q66*m^2*n^2;
62 Qyy  = Q11*n^4     + Q22*m^4     + 2*Q12*m^2*n^2 + 4*Q66*m^2*n^2;
63 Qxy  = m^2*n^2*Q11 + m^2*n^2*Q22 + (m^4+n^4)*Q12 - 4*m^2*n^2*Q66;
64 Qss  = m^2*n^2*Q11 + m^2*n^2*Q22 - 2*m^2*n^2*Q12 + (m^2 - n^2)^2 * Q66;
65
66 Qxx2 = Q112*m^4    + Q222*n^4     + 2*Q122*m^2*n^2 + 4*Q66*m^2*n^2;
67 Qyy2  = Q112*n^4    + Q222*m^4     + 2*Q122*m^2*n^2 + 4*Q66*m^2*n^2;
68 Qxy2  = m^2*n^2*Q11 + m^2*n^2*Q222 + (m^4+n^4)*Q122 - 4*m^2*n^2*Q66;
```

```
69  Qss2  = m^2*n^2*Q11 + m^2*n^2*Q222 - 2*m^2*n^2*Q122 + (m^2 - n^2)^2 * Q66;
70
71  %%% Discretization parameters
72  numx   = 150;              % Number of Material point in the x-direction
73  numy   = numx/hw ;         % Number of Material point in the y-direction
74  numbnd = 3;                % Number of Material point in th boundary region
75  dx     = w / numx;         % Material point spacing in x-direction
76  dy     = h / numy;         % Material point spacing in y-direction
77  nnum   = 0;                % Current node number
78
79  numnodes    = (numx + 2*numbnd)* numy;  % Total number of nodes
80  maxfam      = 100;         % Allowed maximum number of
81
82  area  = dx * dy;           % Area of the particle
83  vol   = area * t;          % Volume of a material point
84  radij = dx/2;              % Node radius
85  delta = 3.015*dx;          % Horizon distance
86
87  %%% Peridynamic material parameters
88  % Material bond-force constant in warp
89  Bx  = 2 * 29/4 * (Qxx - Qxy - 2* Qss) / (pi * t * delta^3);
90  % Material bond-force constant in weft direction
91  By1 = 2 * 29/4 * (Qyy - Qxy - 2* Qss) / (pi * t * delta^3);
92  By2 = 2 * 29/4 * (Qyy2 - Qxy2 - 2* Qss) / (pi * t * delta^3);
93  % Material bond-force constant in any other direction
94  Bxy = 24 * Qss / (pi * t * delta^3);
95
96  % Failure stretch
97  scr11   = Xt/E11;                % [-] Critical stretch warp direction
98  scr22   = Yt/E222+0.08;          % [-] Critical stretch weft direction
99  scr12   = S/G12;           % [-] Critical stretch shear direction
100 failure = ones(numnodes,maxfam); % Matrix containing all failure bonds
101 dmg     = zeros(numnodes,1);     % Damage factor
102 maxdmg  = 0.5;
103 maxxc   = crack/2;
104
105 % Strain energy density references from classical continuum mechanics
106 zeta = 0.001;   % Initial displacement factor
107 % References for the first loading in y-direction
108 Wcm1F  = 0.5 * (Qxx - Qxy - 2*Qss) * zeta^2 ;
109 Wcm1T  = 0;
110 Wcm1FT = (3/2) * Qss * zeta^2 ;
111 % References for the second loading in x-direction
112 Wcm2F  = 0;
113 Wcm2T  = 0.5 * (Qyy - Qxy - 2*Qss) * zeta^2;
114 Wcm2FT = (3/2) * Qss * zeta^2;
115 % Surface correction factors components
116 scfx  = 0.0;
117 scfy  = 0.0;
118 scfr  = 0.0;
119 scmx  = 0.0;
120 scmy  = 0.0;
121 scmr  = 0.0;
122 WpdF  = zeros(numnodes,2);
123 WpdFT = zeros(numnodes,2);
124 Sf    = zeros(numnodes,2);
125 Sm    = zeros(numnodes,2);
```

```
126 Sfold = zeros(numnodes,2);
127 Smold = zeros(numnodes,2);
128
129 %%% Boundary conditions
130 Vxnbd = 2;          % Velocity boundary condition at the boudnary regions
131 %%% Time variables
132 numt = 8500;                                        % Number of time steps
133 dt   = 0.8*sqrt(2.0*rho*dx/(pi*delta^2*dx*Bx));  % Time step size
134
135 %%% System matrices and variables
136 % Location and displacement matrices
137 Xv          = zeros(numnodes,2);    % Original position vector
138 Yv          = zeros(numnodes,2);    % Displacement vector
139 Vel         = zeros(numnodes,2);    % Velocity vector
140 Acc         = zeros(numnodes,2);    % Acceleration vector
141
142 numfam      = zeros(numnodes,1);
143 pointfam    = zeros(numnodes,1);    % Family of nodes within horizon of a
        material particle
144 nodefam     = zeros(1000000,1);
145
146 curnode     = 0;                    % Current node number
147 xi          = 0;                    % Initial distance between points
148 eta         = 0;                    % New distance between points
149
150 %%% Force components
151 dforce1f    = 0.0;              %  x fiber component of the PD force between
        two material points
152 dforce1m    = 0.0;              % x matrix component of the PD force between
        two material points
153 dforce2f    = 0.0;              % y fiber component of the PD force between
        two material points
154 dforce2m    = 0.0;              % y matrix component of the PD force between
        two material points
155 pforce      = zeros(numnodes,2); % Peridynamic force in x and y direction
156 pforceold   = zeros(numnodes,2); %
157 bforce      = zeros(numnodes,2); % External body forces
158
159 dispnode38400   = zeros(numt,2);
160 enddisp     = zeros(numt,1);
161 endtime     = zeros(numt,1);
162 fplane1     = zeros(numt,1);
163 fplane2     = zeros(numt,1);
164 fplane1t    = zeros(numt,1);
165 fplane2t    = zeros(numt,1);
166
167 % Video frame counter
168 vi = 1;
169 completefailure = 0;
170
171 %% Discretization
172 %Material points of the lamina
173 % Internal region
174 for j = 1:numx
175     for k = 1:numy
176         nnum = nnum + 1;
177         Xv(nnum,1) = (-1.0 * w / 2.0) + (dx / 2.0) + (j-1) * dx;
```

```
178         Xv(nnum,2) = (-1.0 * h / 2.0) + (dy / 2.0) + (k-1) * dy;
179     end
180 end
181 numint = nnum;  % Total number of nodes in the internal lamina region
182
183 % Boundary region left side
184 for j = 1:numbnd
185     for k = 1:numy
186         nnum = nnum + 1;
187         Xv(nnum,1) = (-1.0 * w / 2.0) - (dx / 2.0) - (j-1) * dx;
188         Xv(nnum,2) = (-1.0 * h / 2.0) + (dy / 2.0) + (k-1) * dy;
189     end
190 end
191 numleft = nnum; % Total number of nodes at the left boundary region
192
193 % Boundary region right side
194 for j = 1:numbnd
195     for k = 1:numy
196         nnum = nnum + 1;
197         Xv(nnum,1) = (1.0 * w / 2.0) + (dx / 2.0) + (j-1) * dx;
198         Xv(nnum,2) = (-1.0 * h / 2.0) + (dy / 2.0) + (k-1) * dy;
199     end
200 end
201 numright = nnum; % Total number of nodes at the right boundary region
202
203 %% Assigning bond vectors bewtween material points
204 for j = 1:numnodes
205     if j==1
206         pointfam(j,1) = 1;
207     else
208         pointfam(j,1) = pointfam(j-1,1) + numfam(j-1,1);
209     end
210     for k = 1:numnodes
211         xi = sqrt((Xv(k,1) - Xv(j,1))^2 + (Xv(k,2) - Xv(j,2))^2);
212         if j~=k
213             if xi <= delta
214                 numfam(j,1) = numfam(j,1) + 1;
215                 nodefam(pointfam(j,1)+numfam(j,1)-1,1) = k;
216             end
217         end
218     end
219 end
220
221 %% Definition of the crack surface
222 %PD bonds penetrating through the crack surface are broken
223 for j = 1:numnodes
224     for k = 1:numfam(j,1)
225         cnode = nodefam(pointfam(j,1)+k-1,1);
226         if Xv(cnode,1) > 0.0 && Xv(j,1) < 0.0
227             if abs(Xv(j,2)) - (crack / 2.0) <=  1.0E-10
228         failure(j,k) = 0;
229             elseif abs(Xv(cnode,2)) - (crack / 2.0) <= 1.0E-10
230         failure(j,k) = 0;
231             end
232         elseif Xv(j,1) > 0.0  && Xv(cnode,1) < 0.0
233             if abs(Xv(j,2)) - (crack / 2.0) <= 1.0E-10
234         failure(j,k) = 0;
```

```
235             elseif  abs(Xv(cnode,2)) - (crack / 2.0) <= 1.0E-10
236         failure(j,k) = 0;
237             end
238         end
239     end
240 end
241
242 %% Determination of surface correction factors
243 %loading in x-direction
244 for j = 1:numnodes
245     Yv(j,1) = zeta * Xv(j,1);
246     Yv(j,2) = 0.0;
247 end
248
249 for j = 1:numnodes
250     WpdF(j,1) = 0.0;
251     WpdFT(j,1) = 0.0;
252     for k = 1:numfam(j,1)
253         cnode = nodefam(pointfam(j,1)+k-1,1);
254         xi = sqrt((Xv(cnode,1) - Xv(j,1))^2 + (Xv(cnode,2) - Xv(j,2))^2);
255         eta = sqrt((Xv(cnode,1) + Yv(cnode,1) - Xv(j,1) - Yv(j,1))^2 + (Xv(
              cnode,2) + Yv(cnode,2) - Xv(j,2) - Yv(j,2))^2);
256         if (xi <= delta-radij)
257             fac = 1.0;
258         elseif (xi <= delta+radij)
259             fac = (delta+radij-xi)/(2.0*radij);
260         else
261             fac = 0.0;
262         end
263
264         if abs(Xv(cnode,2) - Xv(j,2)) <= 1.0E-10 % Fibers in x-direction
265             WpdF(j,1)  = WpdF(j,1)  + 0.5 * 0.5 * Bx * ((eta - xi)^2 / xi) *
                    vol * fac;
266             WpdFT(j,1) = WpdFT(j,1) + 0.5 * 0.5 * Bxy * ((eta - xi)^2 / xi) *
                    vol * fac;
267         else
268             WpdFT(j,1) = WpdFT(j,1) + 0.5 * 0.5 * Bxy * ((eta - xi)^2 / xi) *
                    vol * fac;
269         end
270     end
271     Sf(j,1) = Wcm1F / WpdF(j,1);
272     Sm(j,1) = Wcm1FT / WpdFT(j,1);
273 end
274
275 %loading in y-direction
276 for j = 1:numnodes
277     Yv(j,1) = 0.0;
278     Yv(j,2) = zeta * Xv(j,2);
279 end
280
281 for j = 1:numnodes
282     WpdF(j,2) = 0.0;
283     WpdFT(j,2) = 0.0;
284     for k = 1:numfam(j,1)
285         cnode = nodefam(pointfam(j,1)+k-1,1);
286         xi = sqrt((Xv(cnode,1) - Xv(j,1))^2 + (Xv(cnode,2) - Xv(j,2))^2);
```

```
287         eta = sqrt((Xv(cnode,1) + Yv(cnode,1) - Xv(j,1) - Yv(j,1))^2 + (Xv(
                cnode,2) + Yv(cnode,2) - Xv(j,2) - Yv(j,2))^2);
288         if (xi <= delta-radij)
289             fac = 1.0;
290         elseif (xi <= delta+radij)
291             fac = (delta+radij-xi)/(2.0*radij);
292         else
293             fac = 0.0;
294         end
295
296          if (abs(Xv(cnode,1) - Xv(j,1)) <= 1.0E-10) % Fibers in y-direction
297              WpdF(j,2)  = WpdF(j,2)  + 0.5 * 0.5 * By1  * ((eta - xi)^2 / xi)
                     * vol * fac;
298              WpdFT(j,2) = WpdFT(j,2) + 0.5 * 0.5 * Bxy * ((eta - xi)^2 / xi) *
                     vol * fac;
299          else
300             WpdFT(j,2) = WpdFT(j,2) + 0.5 * 0.5 * Bxy * ((eta - xi)^2 / xi)  *
                    vol * fac ;
301          end
302      end
303
304     Sf(j,2) = Wcm2T / WpdF(j,2);
305     Sm(j,2) = Wcm2FT / WpdFT(j,2);
306 end
307
308 %% Boundary conditions
309 % initial displacement
310 for j = 1:numnodes
311         Vel(j,1) = 0.0;
312         Vel(j,2) = 0.0;
313         Yv(j,1) = 0.0;
314         Yv(j,2) = 0.0;
315 end
316
317 %% Time integration
318 for tt = 1:1:numt
319     tt
320     ctime = tt * dt;
321
322     for j = (numint+1):numleft
323         Vel(j,1) = -Vxnbd;
324         Yv(j,1)  = -Vxnbd * tt * dt;
325         Vel(j,2) = 0.0;
326         Yv(j,2)  = 0.0 * tt * dt;
327     end
328 %
329     for j = (numleft+1):numright
330         Vel(j,1) = Vxnbd;
331         Yv(j,1)  = Vxnbd * tt * dt;
332         Vel(j,2) = 0.0;
333         Yv(j,2)  = 0.0 * tt * dt;
334     end
335
336     for j = 1:numnodes
337         dmgpar1 = 0.0;
338         dmgpar2 = 0.0;
339         pforce(j,1) = 0.0;
```

```
340         pforce(j,2) = 0.0;
341
342         for k = 1:numfam(j,1)
343             cnode = nodefam(pointfam(j,1)+k-1,1);
344             xi = sqrt((Xv(cnode,1) - Xv(j,1))^2 + (Xv(cnode,2) - Xv(j,2))^2);
345             eta = sqrt((Xv(cnode,1) + Yv(cnode,1) - Xv(j,1) - Yv(j,1))^2 + (Xv
                    (cnode,2) + Yv(cnode,2) - Xv(j,2) - Yv(j,2))^2);
346             if xi <= (delta-radij)
347                 fac = 1.0;
348             elseif xi <= (delta+radij)
349                 fac = (delta+radij-xi)/(2.0*radij);
350             else
351                 fac = 0.0;
352             end
353             if (abs(Xv(cnode,2) - Xv(j,2)) <= 1.0E-10)
354                 theta = 0.0;
355             elseif (abs(Xv(cnode,1) - Xv(j,1)) <= 1.0E-10)
356                 theta = 90.0 * pi / 180.0;
357             else
358                 theta = atan(abs(Xv(cnode,2) - Xv(j,2)) / abs(Xv(cnode,1) - Xv
                        (j,1)));
359
360             end
361             %Determination of the surface correction between two material
                    points
362             scfx = (Sf(j,1) + Sf(cnode,1)) / 2.0;
363             scfy = (Sf(j,2) + Sf(cnode,2)) / 2.0;
364             if (abs(Xv(cnode,2) - Xv(j,2)) <= 1.0E-10)
365                 scfr = 1.0 / (cos(theta)^2 / (scfx)^2);
366             elseif (abs(Xv(cnode,1) - Xv(j,1)) <= 1.0E-10)
367                 scfr = 1.0 / (sin(theta)^2 / (scfy)^2);
368             else
369                 scfr = 1.0 / (((cos(theta))^2 / (scfx)^2) + ((sin(theta))^2 /
                        (scfy)^2));
370             end
371             scfr = sqrt(scfr);
372             scmx = (Sm(j,1) + Sm(cnode,1)) / 2.0;
373             scmy = (Sm(j,2) + Sm(cnode,2)) / 2.0;
374             scmr = 1.0 / (((cos(theta))^2 / (scmx)^2) + ((sin(theta))^2 / (
                    scmy)^2));
375             scmr = sqrt(scmr);
376             %Peridynamic force calculation for bonds in the fiber direction
377             if (abs(Xv(cnode,2) - Xv(j,2)) <= 1.0E-10)
378                 if failure(j,k) == 1
379                     dforce1f = Bx * (eta - xi) / xi * vol * scfr * fac * (Xv(
                            cnode,1) + Yv(cnode,1) - Xv(j,1) - Yv(j,1)) / eta;
380                     dforce2f = Bx * (eta - xi) / xi * vol * scfr * fac * (Xv(
                            cnode,2) + Yv(cnode,2) - Xv(j,2) - Yv(j,2)) / eta;
381                     dforce1m = Bxy * (eta - xi) / xi * vol * scmr * fac * (Xv(
                            cnode,1) + Yv(cnode,1) - Xv(j,1) - Yv(j,1)) / eta;
382                     dforce2m = Bxy * (eta - xi) / xi * vol * scmr * fac * (Xv(
                            cnode,2) + Yv(cnode,2) - Xv(j,2) - Yv(j,2)) / eta;
383                 else
384                     dforce1f = 0;
385                     dforce2f = 0;
386                 if abs((eta-xi)/xi) < scr12
```

```
387                     dforce1m = Bxy * (eta - xi) / xi * vol * scmr * fac * (Xv(
                            cnode,1) + Yv(cnode,1) - Xv(j,1) - Yv(j,1)) / eta;
388                     dforce2m = Bxy * (eta - xi) / xi * vol * scmr * fac * (Xv(
                            cnode,2) + Yv(cnode,2) - Xv(j,2) - Yv(j,2)) / eta;
389                 else
390                     dforce1m = 0;
391                     dforce2m = 0;
392                 end
393                 end
394
395                 %Calculation of the peridynamic force in x and y directions
396                 %acting on *a material point i due to a material point j
397                 pforce(j,1) = pforce(j,1) + dforce1f + dforce1m ;
398                 pforce(j,2) = pforce(j,2) + dforce2f + dforce2m ;
399
400             elseif (abs(Xv(cnode,1) - Xv(j,1)) <= 1.0E-10)
401                 if failure(j,k) == 1
402                     if abs((eta-xi)/xi) < epstrans
403                         dforce1f = By1 * (eta - xi) / xi * vol * scfr * fac *
                                (Xv(cnode,1) + Yv(cnode,1) - Xv(j,1) - Yv(j,1)) /
                                eta;
404                         dforce2f = By1 * (eta - xi) / xi * vol * scfr * fac *
                                (Xv(cnode,2) + Yv(cnode,2) - Xv(j,2) - Yv(j,2)) /
                                eta;
405                     else
406                         dforce1f = By2 * (eta - xi) / xi * vol * scfr * fac *
                                (Xv(cnode,1) + Yv(cnode,1) - Xv(j,1) - Yv(j,1)) /
                                eta;
407                         dforce2f = By2 * (eta - xi) / xi * vol * scfr * fac *
                                (Xv(cnode,2) + Yv(cnode,2) - Xv(j,2) - Yv(j,2)) /
                                eta;
408                     end
409                         dforce1m = Bxy * (eta - xi) / xi * vol * scmr * fac *
                                (Xv(cnode,1) + Yv(cnode,1) - Xv(j,1) - Yv(j,1)) /
                                eta;
410                         dforce2m = Bxy * (eta - xi) / xi * vol * scmr * fac *
                                (Xv(cnode,2) + Yv(cnode,2) - Xv(j,2) - Yv(j,2)) /
                                eta;
411                 else
412                     dforce1f = 0;
413                     dforce2f = 0;
414                     if abs((eta-xi)/xi) < scr12
415                         dforce1m = Bxy * (eta - xi) / xi * vol * scmr * fac *
                                (Xv(cnode,1) + Yv(cnode,1) - Xv(j,1) - Yv(j,1)) /
                                eta;
416                         dforce2m = Bxy * (eta - xi) / xi * vol * scmr * fac *
                                (Xv(cnode,2) + Yv(cnode,2) - Xv(j,2) - Yv(j,2)) /
                                eta;
417                     else
418                         dforce1m = 0; % Bxy * (eta - xi) / xi * vol * scmr *
                                fac * (Xv(cnode,1) + Yv(cnode,1) - Xv(j,1) - Yv(j
                                ,1)) / eta;
419                         dforce2m = 0; % Bxy * (eta - xi) / xi * vol * scmr *
                                fac * (Xv(cnode,2) + Yv(cnode,2) - Xv(j,2) - Yv(j
                                ,2)) / eta;
420                     end
421                 end
```

```
422
423                 %Calculation of the peridynamic force in x and y directions
424                 %acting on *a material point i due to a material point j
425                 pforce(j,1) = pforce(j,1) + dforce1f + dforce1m ;
426                 pforce(j,2) = pforce(j,2) + dforce2f + dforce2m ;
427
428             else
429                 if failure(j,k) == 1
430                     dforce1m = Bxy * (eta - xi) / xi * vol * scmr * fac * (Xv(
                        cnode,1) + Yv(cnode,1) - Xv(j,1) - Yv(j,1)) / eta;
431                     dforce2m = Bxy * (eta - xi) / xi * vol * scmr * fac * (Xv(
                        cnode,2) + Yv(cnode,2) - Xv(j,2) - Yv(j,2)) / eta;
432                 else
433                     dforce1m = 0; %Bxy * (eta - xi) / xi * vol * scmr * fac *
                        (Xv(cnode,1) + Yv(cnode,1) - Xv(j,1) - Yv(j,1)) / eta;
434                     dforce2m = 0; %Bxy * (eta - xi) / xi * vol * scmr * fac *
                        (Xv(cnode,2) + Yv(cnode,2) - Xv(j,2) - Yv(j,2)) / eta;
435
436                 end
437                 %Calculation of the peridynamic force in x and y directions
438                 %acting on a material point i due to a material point j
439                 pforce(j,1) = pforce(j,1) + dforce1m;
440                 pforce(j,2) = pforce(j,2) + dforce2m;
441             end
442
443             %Determine failure of bonds
444             % Bonds in longitudinal direction
445             if abs(Xv(cnode,2) - Xv(j,2)) <= 1.0E-10
446                 if abs((eta - xi)/xi) >= scr11
447                     %if abs(xi(i,2)) <= (w/4.0)
448                         failure(j,k) = 0;
449                    % end
450                 end
451             % Bonds in transverse direction
452             elseif abs(Xv(cnode,1) - Xv(j,1)) <= 1.0E-10
453                 if abs((eta-xi)/xi) >= scr22
454                     %if abs(xi(i,2)) <= (w/4.0)
455                        failure(j,k) = 0;
456                     %end
457                 end
458             % Bonds in all other directions
459             else
460                 if abs((eta-xi)/xi) >= scr12
461                    % if abs(xi(i,12)) <= (w/4.0)
462                        failure(j,k) = 0;
463                    % end
464                 end
465             end
466
467             dmgpar1 = dmgpar1 + failure(j,k) * vol * fac;
468             dmgpar2 = dmgpar2 + vol * fac  ;
469         end
470
471     dmg(j,1) = 1.0 - dmgpar1 / dmgpar2;
472     if dmg(j,1) >= maxdmg &&  Xv(j,2) >= maxxc
473        maxxc = Xv(j,2);
474     end
```

```
475
476     end
477      newcrlength = maxxc - crack / 2.0;
478
479     % Time integration scheme
480     % Integration over the material points in the internal region
481     for j = 1:1:numint
482        %Calculation of acceleration of material point i
483        Acc(j,1) = (pforce(j,1) + bforce(j,1)) / rho;
484        Acc(j,2) = (pforce(j,2) + bforce(j,2)) / rho;
485        %Calculation of velocity of material point i
486        %by integrating the acceleration of material point i
487        Vel(j,1) = Vel(j,1) + Acc(j,1) * dt;
488        Vel(j,2) = Vel(j,2) + Acc(j,2) * dt;
489        %Calculation of displlacement of material point i
490        %by integrating the velocity of material point i
491        Yv(j,1) = Yv(j,1) + Vel(j,1) * dt;
492        Yv(j,2) = Yv(j,2) + Vel(j,2) * dt;
493     end
494
495     % Intergration over the material points in the elft boundary region
496     for j = numint+1:1:numleft
497        % Integrate acceleration over time.
498        %Calculation of acceleration of material point i
499        Acc(j,2) = 0;%(pforce(i,2) + bforce(i,2)) / rho;
500        %Calculation of velocity of material point i
501        %by integrating the acceleration of material point i
502        Vel(j,2) = 0;%Vel(i,2) + Acc(i,2) * dt;
503        %Calculation of displlacement of material point i
504        %by integrating the velocity of material point i
505        Yv(j,2) = 0;%Yv(i,2) + Vel(i,2) * dt;
506     end
507
508     % Integration over the material point in the right boundary region
509     for j = numleft+1:1:numright
510        % Integrate acceleration over time.
511        %Calculation of acceleration of material point i
512        Acc(j,2) = 0;%(pforce(i,2) + bforce(i,2)) / rho;
513        %Calculation of velocity of material point i
514        %by integrating the acceleration of material point i
515        Vel(j,2) = 0;%Vel(i,2) + Acc(i,2) * dt;
516        %Calculation of displlacement of material point i
517        %by integrating the velocity of material point i
518        Yv(j,2) = 0;%Yv(i,2) + Vel(i,2) * dt;
519     end
520
521     endtime(tt,1) = ctime;
522
523
524     % Make displacement array of the left and right sides to give an
525     % overview of the total stretch of the lamina
526     totalstretch(tt,1) = tt;                % Time step
527     totalstretch(tt,2) = Xv(1,1);           % Bottom left node in internal
           region
528     totalstretch(tt,3) = Yv(1,1);           %
529     totalstretch(tt,4) = Xv(numx,1);        % Bottom right node in internal
           region
```

```
530     totalstretch(tt,5) = Yv(numx,1);          %
531     totalstretch(tt,6) = Xv(numleft,1);       % First Bottom node in left bnd
            region
532     totalstretch(tt,7) = Yv(numleft,1);       %
533     totalstretch(tt,8) = Xv(numright,1);      % First Bottom node in left bnd
            region
534     totalstretch(tt,9) = Yv(numright,1);      %
535     totalstretch(tt,10) = newcrlength;
536
537
538     % Nominal strain of the lamina
539     % Original length between the two points
540     Xvoriginal = sqrt( (Xv(numleft+1,1) - Xv(numint+1,1))^2 + (Xv(numleft+1,2)
            - Xv(numint+1,2))^2);
541     Xvnew      = sqrt( (Xv(numleft+1,1) + Yv(numleft+1,1) - Xv(numint+1,1) -
            Yv(numint+1,1))^2 + (Xv(numleft+1,2) + Yv(numleft+1,2) - Xv(numint
            +1,2) - Yv(numint+1,2))^2);
542     elongationINT(tt) = (Xvnew - Xvoriginal) / Xvoriginal * 100;
543
544     % Point 1: 7451
545     % Point 2: 7551
546     CTODvalue = sqrt((Xv(7551,1) + Yv(7551,1) - Xv(7451,1) - Yv(7451,1))^2
            +...
547         (Xv(7551,2) + Yv(7551,2) - Xv(7451,2) - Yv(7451,2))^2);
548
549     CTOD(tt,:) = [ tt CTODvalue ];
550     cracksize(tt,:) = [ tt newcrlength ];
551     if newcrlength > 0.039 && completefailure == 0
552         failretimestep = tt;
553         completefailure = 1;
554     end
555
556     ctodplottext = CTOD(tt,2)*1000;
557
558     %Writing video file
559     if ~(mod(tt,10))
560         tts = num2str(tt);
561         cts = num2str(ctime);
562         eint = num2str(elongationINT(tt));
563         ctodtext = num2str(ctodplottext);
564
565         hfignt = figure(vi);
566         set(hfignt,'Position',[0, 0, 1500, 1000],'visible','off');
567         scatter(Xv(:,1)+Yv(:,1),Xv(:,2)+Yv(:,2),10,dmg(:,1),'filled');hold on;
568         colormap('jet')
569         caxis([0 0.5])
570         colorbar
571         axis([-0.11 0.11 -0.07 0.07 ])
572         daspect([1 1 1])
573         text(-0.1, -0.065,['timestep =',tts]);
574         text(-0.05, -0.065,['ctime =',cts,'s']);
575         text(0.0, -0.065,['Elongation =',eint,'%']);
576         text(0.5, -0.065,['CTOD =',ctodtext,'mm']);
577         set(gca,'fontsize',10)
578         VideoOutFailure(vi) = getframe(gcf);
579         close(hfignt)
580
```

```
581         hfignt2 = figure(vi);
582         set(hfignt2, 'Position',[0, 0, 1500, 1000],'visible','off');
583         scatter(Xv(:,1)+Yv(:,1),Xv(:,2)+Yv(:,2),10,Yv(:,1),'filled');hold on;
584         colormap('jet')
585         caxis([-0.005 0.005])
586         colorbar
587         axis([-0.11 0.11 -0.07 0.07 ])
588         daspect([1 1 1])
589         text(-0.1, -0.065,['timestep =',tts]);
590         text(-0.05, -0.065,['ctime =',cts,'s']);
591         text(0.0, -0.065,['Elongation =',eint,'%']);
592         text(0.5, -0.065,['CTOD =',ctodtext,'mm']);
593         set(gca,'fontsize',10)
594         VideoOutUX(vi) = getframe(gcf);
595         close(hfignt2)
596         vi = vi + 1;
597     end
598 end
599 %%
600 figure()
601 scatter(Xv(:,1)+Yv(:,1),Xv(:,2)+Yv(:,2),10,Yv(:,1),'filled')
602 colormap('jet')
603 caxis([-0.01 0.01])
604 colorbar
605
606 %% Write video files
607 Video = VideoWriter('FMw120A40Bft2_nx150_failure.avi');
608 Video.FrameRate = 25;
609 %Video.Height    = 1000;
610 %Video.Width     = 700;
611 Video.Quality   = 100;
612 open(Video);
613 writeVideo(Video, VideoOutFailure);
614 close(Video);
615 %%
616 Video = VideoWriter('FMw120A40Bft2_nx150_UX.avi');
617 Video.FrameRate = 25;
618 %Video.Height    = 1000;
619 %Video.Width     = 700;
620 Video.Quality   = 100;
621 open(Video);
622 writeVideo(Video, VideoOutUX);
623 close(Video);
```